UNIVERSITY OF CALIFORNIA

SANTA CRUZ

THE INFLUENCE OF SMALL STRESSES ON THE DYNAMICS OF GLACIERS AND SUBDUCTION ZONES

A dissertation submitted in partial satisfaction
of the requirements for the degree of

DOCTOR OF PHILOSOPHY

in

EARTH SCIENCES

by

Jacob I. Walter

September 2012

The Dissertation of Jacob I. Walter
is approved:

Professor Slawek Tulaczyk, Chair

Professor Emily E. Brodsky

Professor Susan Y. Schwartz

Professor Thorne Lay

Tyrus Miller
Vice Provost and Dean of Graduate Studies

Abstract

The influence of small stresses on the dynamics of glaciers and subduction zones

by

Jacob I. Walter

The fast flow of glaciers and rupture of earthquakes on subduction zones both occur at interfaces notoriously difficult to observe. When slip events occur on such interfaces, elastic energy is radiated in the form of seismic waves. Here, we analyze these and other signals, such as continuous GPS, for two glacier systems and a subduction zone. We find that the slip events at an Antarctic ice stream, a Greenland outlet glacier, and a subduction zone in Costa Rica are all modulated by the ocean tide, however, the manifestations of the modulations vary considerably.

In Antarctica, we directly measure the bidaily rupture process of the Whillans Ice Plain using broadband seismometers. The average rupture speed of these events varies by a factor of 2, which is dependent upon the recurrence interval. Based on variations of rupture near the source region, we observe that rupture speed depends on loading conditions.

In Greenland, the breakup of the sea ice and iceberg mixture that forms during the winter causes changes in the flow velocity of Store Glacier, West Greenland. We measure velocity using continuous GPS 16 km away from the terminus and time-lapse photography near the terminus. We observe a step-change in velocity near the terminus in response to the ice melange breakup, corresponding to a 30-60 kPa loss of

buttressing stress. Further, we observe semi-diurnal periodicity in GPS speed perturbations 16 km from the terminus, likely due to ocean tides.

At the subduction zone, we identify and locate tremor events, distinct from earthquakes in their low amplitude, which occur as shear failure on the plate interface. We locate the events on portions of the plate believed to be undergoing stable sliding, adjacent to locked portions of the plate. Furthermore, we provide multiple forms of geodetic and pressure evidence of an offshore event that occurred in 2008.

Observations of various behaviors that include relatively small stresses may provide insight into the unique dynamics of glaciers and subduction zones. Small stresses that drive failure suggests either a weak basal interface or a system near its critical stress state.

Acknowledgments

Over the course of my graduate career, I have been incredibly fortunate to have the guidance of three wonderful advisors in Slawek, Emily, and Susan. I have appreciated each of their unique "styles" for advising in my development as a scientist. I especially want to thank Slawek for giving me an extraordinary amount of responsibility and respect early on, which propelled me in the right direction. Emily was a constant source of technical knowledge and more importantly, motivation that what I was doing was worthwhile science. Susan always provided a welcome sanity check on my writing and I have finally come to appreciate her constant reminder to "just look at the seismograms!" I would like to thank Thorne for serving on my committee and being such a vast resource for all things seismological. Dan helped with many technical challenges with the seismometers and other field equipment, without him, a lot of these measurements would not be possible.

I am especially grateful for having such a loving and supportive family in my parents, Kymn and Bobbie, my brother, Ryan, and sister, Julie. I have appreciated the support of friends and fellow graduate students, who either helped me directly with frustration by helping me academically or providing a distraction from the problem at hand. They are, in no particular order, Tristan, Einar, Andrew, Meegs, Karin, Stephanie, Rachael, Don, Dan (again), Laura, Lauren, Lia, Krista, Lucas, Ken, Saffia, and Sophie.

Table of Contents

1. INTRODUCTION

The fast flow of glaciers and rupture of earthquakes on subduction zones occur at the interface between two elastic bodies. Directly measuring physical properties of those interfaces is notoriously difficult and expensive, if not impossible. When slip events occur on tectonic faults, elastic energy is radiated in the form of seismic waves and an earthquake occurs. Analogously, a glacier can either slip fast enough or calve with sufficient energy to generate seismic waves observable thousands of kilometers away. Yet, in both cases, slip events can also occur over a much longer duration and be nearly undetectable.

Recent advancements and widespread availability of geophysical monitoring has allowed us to observe many small, previously undetected movements of glaciers and subduction zones continuously. In this way, we are able to assess the transience and repeatability of such movements. Determining the spatial and temporal variability of motion improves our understanding of glacier dynamics and earthquake cycles, which may have important societal implications. By observing these phenomena over long periods of time, we can assess the variability of behavior and determine if external forcing enhances the slip. The susceptibility of slip events to external forces may allow us to infer properties of the glacier basal or fault interface.

One manifestation of frictional sliding occurs at the Whillans Ice Plain (WIP), West Antarctica, which slips 0.5 m in ~30 min, typically twice daily (Bindschadler et al., 2003). During two field seasons, in the austral summers of 2008 and 2010, we

have deployed broadband seismometers and continuous GPS receivers to monitor the rupture process that occurs during slip events. We observe the ice motion that occurs during the slip event and the propagation of the rupture front across the WIP during the event (Walter et al., 2011a). In addition to observing behavior in the near-field, when the rupture front reaches the edge of the slipping interface, it generates a seismic wave observable up to 1000 km away (Wiens et al., 2008). Using data acquired during the 2008 field season, we find that as the rupture front propagates towards the stations, the amplitude of the initial wave arrival correlates linearly with eventual slip that occurs over the ~30 min event (Walter et al., 2011a). Also the rupture speed, estimated using a combination of arrival times at near- and far-field stations, varies by a factor of 2 for different events and linearly correlates with inter-event duration or recurrence interval.

On closer inspection, using an augmented regular array of broadband seismometers in 2010, the WIP exhibits near-source rupture speed variability for the two modes of tide: high tide events rupture slower near the source region, and low tide events rupture faster near the source region. Furthermore, there two separate source region locations for the two modes: high tide events locate further from the grounding line than low tide events. We hypothesize that tidal flexure of the ice at the grounding line causes the shift in nucleation zone with tide. When an elastic beam flexes, it also imparts downward forces, depending on the direction (high or low tide) of flexure. The nucleation zone for each mode of the tide may correspond to points on the ice stream where the downward force is applied. However, once the

rupture is a significant distance away from the nucleation, it behaves more consistently with previous observations, where the average rupture speed is linearly correlated with inter-event duration. Our measurements provide insight into the rupture process and may indicate that certain rupture properties are governed by the loading conditions.

At the opposite hemisphere, we observed the fast motion of a west Greenland outlet glacier, Store Glacier. We monitored flow speed at two positions on the glacier, using time-lapse photogrammetry and continuous GPS. In addition, we monitored the calving rate using an array of broadband seismometers surrounding the terminus of the glacier. At the front of Store Glacier, a seasonal bonded mix of sea ice and calf icebergs forms during winter and breaks up in the spring. This feature is called an ice melange. During the spring breakup, we observe changes in observed velocities at two measurement points shortly following the melange breakup, near the terminus and at a GPS station 16 km from the terminus. At the terminus, we observe a step-change in the velocity of 1.5 m/d (average velocity is 11 m/d). At the GPS station we record diurnal and semi-diurnal speed perturbations. The semi-diurnal speed perturbations are evidence of tidal influence of ice flow. Furthermore, using the step-change in velocity near the terminus region, we estimate a melange buttressing stress of 30-60 kPa. Such measurements are an example of utilizing external forcing to estimate various material conditions of the dynamic system.

Ever since Obara (2002) showed that geodetic slow slip events are sometimes accompanied by non-volcanic tremor, an emergent and low amplitude seismic signal,

efforts have been concentrated on identifying the phenomena at other subduction zones. Utilizing a broadband network of seismometers, we have identified tectonic tremor and slow slip at the Nicoya Peninsula, in northern Costa Rica (Walter et al., 2011b). The tremor sources locate in regions believed to be aseismic regions, with respect to the pattern of inter-seismic locking. Therefore, the absence of tremor may delineate zones that are actively accumulating frictional stress that may rupture in large earthquakes. By closely analyzing the frequency of tremor occurrence, we find that tremor activity may be periodic around the ~180 day period, which corresponds to periodicity of the equinox tide. During an event in August 2008, the tremor activity is consistent with the calculated change in Coulomb stress induced by the ocean tides. Further evidence from a pressure observatory in a seafloor borehole and GPS evidence for slow slip, suggests that a slow slip event occurred at a shallow depth on the plate interface. It remains an open question and ongoing debate whether such slow slip increases or decreases the earthquake hazard at subduction zones.

At all three geographic settings, we observe the movement of glaciers and subduction zones to be modulated in various ways by the tide. The tide imparts very small stresses and small stresses driving failure suggest either a weak basal interface or a system near its critical stress state. A better understanding of the physics of fast glacier flow has the potential to improve ice sheet models that forecast future sea-level rise. Similarly, a better understanding of the dynamics of subduction zones and the earthquake cycle has the potential to save lives.

2. TRANSIENT SLIP EVENTS FROM NEAR-FIELD SEISMIC AND GEODETIC DATA ON A GLACIER FAULT, WHILLANS ICE PLAIN, WEST ANTARCTICA

The following Chapter, essentially unchanged, appeared previously in the Journal of Geophysical Research:

Walter, J. I., E. E. Brodsky, S. Tulaczyk, S. Y. Schwartz, and R. Pettersson (2011), Transient slip events from near-field seismic and geodetic data on a glacier fault, Whillans Ice Plain, West Antarctica, J. Geophys. Res., 116, F01021, doi:10.1029/2010JF001754.

2. TRANSIENT SLIP EVENTS FROM NEAR-FIELD SEISMIC AND GEODETIC DATA ON A GLACIER FAULT, WHILLANS ICE PLAIN, WEST ANTARCTICA

Abstract

Bi-daily, tidally modulated stick-slip speed-ups of the Whillans Ice Plain (WIP) provide insight into glacier dynamics and failure at a naturally repeating fault asperity. We installed a network of continuously operating GPS receivers in 2007 and deployed on-ice broadband seismometers during the austral summer of 2008 on Whillans Ice Stream (WIS), West Antarctica and recorded 26 glacier speed-up events. Previous work during the 2004 field season suggested that these speed-ups initiate as failure of an asperity on or near "Ice Raft A" that triggers rupture across the entire WIP. Our results for 2008 locate the slip initiation farther to the south of this feature, closer to the grounding line and the southernmost extent of the Ross Ice Shelf. The initiation may be controlled by a discontinuity in basal boundary conditions at the suture between two ice streams. A strong correlation between the amplitude of seismic waves generated at the rupture front and the total slip achieved over the duration of the slip event (~ 30 min) suggests slip-predictable behavior, i.e., the ability to forecast the eventual slip based on the first minute of seismic radiation. Successive slip events propagate with different rupture speeds (100-300 m/s) that strongly correlate ($R^2 = 0.73$) with the inter-event duration. In addition, the amount of slip achieved during each event appears to be correlated with the rupture speed. We use these observations to constrain basal shear stress to be 4 kPa by calculating conditions for basal freezing. Our observations yield information regarding

mechanics and dynamics of ice stream beds at the scale of 10s to 100s of km. Subglacial processes are notoriously difficult to constrain on these large scales, which are relevant to the understanding of regional and continental ice motion.

2.1. Introduction

The recently discovered episodic slip events on the Whillans Ice Stream in Antarctica indicate that twice a day the glacier locally speeds up to a slip rate of 10s of cm per hour for 20-30 minute periods [Bindschadler et al., 2003a]. Wiens et al. [2008] have shown that the slip velocity of the ice becomes fast enough during these slip events to generate seismic waves that are observable at far-field stations near the South Pole (QSPA) and the Dry Valleys, Antarctica (VNDA).

Twice daily stick-slips are intrinsically interesting as a direct indication of the mode of glacier motion and episodic slip provides a window into the physical conditions at the base of the glacier. Periodic or episodic movement in a system driven by far-field, steady motion is a hallmark of stick-slip as most commonly evidenced by earthquakes on tectonic faults [e.g. Brace and Byerlee, 1966]. Winberry et al. [2009] suggest that this basic stick-slip model is applicable to the ice sheet, where the base is locked by friction between events and loaded by elastic strain accumulation in the glacier. Eventually the local frictional resistance is overcome and the glacier jerks forward, releasing the elastic stress, and beginning the cycle again. In this scenario, the timing, size, and location of the slip events provide information

about the basal friction, and its control on overall glacial movement.

In this paper, we use newly acquired field data and techniques borrowed from the tectonic earthquake community to closely study these episodic slip events, to constrain the conditions at the base of the glacier. After describing the data collection, we highlight five key observations about glacial slip events: (1) the presence and shape of an initiation phase in addition to previously reported stopping phases, (2) the variability of the rupture speed and its association with final slip, (3) the location of the start of slip events, (4) the correlation between the initiation phase amplitude and the final slip, and (5) the presence of inter-event stable sliding. We then proceed to combine and interpret these observations to address five different physical points: (1) the relationship between glacial slip and tectonic earthquakes, (2) the physical controls on the start of slip, (3) the slip-predictability, (4) the stress drop during events, and (5) the role of basal freezing in healing.

2.2. Data Collection

2.2.1 Seismic and Geodetic Data

During December of 2007, we established a network of continuously-sampling GPS stations on WIS/WIP at strategic locations to capture the hydrology and dynamics of an active subglacial lake network [Fricker et al., 2007]. We used the online precise point positioning (PPP) service provided by Natural Resources Canada (http://www.geod.nrcan.gc.ca/online_data_e.php) to obtain a position for each sample. The GPS receivers record a position every 15 seconds and have operated

continuously since installation, with plans to operate through 2014.

Following the establishment of the GPS network, in the November/December 2008 field season, we operated broadband seismometers on WIS. The broadband seismometers operated at 100 Hz and all but one (A702) were co-located with continuous GPS stations (Figure 1). In addition, we used far-field data from the Global Seismic Network (GSN), including stations QSPA and VNDA, which are about 650 and 990 km away, respectively, from WIP. Their location relative to our field study area appears on Figure 1.

2.2.2 Ice-penetrating Radar

Context for the slip events is provided by data on the subglacial structure from ice-penetrating radar. In a previous field season (Nov. 2007), we collected about 180 km of radar profiles in a transect crossing the suture zone, where the WIS and Mercer Ice Stream (MIS) converge to form the Whillans Ice Plain (WIP). The transect crosses through GPS stations M6, M8, and M9, and continues along this general line southwest. The radar data were collected using a ground-based low frequency impulse radar with 10 MHz resistively loaded dipole antennas, giving a pulse wavelength of ~20 m in ice. The transmitter consisted of a solid-state high voltage pulse source with a repetition frequency of 1 kHz. The receiver was a 12-bit low-noise digitizer. Individual traces were stacked 200 times and the average trace spacing was 18m. Trace locations were determined using geodetic two-frequency GPS measurements. The collected data were corrected for normal moveout,

dewowed, and low-pass filtered before being displayed. Conversion of travel times to depth was done assuming a wave speed in ice of 168 m/s.

Relative reflectivity of the bed was estimated using the method of Jacobel et al. [2009] who use recorded returned power of the bed as a proxy for bed conditions, where stronger bed returns are typically interpreted as wetter bed. The method requires that the recorded bed power is corrected for geometrical spreading, as well as, attenuation in the ice column. The geometrical spreading can be easily corrected for, but the attenuation within the ice is more difficult to estimate. A common approach in radioglaciology is to use spatial variations in bed power normalized to a constant depth as a proxy for englacial attenuation [Gades et al., 2000, Winebrenner et al., 2003, Jacobel et al., 2009]. In this study we use the variations in depth-averaged returned bed power from all our profiles to estimate the attenuation rate. This gives an attenuation rate of 23.7 dB/km, which is similar to earlier reported attenuation rates for ice streams in West Antarctica [Jacobel et al., 2009 and references therein]. After correcting for geometric spreading and englacial attenuation, the returned bed power is assumed to dependent mainly on the dielectric contrast across the ice-bed interface and is taken to be a proxy for the water abundance at the bed.

2.3. Observations

2.3.1 Slip Event Description

2.3.1.1 Near-field records of slip events

We recorded a series of slip events at the on-ice, co-located continuous GPS receivers, and broadband seismometers. Slip events typically last 25-30 min and have total displacements of 0.2-0.5 m (Figure 2). At each locale, the onset of slip is rapid, as revealed by the steep slope of the GPS records. The co-located seismometers record a small amplitude, medium period (<100 s) arrival coincident with the GPS slip onset (red box in middle panel of Figure 2). We will refer to this portion of the wave as the initiation phase throughout the remainder of the paper. After the initiation phase, the seismograms record the same integrated displacement as the GPS records, as the instruments move along with the slipping ice (lower panel of Figure 2).

The seismic initiation phase arrives synchronous with the start of GPS slip for every slip event and is recorded on each station as the rupture front sweeps across the network (Figure 3). In the record section shown on Figure 3, the seismic data have been bandpassed (0.012-0.04 Hz) in order to highlight the energy contained within the initiation phase.

In addition to recording the initiation of the slip events as the rupture front passes beneath each station, some of the on-ice stations also record evidence of the rupture front stopping at a discrete location ~100 km from its origin. Figure 3 depicts this stopping phase, which we call Phase B, as observed in the near-field records. Far-field seismic records show at least two stopping phases, and we describe these in more detail in the following section.

2.3.1.2 Far-field records of slip events

We obtained broadband seismic data from far-field stations VNDA (~990 km

from WIP) and QSPA (~650 km from WIP) for the time period overlapping operation of our on-ice stations. Examples of waveforms from these stations appear on the lower half of Figure 3. Figure 3 contains a case of a triple-phase long period waveform from VNDA first described by Wiens et al. [2008]. Throughout this paper, we refer to the three phases on the far-field record as Phase A, Phase B, and Phase C (Figure 3). Of the 26 slip events observed during our 2008 field season, only 5 had all three phases (A, B, and C) visible on VNDA records, with the majority lacking Phase A (Record sections for all of the slip events are included as Supplementary Material). Phase B is visible on VNDA records for 22 of 26 events and Phase C is visible on VNDA records for 17 of 26 events.

Wiens et al. [2008] suggested that the triple-phased long-period waveforms visible at stations VNDA and QSPA are Rayleigh waves representing a starting and two stopping phases of the WIP slip (See schematic on Figure 4). They located the initiation of the slips (Phase A) at "Ice Raft A," whose outline appears on Figure 1, using a grid-search of the GPS slip initiation. Phase B and C arrivals were interpreted to be stopping phases and located both using a surface wave grid-search technique. According to their methods, Phase B locates ~50 km south of "Ice Raft A", near the region we suggest the slips start (See Figure 1 and below for location methods), and Phase C locates ~120 km north of "Ice Raft A".

Phase B arrives at VNDA ~11-24 minutes after the first detected motion on the Ice Plain. The travel-time for a Rayleigh wave originating at the Ice Plain would be only ~5.5 minutes. In the next section, we show that this can be explained by a

rupture speed variation of up to a factor of two between subsequent events. When Phase B is generated, the on-ice stations (A702 and Cookie) consistently observe Phase B ~5.5 minutes prior to VNDA. The constant relative timing of the near-field and far-field arrival supports their identification as the same seismic phase.

The on-ice stations never record Phase A. If this phase corresponds to the initiation of rupture at the origin of the slip event as proposed by Wiens et al. [2008], then it originates ~50 km from any of our stations (A more precise location will be provided below). Absence of Phase A arrivals in the near-field records suggests that it does not propagate in ice at close distances. Phase A is distinct from the initiation phase that accompanies the beginning of slip at each station. Phase A records the global initiation of slip on the ice stream; the initiation phase records the local slip start as the rupture front arrives at a station.

2.3.2 Rupture Speed Variations

The difference in time between the arrival of stopping Phase B at station VNDA and the start of a slip event detected at on-ice stations varies between events. The difference covers a range of ~11-24 min, which is much greater than the ~5.5 min travel-time for a Rayleigh wave originating at WIS to travel ~1000 km to VNDA. The range in the arrival time of Phase B suggests that the time for the slip to rupture across the WIP varies from ~5-18 min. Such a range in rupture time can be generated by subsequent changes in either rupture speed or rupture length. Previous work [Wiens et al., 2008] showed that the rupture speed varies from 0.1-0.2 km/s for

each event. Therefore, we first investigate the possibility that the range Phase B arrivals is due entirely to variation in rupture velocity. Later, we will pursue the alternative hypothesis by varying the rupture length.

The total travel-time observed for Phase B is the sum of the on-ice rupture time and the propagation time from the arrest location to the station (Figure 4). Assuming that the wave travels from the Ice Plain to the station as a Rayleigh wave, the propagation time can be calculated. Therefore, if we assume a constant rupture length, we can calculate a rupture velocity from the observed travel-times. The rupture velocity in this model is

$$V_{rupture} = \frac{L_{rupture}}{t_{VNDA} - \frac{d_{far-field}}{V_{Rayleigh}}} \qquad (1)$$

where $V_{Rayleigh}$ is the Rayleigh wave speed (3 km/s), $d_{far\text{-}field}$ is the distance to the station , $L_{rupture}$ is the length of rupture, and t_{VNDA} is the difference in time between the origin time and arrival of Phase B at station VNDA (See Figure 4). We use values of 990 km and 100 km for $d_{far\text{-}field}$ and $L_{rupture,}$ respectively. Both of these values are approximate. Based on the configuration in Figure 1, the far-field distance can vary by about 100 km. This uncertainty results in ~30 s uncertainty in travel time, which is at maximum <5% of the observed arrival time variability. The inferred rupture velocities are more strongly dependent on $L_{rupture}$ and this sensitivity will be explored below. We use VNDA arrivals, rather than QSPA, for rupture speed analysis, as they are detected more frequently.

Typical values for rupture speed based on Equation 1 vary between 0.1-0.3 km/s (See Supplementary Table 2). This range is comparable to the range of previous work on WIP slip events and significantly below the usual rupture speed for earthquakes (~3 km/s) [e.g. Kanamori and Brodsky, 2004].

We now consider the alternative hypothesis that rupture length variability controls the variability in Phase B arrival times. Because our GPS network is not able to observe the entirety of the rupture area, we do not have direct constraints on $L_{rupture}$. We therefore calculate values of $L_{rupture}$ from Equation 1 with fixed rupture speeds and the observed arrival times and evaluate the plausibility of the resulting values. The minimum value of $V_{rupture}$ = 0.1 km/s corresponds to inferred rupture lengths of 38-78 and the maximum of $V_{rupture}$ = 0.3 km/s results in 95-234 km. The length of 234 km exceeds any dimension of the WIP and 38-78 km is smaller than the distance between many of the stations and the furthest slip-start location. The rupture speed fluctuations therefore provide the more plausible cause of the large range (~11-24 min) of arrival time variations at the far-field station.

A closer look at the Phase B and C separation also provides important constraints upon the varying nature of the rupture speeds. In order to assess phase and/or amplitude variations between subsequent events, we plot various waveforms for VNDA with respect to each rupture velocity as inferred from Equation 1 on Figure 5a. The figure shows that the lag between Phase B and Phase C arrivals increases with decreasing rupture velocity. This suggests that Phase B and C, as stopping phases, have fixed locations, a feature also identified by Wiens et al. [2008].

Multiplying the time difference between the Phase B and Phase C arrivals at the maximum and minimum rupture speeds, yields a consistent value of ~60 km. This value is a minimum rupture distance perpendicular to the wavefront from the initiation point, for the two stopping locations.

A similar pattern is seen for data from 2004. Wiens et al. [2008] published a catalog of slip event origin times for their field season in the austral summer of 2004. We obtained VNDA data for 2004 and with use of the Wiens et al. [2008] catalog, we repeated the steps described above and obtained rupture velocity estimates consistent with our observations in 2008 (Figure 5b). Although the basic pattern of arrivals is the same, there is one clear difference. The 2004 data contain more Phase A arrivals than are present for slip events in 2008. In both 2004 and 2008, the slip events with lower rupture velocities seem to preferentially generate Phase A arrivals.

Another distinguishing feature of these slip events is that the total slip achieved over the slip event scales with the rupture velocity. Figure 6 indicates a strong correlation (R^2 value of 0.79 and p-value of 0.0005) between the GPS slip and inferred rupture velocity. Previous work hinted at the possibility of such a correlation, as Wiens et al. [2008] qualitatively observed a correlation between Ross Sea tidal amplitude and rupture velocity; and Winberry et al. [2009] modeled the stress balance on the WIP from ocean tides showing that high tide increases shear stress, which corresponds to increased slip. Therefore, the correlation between rupture velocity and slip was implicit in the earlier work, but was not specifically addressed until now.

2.3.3 Location of Slip Start

We locate the start of the slip events by inverting the initiation phase arrival times for the on-ice seismometers from the 2008 field season (Figure 1). We implement a 2-D (x, y, t) linear least squares inversion of the arrival times by assuming a unique rupture speed for each event (See Appendix A for a detailed description). The rupture speed varies between events and an average quantity is inferred from Equation 1 for each individual event. We also calculate error ellipses, with two standard deviations representing the 95% confidence interval (Figure 1). The zone encompassed by our locations and error ellipses is south of our seismic network and adjacent to the grounding line.

Seismic arrival times are much more reliable for timing of the rupture front propagation than determining arrival of the rupture using GPS, as it is difficult to accurately pick an arrival time on coarsely sampled GPS data (15s sample spacing in this study). At co-located stations, automatic and handpicked GPS initiation times can range from simultaneous to 60 seconds after the seismic arrival. Therefore, picking seismic arrivals is better suited for inverting for the origin of the slip-start.

The zone does not intersect "Ice Raft A," as suggested in Wiens et al. [2008]. One possible issue is that Wiens et al. [2008] state that the rupture speed is ~1000 m/s within 20-30 km of the nucleation zone and decreases to ~100 m/s at the edges of WIP. Given these approximate guidelines, we performed a second inversion using a velocity of 1000 m/s at the source, that linearly decreases over 100 km to 0 m/s. The details of this second inversion are provided in Supplementary Material. With this

second inversion, the general location of the slip-start locations (See Supplementary Figure 1) does not change significantly and all locations fall within the region shown on Figure 1, inclusive of the error ellipses.

A few events are particularly diagnostic of the slip start location. For Events 19 and 20, the initiation phase arrives at station M6 prior to Whigh, and both arrivals occur within ~10 seconds. (See Supplementary Material; Record Sections for Events 19 and 20). As can be seen from the map in Figure 1, the initiation phase could not possibly arrive at M6 first, if the slip-start was at "Ice Raft A." Furthermore, if the slip events began at "Ice Raft A," the arrivals would be separated by at least 100 seconds with the rupture front passing Whigh first.

2.3.3 Correlation of Initiation Phase Amplitude and Final Slip

In order to understand the rupture process, we compare the amplitude of the initiation phase with the total slip of the event. Total slip displacement over the 20-30 min duration of each slip event is well constrained by the GPS record. The five panels on Figure 7 show the east component amplitude of the initiation phase (east axis is parallel to ice flow direction) versus GPS slip displacement at one particular GPS station, M8. We measure the amplitude of the initiation phase after applying a high-pass filter at 3,000 s (Figure 2). There is a strong linear correlation between amplitude and slip for all stations. The correlations (See Figure 7 for R^2, p-value, and slope of each fit) imply that the events are slip-predictable, with the probability of random occurrence (p-value) being less than 1% at stations M6, Cookie, and

Crevasse.

Seismic waves can be generated during both acceleration and deceleration of slip and their amplitude scales with the moment rate [Lay and Wallace, 1995]. Figure 8 shows the relationship between the stopping Phase B amplitude and slip. The linear relationship in Figure 8 suggests that the slip events appear to stop at a rate that scales with total event slip.

2.3.4 Inter-Event Stable Sliding

The WIP does not remain locked during inter-event periods [Bindschadler et al., 2003b]. We observe inter-event surface displacement that accounts for ~50% of the total daily motion for most stations within our network. Given the low driving stresses of a few kPa acting on WIP, contribution of internal ice deformation to surface velocity is minor [Joughin et al., 2002; Joughin et al., 2004]. Hence, during the inter-event period, the WIP is stably sliding. We calculate the average stable sliding velocity by differencing positions after a slip event and prior to the subsequent event and dividing by the elapsed time (inter-event duration).

We observe that the average stable sliding velocity varies for different inter-event periods with the largest scatter at the smaller periods (Figure 9). For inter-event periods greater than the semi-diurnal period (~ 0.5 day), the inter-event velocity is on average ~0.5 m/day for stations M8, M9, and Cookie. Station Whigh has an inter-event stable sliding velocity ~1/2 that of the above three stations, yet slips nearly twice as much as M8 and M9 during slip events (See Supplementary Table 2).

Therefore the long-term average surface velocity is similar for all the stations despite the differences in partitioning of the total motion between stable sliding and slip events. This behavior suggests that there are multiple frictional asperities at the base of the WIP detectable only through measurement techniques with sub-daily sampling (e.g. continuous GPS).

2.4. Interpretation

2.4.1 Comparison to Tectonic Earthquakes

Glacier stick-slip motion on the WIP is a useful analogue for and may provide insight into tectonic earthquakes. The events we describe in this paper are not quite stick-slip motion, in the sense that the base is not "stuck." Stable inter-event sliding is punctuated by the arrival of a rupture front, which initiates the unstable slip motion. Such a process is analogous to the rupture of large earthquakes into areas less coupled than the frictional asperities believed to be the predominant zones of nucleation [e.g. Moreno et al., 2010]. Bi-daily repeatability and relatively large rupture area on the WIP provide a rich dataset for studying variations in rupture processes and assessing the balance of elastic stresses during rupture. In this paper, we have attempted to measure relevant characteristics of the rupture process, including the amplitude of a wave traveling with the rupture front propagation, slip during the event, and rupture speed of the propagation.

The geometry of the glacier results in unusually close near-field records for a slip event. Most large earthquakes only intersect the surface in a relatively narrow

zone and often this area is underwater at subduction zones. There is seldom an opportunity to place seismometers within 1-2 km of the rupture plane in multiple locations. Therefore, few near-source records exist that accurately record seismic wave amplitudes associated with the propagation of a rupture front. Our observations of the initiation phase amplitude scaling with eventual slip could motivate future investigations into earthquake rupture.

In general, earthquake rupture speeds are usually approximately 0.9 times the shear wave speed and vary relatively little except for a few extreme cases [Kanamori and Brodsky, 2004]. There is no evidence for systematic variation of rupture speed with earthquake size. This consistency for earthquakes is thought to reflect the control of the shear wave speed on the rupture of a dynamic shear crack. Here, we have shown that rupture speeds vary by a factor of two for the WIP events and there is a systematic variation with total slip (Figure 6). In order to accommodate this difference, either the rupture propagation process must be fundamentally different than rapid shear failure observed on tectonic faults, or the shear wave velocity at the base must vary in time.

2.4.2 Physical Controls on Slip Start Location

Our locations show that the slip starts in a region adjacent to the southern section of the WIP grounding line (Figure 1). Due to the overlapping error ellipses, we cannot assess whether the events nucleate in a critical slipping region or if there is a separate origin for each event. The location of the slip-start differs significantly

from a previous study [Wiens et al., 2008] that located the slip starts at "Ice Raft A" and suggested that "Ice Raft A" acts as an asperity.

The spatial difference between locations in our experiment and the TIDES experiment [Wiens et al., 2008] could be due to migration of the dominant asperity over the 4 year period separating the experiments. Temporal variation in asperity location might be related to the century scale slowdown of the WIS [Bougamont et al., 2003], which likely causes a redistribution of the basal stresses. The WIS also contains a dynamic subglacial lake network at its base [Fricker et al., 2007], which could cause stress redistribution at relatively short timescales. An elevation change anomaly designated as Lake 10 [Fricker and Scambos, 2009], which is located at the up-ice edge of the "Ice Raft A," has been filling since observations with IceSAT began (~2004) and is a potential cause for the slip start migration.

Radar imaging of the suture helps to shed light on the basal conditions that may control the slip start location. We assume that the radar image shown in Figure 10 is representative of the suture zone in the slip start region, though it was collected ~50 km from the slip start locations. The data in Figure 10 shows that the bed is more reflective below WIS-sourced ice than MIS-sourced ice, and the height of the overlying ice increases to the southwest, which is where our origin locations cluster. Radar reflectivity of the bed is influenced by the permittivity contrast between the basal ice and the underlying geologic materials. Glaciological interpretations typically attribute a strong bed reflection to subglacial zone with abundant water and/or water that is highly conductive [e.g. Raymond et al., 2006]. Weaker bed

reflection is taken to indicate subglacial materials that contain less water and/or water that is less conductive. A plausible glaciological interpretation of the observed 'dimmer' bed south of the suture zone is that ice there is overriding bedrock, or a relatively more competent till layer than in the area to the north of the suture zone. This suggests that the slip-start region is better frictionally coupled than the bed beneath the main part of the WIP. The enhanced frictional locking may allow sufficient stress to accumulate to nucleate slip events.

Phase A is observed in only 5 of 26 events and its arrival time indicates that it is associated with the slip-start. During our experiment, 4 of 5 Phase A arrivals occur after short inter-event periods, but high inter-event stable sliding velocities (Figure 9). If increased stable sliding velocity translates to better coupling, then we speculate that the presence of Phase A arrivals is dependent upon the degree of ice/till coupling. However, future observations will provide better insight into the physical constraints for Phase A transmission.

2.4.3 Initiation Phase Predicts Final Slip

Figure 7 suggests that the eventual slip of the Ice Plain scales with the amplitude of the initiation phase observed at the rupture front. While amplitude is variable for each station for any given event, the relative size of the initiation phase at a single station correlates with the final GPS slip of the event. This observation implies that the magnitude of the slip event is deterministic based on the conditions during the first 30-100 s of slip.

This ice slip event behavior is in contrast with tectonic earthquakes where the connection between the initiation and the final size of an earthquake is subtle enough to remain controversial [Rydelek and Horiuchi, 2006]. The slip-predictable behavior is consistent with an isolated stick-slip patch with relatively simple driving conditions. An isolated patch is expected to have regular, deterministic motion as opposed to the chaotic behavior of strongly coupled patches [Burridge and Halliday, 1971]. The stick-slip section of the WIP appears to be poised in a transitional basal regime surrounded by a combination of steady sliding and fixed boundaries.

2.4.4 Stress Drops for Glacier Stick-Slip Events

One window into the glacial dynamics is the stress drop during slip events. Stress drops are commonly measured for earthquakes, but because the WIP is a planar slab of ice with a high length-to-thickness aspect ratio, we need to modify the standard seismological theory for this case.

First, we consider the stress equilibrium, $\nabla \cdot \tau = 0$, and assume that the derivatives in the y-direction, perpendicular to ice flow, are negligible,

$$\frac{\partial \tau_{xz}}{\partial z} = \frac{\partial \tau_{xx}}{\partial x} \quad \text{or} \quad \Delta \tau_{xz} = \frac{H}{L} \Delta \tau_{xx}, \tag{2}$$

where H is the thickness of the ice stream (~600 m), L is length (~100 km), x is the slip direction, and z is depth. Next, we use Hooke's Law for the stress-strain relationship,

$$\Delta \tau_{xx} \sim \frac{d}{L} E, \tag{3}$$

where E is Young's modulus (~10 GPa for ice) and d is slip. Combining Equations 2 and 3, the shear stress drop, $\Delta\sigma$, is

$$\Delta\sigma = \Delta\tau_{xz} = C\frac{dH}{L^2}E\,. \qquad (4)$$

where C is a constant of proportionality.

Equation 4 is similar to one proposed and used in modeling efforts [Bindschadler et al., 2003a; Winberry et al., 2009] to approximate driving stresses up-ice in between stick-slip events. It differs from the usual tectonic earthquake stress drop by a factor of H/L. The constant C is typically of order one and depends on geometry [Lay and Wallace, 1995]. Since the shape of the slipping patch is largely unconstrained, we use Equation 4 in its simplest form with C=1 to measure the relative stress drop for each slip event. The resultant stresses range from 50-300 Pa and appear on Figure 11 plotted against rupture speed.

In the calculations for Figure 11, we have assumed a constant rupture length. Due to the geometry of our network, we cannot directly determine rupture length of the events, but previous studies suggest that the entire WIP ruptures during events [Wiens et al., 2008] and our observations in Section 3.2 also favor little variation in length. If this is the case, then the stress drops vary by a factor of two for the glacial events and the variation in total seismic moment is controlled by displacement, not rupture length. This is in contrast to most earthquakes where rupture length varies in proportion to displacement [Kanamori and Anderson, 1975], with only rare

exceptions in places with well-separated stick-slip patches [Harrington and Brodsky, 2009].

We are hesitant to suggest that Figure 11 exhibits a linear correlation between stress drop and rupture speed, given our assumption of a constant rupture length. However, given the co-variation of other observables such as rupture velocity and initiation phase amplitude with the slip, a variation of actual stress with event size could be a plausible relationship for the glacial slip events. However, this bears further investigation with future deployments of more dense instrumental arrays that can capture directly both L and d.

2.4.5 Inter-Event Basal Freezing

The variation in rupture speed with slip suggests a significant variation in material properties at the base of the glacier over time. For tectonic earthquakes, the rupture velocity is limited by the shear wave velocity of the rock and is typically approximately 0.9 times the shear wave speed [Kanamori and Brodsky, 2004]. Blankenship et al. [1987] reported a shear wave speed for in-situ till of approximately 170 m/s at a location 300 km away from our field area. We calculate rupture velocities for the WIP in the range 100-300 m/s for our idealized geometry and Wiens et al. [2008] report rupture velocity variations within a similar range (0.1-0.2 km/s). Even though our observations of rupture speed exceed measurements of till shear wave speed [Blankenship et al., 1987] by nearly a factor of two, crack propagation is governed by the elastic properties over a broader thickness than just the till layer.

Earthquake crack simulations indicate that the appropriate thickness length scale is comparable to the seismic wavelength [Harris and Day, 1997], which would be inclusive of basal ice and underlying marine sediments.

The rupture speed variations suggest variations in the material properties between events, i.e., healing. Some further constraints on such a healing process are: (1) WIP undergoes stick-slip events usually twice daily, which is evidence for a relatively fast healing process and (2) the correlation between rupture speed and inter-event duration on Figure 12 implies time-dependent healing. Finally, (3) the re-rupture of the same large region (~100 x 100 km) requires that the healing process must also be pervasive. Also, if the healing process is driven by hydrological changes within the subglacial till layer (e.g. decrease in pore water pressure and associated sediment strengthening in response to basal freezing), the short repeat interval of the slip events implies that the active process zone in which healing is taking place is relatively thin. The characteristic diffusive thickness of such a zone is just several centimeters, given the low hydraulic diffusivity of West Antarctic tills of ~10^{-8} m^2/s [Tulaczyk et al., 2001] and ~0.5 day repeat interval [Tulaczyk et al., 2000a, p. 475].

To explain the correlation between increased tidal loading and inter-event duration, Winberry et al. [2009] suggested freezing as the likely inter-event healing process. In order to evaluate the likelihood of such a process, we calculate the basal freezing expected during the observed inter-event durations and compare it with the corresponding rupture velocities.

We modify an equation from Paterson [1994] for the dependence of basal

melting/freezing on a basal heat budget to calculate the freezing rate. We change the sign of the equation so that freezing is positive,

$$f_r = \frac{-G - \tau_b u_b + k_i \Theta_b}{L_i \rho_i} \qquad (5)$$

where f_r is freeze rate, G is the geothermal gradient, τ_b and u_b are basal shear stress and velocity, k_i is thermal conductivity of ice, Θ_b is the basal temperature gradient, L_i is latent heat of fusion, and ρ_i is the density of ice. In assigning values for the above constants, we follow previous assumptions for the area [Tulaczyk et al., 2000b; Joughin et al., 2002], and use G = 0.07 W/m^2, k_i = 2.1 W/m°C, Θ_b = 0.046 °C/m, L_i = 333 kJ/kg, and ρ_I = 917 kg/m^3. We use our observed values of inter-event stable sliding at station M8 for values of u_b. For basal shear stress, we input a constant value of 1 kPa, as previous work suggests a value of 1.1 ± 0.9 kPa [Joughin et al., 2002]. We calculate freeze rate, f_r, and multiply by the inter-event duration to obtain an estimate of the frozen thickness, where positive values represent freezing.

Figure 13 shows the linear relationship between the calculated inter-event basal freezing and observed rupture speed. Such a linear relationship could have been anticipated by the correlation between inter-event time and rupture velocity. However, the calculation extends the observation by providing a specific physical process for the correlation, which has implications for other observables within Equation 5.

The freeze rate calculation (Equation 5) is highly sensitive to the product of $\tau_b u_b$. For the basal shear stress, τ_b, we used the nominal value of 1 kPa, based on

Joughin et al. [2002]. In order to assess the sensitivity of our results to this assumption and to place a maximum constraint on basal shear stress, we varied the basal shear stress and calculated the associated freezing, using the range of values for u_b from GPS station M8. Figure 14 shows the associated freezing expected based on Equation 5, when the basal shear stress is allowed to vary between 0-5 kPa. The basal interface transitions into melting near the value of 4 kPa for the range of velocities we observe at our stations.

A further constraint on the basal processes comes from the long-term behavior of WIS. Joughin et al. [2004] shows that the annually averaged velocities for the WIS have been decreasing over the last few decades and suggested basal freezing as the primary mechanism for such a slow-down. Numerical models suggest a similar mechanism for shutdown [Bougamont et al., 2003] of WIS. Recent slider block models of glacier friction suggest that stick-slip behavior, which is now observed on the WIP, is a transitional response to decreasing velocity or increasing static friction, such as would accompany freezing [Sergienko et al., 2009].

Based on our observations of the range of inter-event sliding velocities, and in order to obtain net freezing over long time periods in Equation 5, the basal shear stress is constrained to be below the 4 kPa value. During unstable sliding (slip event), the basal velocity (~0.5 m over ~30 min is ~24 m/day) is at least an order of magnitude faster than during inter-event stable sliding (Figure 9) and promotes melting, therefore the shear stress must be significantly below this upper bound.

In summary, we have shown that at its current surface velocity, the WIP

promotes basal freezing, at sub-daily timescales, up to a limit of 4 kPa, where it transitions to promoting melting. Our results suggest inter-event freezing at a maximum of 7 microns. The freezing can increase the static friction at the base. It can also affect shear wave velocities, and hence rupture velocities, as elastic properties can be very sensitive to grain boundary fluids [Takei, 1998].
Direct measurements do not exist of such small magnitude basal freezing, nor would such a small change be easily directly detected between subsequent slip events. Yet, freezing of this magnitude may be important for glacier dynamics, as laboratory ring-shear experiments of glacier till indicate that strain within till is confined to relatively narrow zones [Iverson et al., 1998].

2.5. Summary and Conclusions

We present new near-field data for glacial slip events collected during the austral summer of 2008. We observe that the slip events contain a distinct initiation phase only observable in the near-field. The amplitude of the initiation phase increases with final slip and rupture velocities, indicating that both of these quantities are determined from the start of rupture. The ruptures begin in a region near the suture zone between Whillans and Mercer Ice Streams. Radar data indicates a distinction in bed properties that is consistent with the slip events nucleating in a relatively drier, higher friction region. Between events, the rupture region continues to stably slide at a lower rate indicating incomplete locking with the base.

The variation of slip between events and slip-predictability are consistent with

standard stick-slip models of earthquakes on isolated asperities. However, the variation in rupture velocity with size is a distinct feature of glacial events that may be explained by a variation in shear wave velocities controlled by extremely small-scale inter-event freezing. In order for this freezing to occur, the basal shear stress cannot exceed 4 kPa.

2.6. Acknowledgements

Thorough and thoughtful reviews by the Associate Editor, Martin Truffer, Fabian Walter, and Paul Winberry considerably improved this paper. This work was funded primarily by NSF Antarctic Sciences Division Grant number 0636970. A NASA Earth and Space Science Fellowship provided support for J.I.W. We would like to thank John Woodward and Saffia Hossainzadeh for assistance in the field. We thank Dan Sampson for providing technical assistance prior to fieldwork and Doug Wiens for loaning some of the passive seismic sensors. Raytheon Polar Services provided field support and logistics. The GPS stations were provided by the UNAVCO Facility with support from the National Science Foundation (NSF) and National Aeronautics and Space Administration (NASA) under NSF Cooperative Agreement No. EAR-0735156. Some of the instruments used in the field program were provided by the PASSCAL facility of the Incorporated Research Institutions for Seismology (IRIS) through the PASSCAL Instrument Center at New Mexico Tech. Data collected during this experiment will be available through the IRIS Data Management Center. The facilities of the IRIS Consortium are supported by the National Science

Foundation under Cooperative Agreement EAR-0552316 and by the Department of Energy National Nuclear Security Administration.

2.7. References

Bindschadler, R. A., M. A. King, R. B. Alley, S. Anandakrishnan, and L. Padman (2003a), Tidally controlled stick-slip discharge of a West Antarctic ice stream, Science, 301: 10871089.

Bindschadler, R. A., P. L. Vornberger, M. A. King, and L. Padman (2003b), Tidally driven stick-slip motion in the mouth of Whillans Ice Stream, Annals of Glaciology, 36, 263-272.

Blankenship, D. D., S. Anandakrishnan, S., J. L. Kempf, and C. R. Bentley (1987), Microearthquakes under and alongside Ice Stream B, Antarctica, Annals of Glaciology, 9, 30-34.

Bougamont, M., S. Tulaczyk, and I. Joughin (2003), Numerical investigations of the slow-down of Whillans Ice Stream, West Antarctica: is it shutting down like Ice Stream C?, Annals of Glaciology, 37, 239-246.

Brace, W. F. and J. D. Byerlee (1966), Stick-slip as a mechanism for earthquakes, Science, 153(3739).

Burridge, R. and G. S. Halliday (1971), Dynamic shear cracks with friction as models for shallow focus earthquakes, Geophys. Jour. of the Royal Astr. Society, 25, 1-3.

Fricker, H. A., T. Scambos, R. Bindschadler (2007), An active subglacial water system in West Antarctica mapped from space, Science, 315(5818): 1544-1548.

Fricker, H. A. and T. Scambos (2009), Connected subglacial lake activity on lower Mercer and Whillans Ice Streams, West Antarctica: 2003-2008, Journal of Glaciology, 55(190): 303-315.

Gades, A.M., C.F. Raymond, H. Conway and R.W. Jacobel (2000), Bed properties of Siple Dome and adjacent ice streams, West Antarctica, inferred from radio-echo sounding measurements, Journal of Glaciology, 46(152), 88–94.

Harrington, R.M. and E. E. Brodsky (2009), Source Duration Scales with Magnitude Differently for Earthquakes on the San Andreas Fault and on Secondary Faults in Parkfield, CA , Bull. Seism. Soc. Am., 99, 23-23-2334.

Harris, R. A. and S. M. Day (1997), Effects of a low-velocity zone on a dynamic rupture, Bull. of the Seism. Soc. of Amer., 87(5): 1267-1280.

Horgan, H. J., and S. Anandakrishnan (2006), Static grounding lines and dynamic ice streams: Evidence from the Siple Coast, West Antarctica, Geophys. Res. Lett., 33, L18502.

Iverson, N. R., T. S. Hooyer, and R. W. Baker (1998), Ring-shear studies of till deformation: Coulomb plastic behavior and distributed strain in glacier beds, Journal of Glaciology, 44(148): 634-642.

Jacobel, R., Welch, B., Osterhouse, D. J., Pettersson, R., MacGregor, J. A., 2009. Spatial variation of radar-derived basal conditions on Kamb Ice Stream, Annals of Glaciology, 51, 10–16.

Joughin, I., S. Tulaczyk, R. Bindschadler, and S. F. Price (2002), Changes in west Antarctic ice stream velocities: Observation and analysis, J. Geophys. Res., 107(B11), 2289, doi:10.1029/2001JB001029.

Joughin, I., S. Tulaczyk, D. R. MacAyeal, and H. Engelhardt (2004), Melting and freezing beneath the Ross Ice Streams, Antarctica, Journal of Glaciology, 50 (168).

Kanamori, H. and D. L. Anderson (1975), Theoretical basis of some empirical relations in seismology, Bulletin of the Seismological Society of America, 65(5): 1073-1095.

Kanamori, H. and E. E. Brodsky (2004), The physics of earthquakes, Rep. Prog. Phys., 67, 1429-1496.

Lay, T. and T. C. Wallace (1995), Modern Global Seismology, Academic Press, 521 pp.

Moreno, M., M. Rosenau, and O. Onchen (2010), 2010 Maule earthquake slip correlates with pre-seismic locking of Andean subduction zone, Nature, 467, doi:10.1038/nature09349.

Paterson, W.S.B. (1994), The physics of glaciers, 3rd edition, Pergammon Press, 480 pp.

Raymond, C. F., G. A. Catania, N. Nereson, and C. J. Van der Veen (2006), Bed radar reflectivity across the north margin of Whillans Ice Stream, West Antarctica, and implications for margin processes, Journal of Glaciology, 52(176): 3-10.

Rydelek, P. and S. Horiuchi (2009), Earth Science: Is earthquake rupture deterministic? Nature **442**, E5-E6.

Sergienko, O. V., D. R. MacAyeal, and R. A. Bindschadler (2009), Stick-slip behavior of ice streams: modeling investigations, Annals of Glaciology, 50(52): 87-94.

Shabtaie, S., I. M. Whillans, and C. R. Bentley (1987), The morphology of Ice Streams A, B, and C, West Antarctica, and their environs, Journal of Geophysical Research, 92(B9): 8865-8883.

Stein, S. and M. Wysession (2003), An Introduction to Seismology: Earthquakes and Earth Structure, Blackwell Publishing.

Takei, Y. (1998), Constitutive mechanical relations of solid-liquid composites in terms of grain-boundary contiguity, J. Geophys. Res., 103(B8), 18183-18203.

Tulaczyk, S., Kamb, B. & Engelhardt , H. 2000a: Basal mechanics of Ice Stream B, West Antarctica. I. Till mechanics, J. Geophys. Res., 105, 463–481.

Tulaczyk, S., Kamb, B. & Engelhardt , H. (2000b), Basal mechanics of Ice Stream B, West Antarctica. II. Undrained-plastic-bed model, J. Geophys. Res., 105, 483–494.

Tulaczyk, S., Kamb, B. & Engelhardt , H. F., (2001), Estimates of effective stress beneath a modern West Antarctic ice stream from till preconsolidation and void ratio. Boreas, Vol. 30, pp. 101–114.

Wiens, D. A., S. Anandakrishnan, J. P. Winberry, and M. A. King (2008), Simultaneous teleseismic and geodetic observations of the stick-slip motion of an Antarctic ice stream, Nature, 453: 770774.

Winberry, J. P., S. Anandakrishnan, R. B. Alley, R. A. Bindschadler, and M. A. King (2009), Basal mechanics of ice streams: Insights from the stick-slip motion of Whillans Ice Stream, West Antarctica, J. Geophys. Res., 114, F01016, doi:10.1029/2008JF001035.

Winebrenner, D.P., B.E. Smith, G.A. Catania, H.B. Conway and C.F. Raymond (2003), Radio-frequency attenuation beneath Siple Dome, West Antarctica, from wide-angle and profiling radar observations, Annals of Glaciology, 37, 226–232.

2.8. Appendix A: Slip-start location inversion

We implement a 2-D (x, y, t) iterative linear least squares inversion to locate the slip event start location (Stein and Wysession, 2003). We use seismic initiation phase arrival times at each of the on-ice stations as the data vector $\underline{d}$. In our case, $\underline{d}$ is an nx1 vector, where n is the number of observing stations for that particular event.

Given an initial guess of origin location and time, we form the model vector $\underline{m}$=(x,y,t). We then calculate the predicted arrival time vector $\underline{d}'$ at each station in the data set using the rupture velocity particular to each event from Supp. Table 2, station locations and the model vector $\underline{m}$. Travel-time from the basal layer, through the ice, is neglected. The residual between the predicted arrival time and the observations is $\Delta\underline{d} = \underline{d}' - \underline{d}$. The model vector is then improved by determining the derivatives of the arrival times predictions with respect to the model parameters. We define the components of the nx3 matrix $\underline{\underline{G}}$ by $G_{ij} = \frac{\partial d_i}{\partial m_j}$ and the requisite model increment is related to the residual by $\Delta\underline{d} = \underline{\underline{G}}\Delta\underline{m}$. The least square solution for the model increment is $\Delta\underline{m} = (\underline{\underline{G}}^T \underline{\underline{G}})^{-1}\underline{\underline{G}}^T \Delta\underline{d}$. We perform 10 iterations of the inversion, adding successive values of $\Delta\underline{m}$ to the previous iteration of $\underline{m}$, to obtain an origin location and time.

The standard deviations for the model vector are determined by $\underline{\sigma}_m^2 = \sigma^2(\underline{\underline{G}}^T \underline{\underline{G}})^{-1}$ [Stein and Wysession, 2003: Section 7.2, Equation 34] where σ is

the standard deviation of the residual vector $\Delta \underline{d}$. Two standard deviations define the 95% confidence interval and are used to define the semi-major axes of the ellipses on Figure 1.

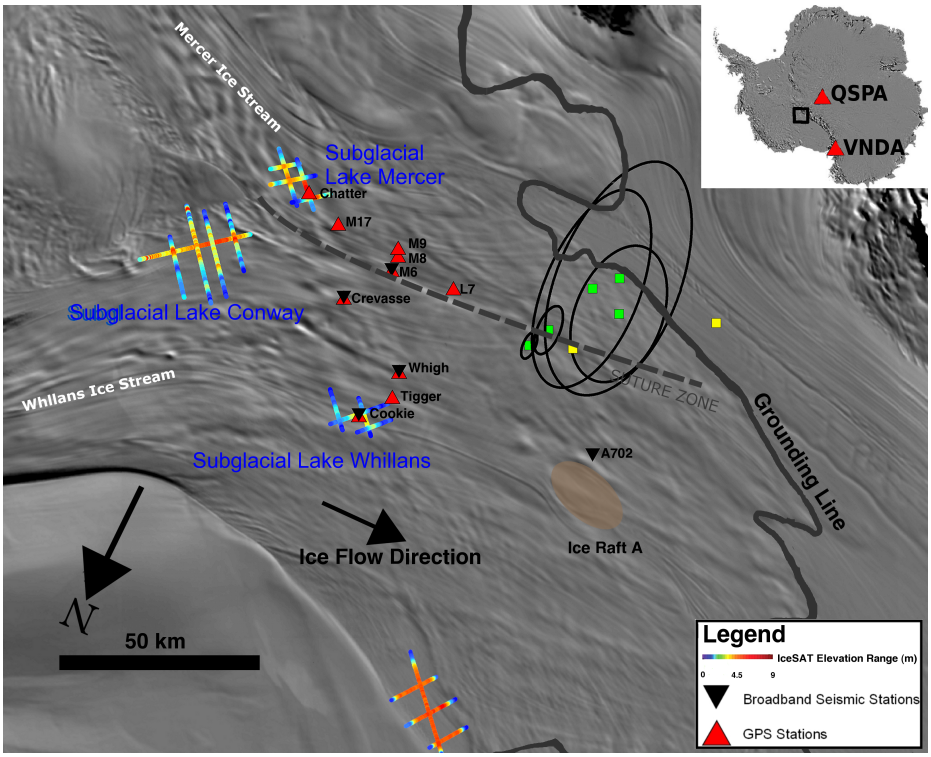

Figure 1: Station location map depicting continuous GPS network and broadband station names for the 2008 field season. Subglacial lake geometry is shown as IceSAT tracks, adapted from Fricker et al. [2007]. Grounding line is shown, adapted from Horgan and Anandakrishnan [2006]. The circles are 95% confidence level error ellipses encircling slip-start locations, shown as green squares. Yellow squares indicate slip-start locations with only three station observations; others have at least four observations. The suture zone location is based on the presence of buried crevasses detected by airborne radar sounding [Shabtaie et al., 1987]. The suture zone is the boundary between Mercer- and Whillans-sourced ice.

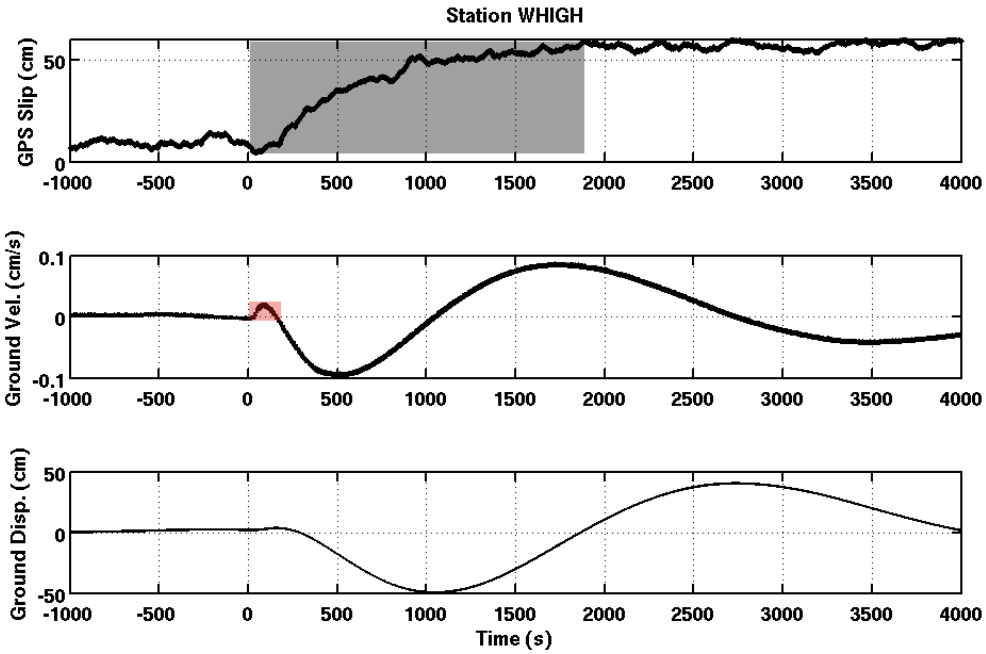

Figure 2: GPS displacement (top), seismic ground velocity (middle) and displacement (bottom) on the east component at a co-located site. Seismic data has been high-pass filtered at 3,000 seconds (0.0003 Hz). Red box indicates the medium-period slip initiation pulse and the grey box encapsulates the total slip and duration of the slip event. Note the comparable displacement amplitudes for the GPS (top) and seismic (bottom). The seismic displacement amplitude is negative near ~1000 seconds because the slip direction is predominantly west.

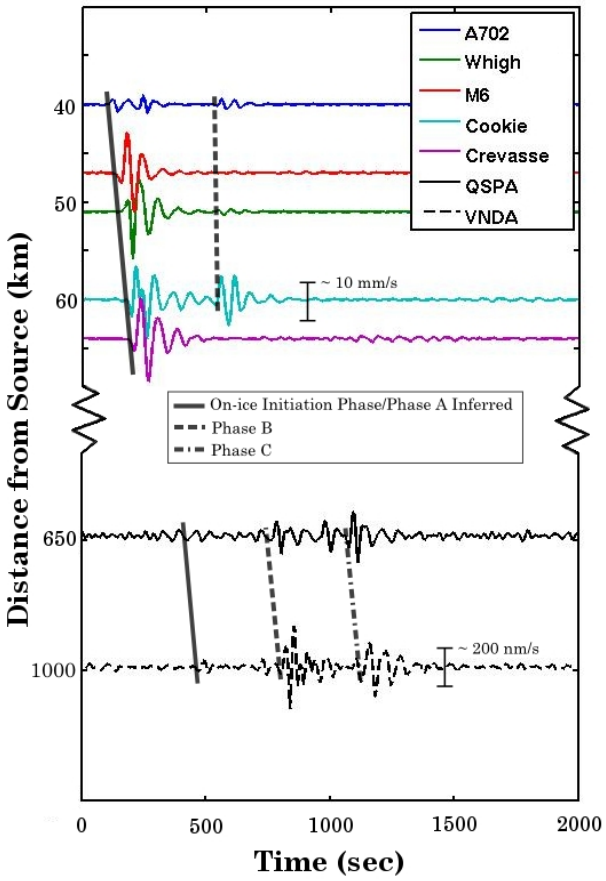

Figure 3: Seismic record section of a single event observed at both on-ice and far-field stations. At the on-ice stations, the initiation phase (solid gray line through color stations) indicates the rupture front propagating across the ice plane and its modeled arrival at far-field stations (most events in 2008 do not transmit sufficient Phase A energy to be detectable above the noise). On-ice, the initiation phase is the seismic energy associated with the passing rupture front (maximum ~ 0.3 km/s) observed at each individual station. In the far-field, Phase A is a seismic wave (~ 3 km/s) associated with the slip-start, which is a distance away from the on-ice stations. A diagram of the rupture process is also found on Figure 4.

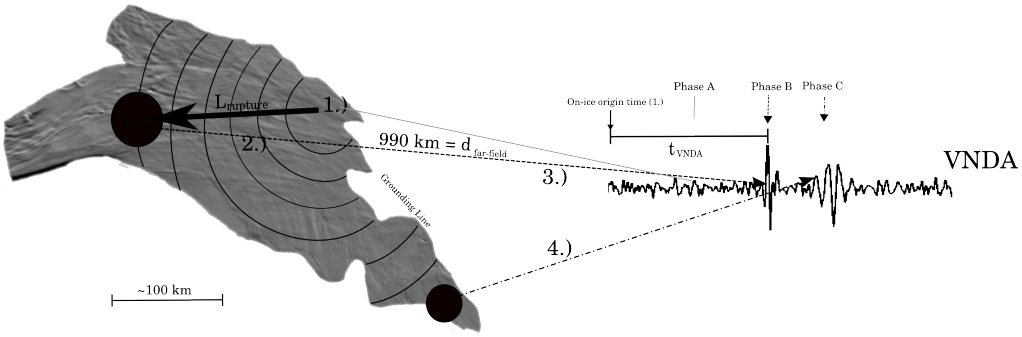

Figure 4: Schematic of method for far-field inference of rupture speed. (1) Rupture initiates at a location adjacent to the grounding line, (2) propagates across the ice at a rupture speed determined by Equation 1, (3) the rupture stops spreading at one stopping point which transmits Phase B of the far-field wave, (4) the rupture stops at another stopping point and transmits Phase C of the far-field wave. The origin time is inferred from the seismic initiation phase at the on-ice stations. The origins of Phases B & C are not constrained and only shown schematically Phase A is weak or unobservable on the example seismogram and the expected arrival time is shown shown for clarity

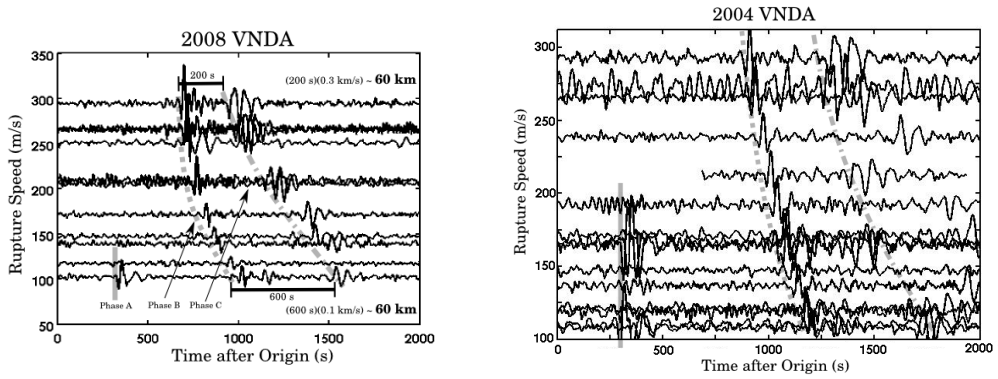

Figure 5: Waveforms of a suite of slip events observed at station VNDA in (a) 2008 and (b) 2004, plotted as a function of rupture speed. The waveforms are adjusted so that the origin (Time = 0) corresponds to the on-ice origin time. If Phase A were visible at station VNDA for all events, that arrival time would be near the 350 second mark. The time difference between Phase B and Phase C arrivals varies linearly with rupture speed, such that an estimated distance of 60 km separates the physical locations of Phase B and Phase C decelerating points.

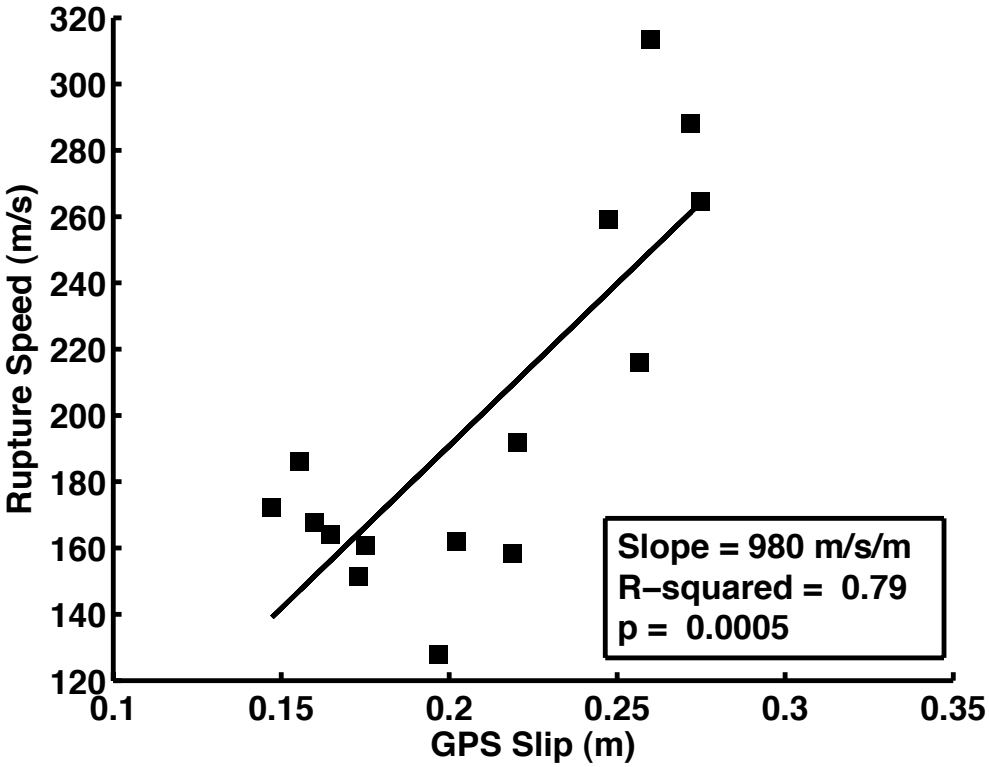

Figure 6: Rupture speed as inferred from the far-field records using Equation 1 and GPS slip measured at station Whigh (See Figure 1 for station locations).

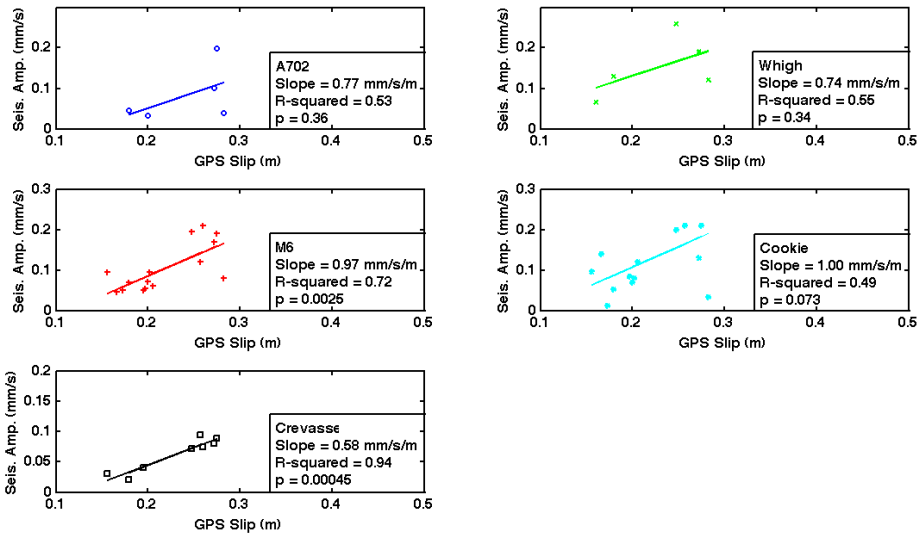

Figure 7: Slip displacement versus amplitudes of the seismic initiation for various stations in our network. The p-value is the probability of the data being uncorrelated. All stations show a strong correlation. Values for slip displacement come from a single GPS station (M8) and represent the average slip for the WIP.

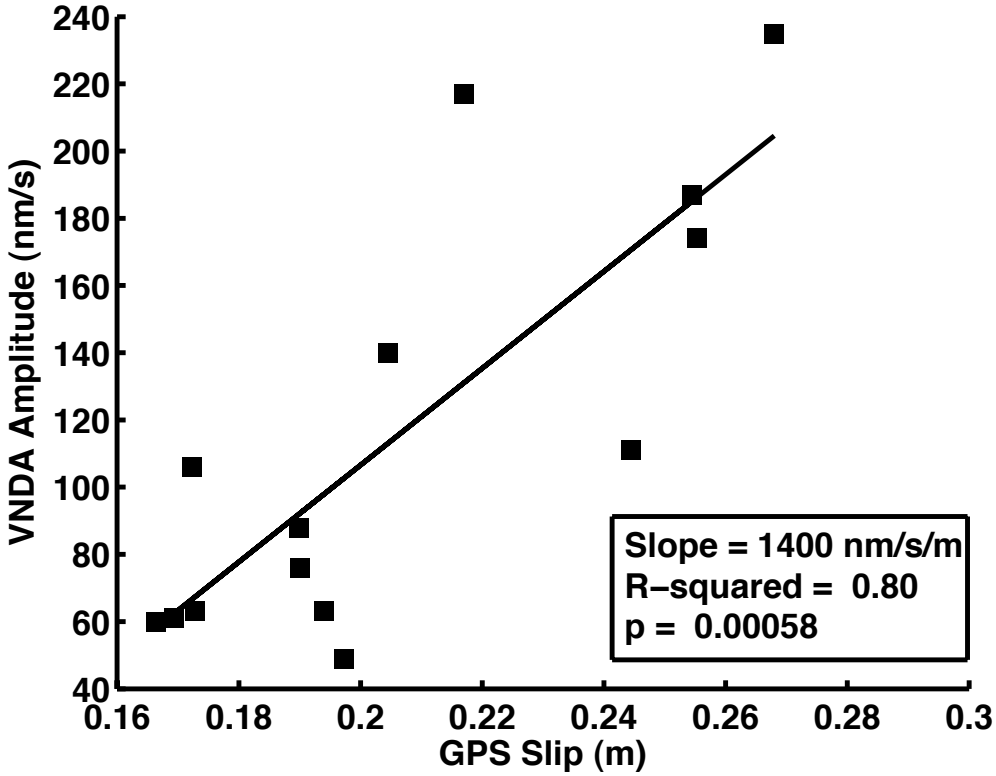

Figure 8: Far-field Phase B amplitude measured at broadband station VNDA and GPS slip.

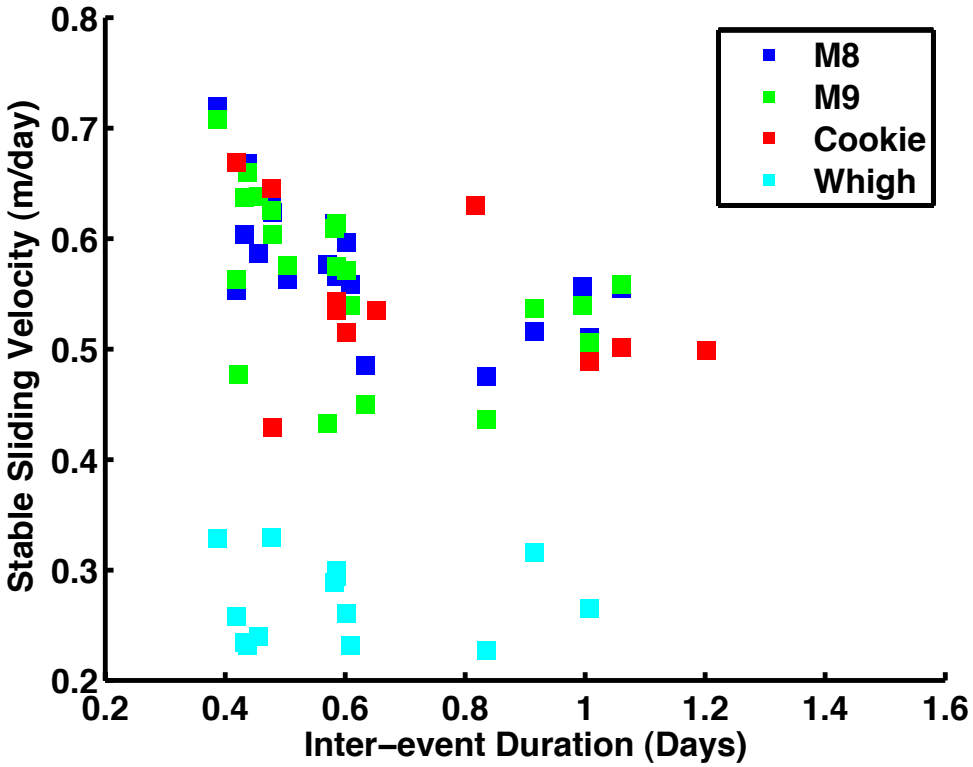

Figure 9: Measured inter-event stable sliding velocity based on GPS data versus inter-event duration.

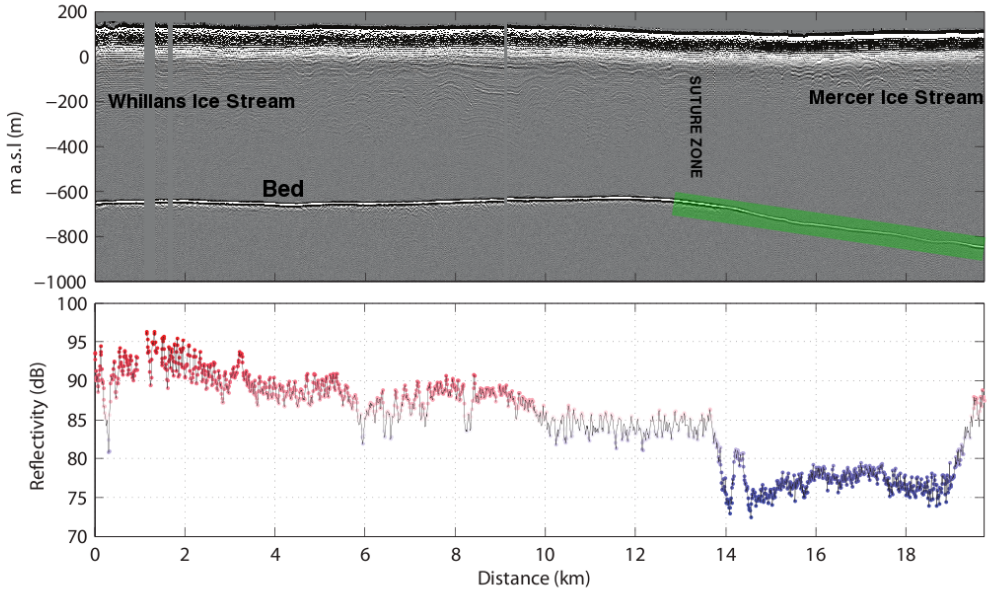

Figure 10: Ice-penetrating radar line collected across a transect from stations M6-M8, continuing southwest. Ice flow direction is directly towards the reader. In the top panel, the green bar indicates the inferred source of slip start locations. In the bottom panel, red indicates high reflectivity and blue indicates low reflectivity. Brighter reflectivity (red) typically indicate the presence of conductive pore water [Raymond et al., 2006].

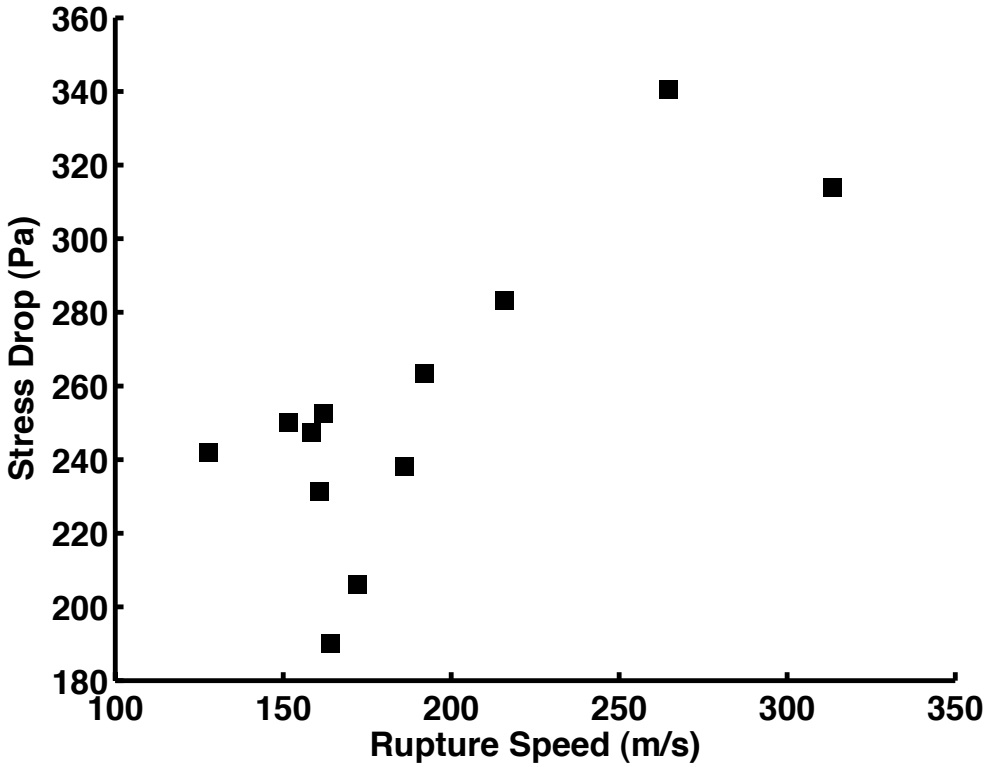

Figure 11: Stress drop plotted as inferred from the GPS slip of Figure 6 and rupture speed. Measurements of GPS slip come from station Whigh.

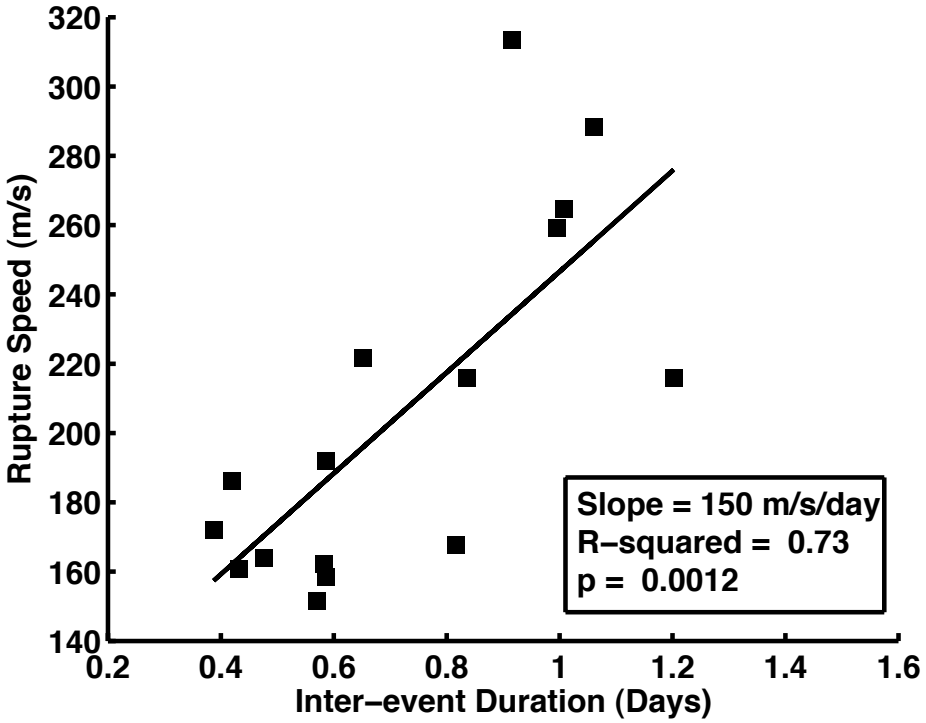

Figure 12: Rupture speed as inferred from the far-field records and inter-event duration.

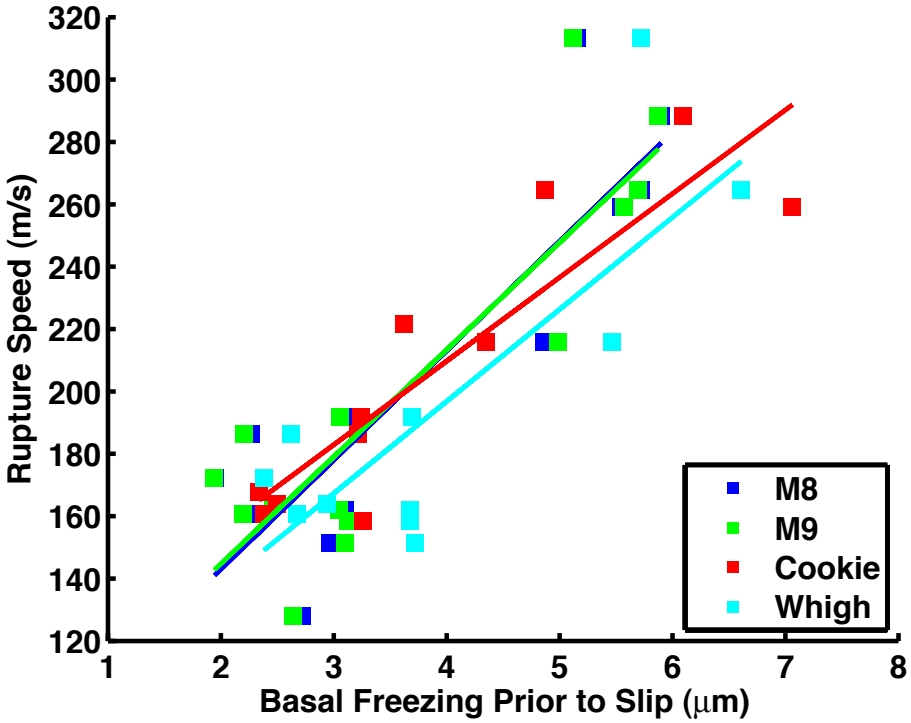

Station	Slope	R^2	p-value
M8	35	0.88	0.000042
M9	34	0.87	0.000059
Cookie	27	0.90	0.00017
Whigh	30	0.81	0.0028

Figure 13: Basal freeze-on calculated from Equation 5 and the GPS data from Figure 9 and rupture velocity for the resultant slip event, inferred from far-field stations. Basal freeze-on is calculated over the duration of inter-event time leading up to the slip event.

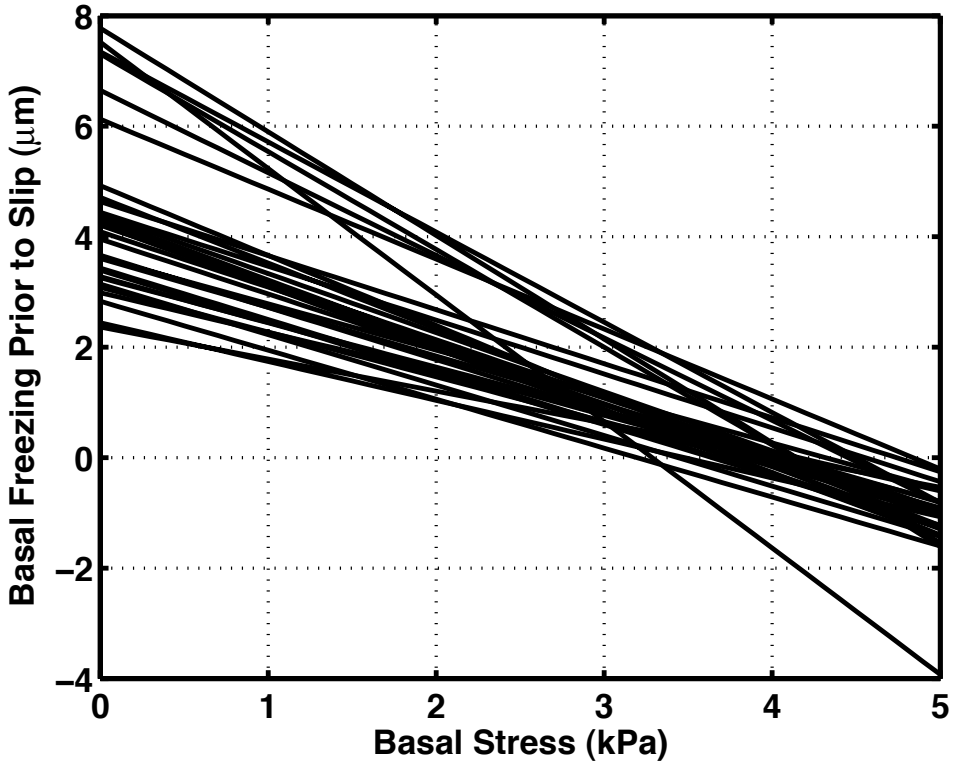

Figure 14: Freezing for a range of inter-event basal shear stress τ_b in Equation 5. This calculation is used to constrain the range of basal shear stresses that are realistic, and as freezing must be positive over the long-term, τ_b must be less than 4 kPa based on the range of velocities we observe. We use observed inter-event velocity, u_b, from station M8.

3. RUPTURE SPEED DEPENDENCE ON LOADING CONDITIONS

3. RUPTURE SPEED DEPENDENCE ON LOADING CONDITIONS

Abstract

The speed of rupture propagation of a supercritical crack along a frictional interface is dependent upon the elastic properties of the materials surrounding the interface. However, the processes controlling rupture velocity of a slower crack are more ambiguous. We present data from a large Antarctic ice stream, Whillans Ice Plain (WIP), which undergoes bi-daily stick-slip events that generate seismic waves observable up to 1000 km away. The WIP flows downhill at a steady rate, then suddenly increases its speed by 2 orders of magnitude at tidal periods, slipping up to ~0.5 m in ~30 min. Previous measurements suggested a variation of average rupture speed by a factor of 2 between events. Using a network of broadband seismometers in a regular grid surrounding the rupture zone, we find that the variable rupture speed may depend upon tidal flexure near the nucleation zone and the local loading conditions of the slipping interface.

3.1. Introduction

3.1.1. Background

Observations suggest that most earthquakes rupture at a rate approaching the shear wave speed of the rocks through which they propagate (Kanamori and Brodsky, 2004). Though when shear is driven in the laboratory, detailed measurements suggest rupture speed may be controlled by interfacial loading conditions (Ben-David and

Feinberg, 2011). Variations in loading conditions in the laboratory are measured concentrations of increased interfacial shear and normal stresses.

Some evidence suggests that earthquake rupture can sometimes surpass the limiting shear wave speed, in supershear ruptures (Dunham and Archuleta, 2004). At the other limit of rupture speed observations, the discovery of the prevalence of slow slip at subduction zones has caused increasing focus on ruptures that propagate well below the shear velocity of an interface (e.g. Segall et al., 2010). Glaciers undergo a similar slip initiation process as earthquakes (Walter et al., 2011) and their slower propagation may allow us to study the rupture process more easily than during an earthquake.

In West Antarctica, bi-daily stick-slip events occur beneath the Whillans Ice Plain (WIP), which is an area downstream of the Whillans (WIS) and Mercer Ice Streams (MIS). This area has a relatively low driving stress of 3 kPa and a basal shear stress of 1 kPa (Joughin et al., 2002). Though tidal stresses imparted by ocean tides on the WIP are only on the order of 0.4 kPa (Bindschadler et al., 2003), they are able modulate the flow of the WIP due to the low background stresses. This sub-daily modulation of flow is manifested as stick-slip motion at the basal interface, where the ~150 km long x ~100 km wide x ~800 m thick WIP moves up to 0.5 m in approximately 30 min, every 6-18 hours. The rupture front propagation during the slip events can be tracked using broadband seismometers (Walter et al., 2011).

3.1.2. Basal friction

Shear failure along a fault or at the base of a glacier occurs when the shear stress locally exceeds a failure threshold or the yield stress. For Coulomb friction, the failure stress, τ_f, equals a coefficient of friction, μ_s, times the normal stress, σ_n,

$$\tau_f = \mu_s \sigma_n \qquad (1)$$

In saturated sediments whose particle framework is more compressible than water (Mitchell, 1993) the normal stress term is replaced by the normal effective stress, σ'_n, which is normal stress on the shear interface minus the pore pressure, p_w,

$$\tau_f = \mu_s (\sigma_n - p_w) \qquad (2)$$

Increasing water pressure lowers the normal effective stress and thus lowers the yield stress, promoting failure along the slip plane. Conversely, till that is well-drained and has lower pore pressure, would be relatively stronger.

The WIP stick-slip events occur with repeat intervals between 6-18 hours, dependent upon the tidal loading. The tidal forcing contributes stresses on the order of 0.1 kPa (Bindschadler et al., 2003; Winberry et al., 2009). Small stresses driving failure suggests a weak basal interface and an inherently weak till. When WIS tills have been directly sampled, shear box measurements indicate a low yield stress of only a few kPa (Kamb, 1991). Furthermore, shear tests on tills are in general agreement with force balance estimates of basal shear stress of 1.1 ± 0.9 kPa (Joughin et al., 2002). Glacier till retrieved from mountain glaciers also behaves as a

Coulomb-plastic material (Iverson et al., 1998), suggesting that Coulomb-plastic till rheology may be a ubiquitous feature of glacier flow.

3.1.3. Spatially heterogeneous static friction

Large spatial concentrations of increased basal shear stress exist and are manifested as 'sticky spots' at the base of ice streams (Alley, 1993; Clarke et al., 2007). One such sticky-spot for nucleation of the WIP events may be near the grounding line (Walter et al., 2011; Figure 1).

Laboratory pre-consolidation tests on tills recovered from the WIS indicate in-situ effective stress of ~10 kPa (Tulaczyk et al., 2001). Such a low effective stress in tills under ~800 m of ice overburden suggests porewater pressure has an important role in subglacial tills. Therefore, if we assume that tills that have high porewater content and pressure generally underlie the active ice streams, the availability and flow of excess porewater may be sufficiently spatially variable to permit a spatial variability in till strength. Beneath polar ice sheets, liquid water is driven from high to low hydropotential (Shreve, 1972), which is typically calculated from

$$\phi = \rho_i g(H - z) + \rho_w g z \qquad (3)$$

where ϕ is the hydropotential, ρ_i and ρ_w are the densities of ice and water, g is the acceleration of gravity, and H is the elevation of the glacier surface. At the base of the WIP, porewater is plausibly driven away from hydropotential highs, which may then become 'sticky spots' in the form of patches of stronger subglacial till (Alley, 1993).

3.2. Observations

In the austral summer of 2010, we installed an array of 11 broadband seismometers on the Whillans Ice Plain, West Antarctica (Figure 1). Station S10 is located adjacent to Ice Raft A and S02 is located on Subglacial Lake Whillans. Also, it is worth noting that stations S03 and S07 are located on ice that flows from Mercer Ice Stream, as a suture zone is visible in the MODIS imagery in Figure 1.

3.2.1. Rupture speed

We compare the conditions for slip event nucleation (Figures 2a and 2b) with observations of rupture initiation and propagation, shown in Figures 2c and 2d. Figures 2c and 2d show arrival time contours for the mean of all events that either initiate on low tide or high tide. The sign from the tide level output of the Padman et al. (2003) inverse tidal model for the Ross Sea determines whether an event is defined as low (negative) or high (positive) tide. Generally, the observations show that slip events nucleate in the region of higher seismic coupling, which may be a basal condition that is determined by the relatively high hydropotential in the region.

Walter et al. (2011) showed that the average rupture speed of events linearly correlated with the inter-event period (recurrence interval). We perform a similar analysis here using arrival of the stopping phase at an on-ice station rather than relying on the sporadic arrivals at station VNDA in the Dry Valleys. We perform delay-and-sum beamforming (e.g. Rost and Thomas, 2002) for 4 of 44 events, to determine the azimuth and velocity of the stopping phase arrival (See supplemental methods for more information and verification with synthetic data). The restricted

number of analyzed events is due to the low amplitude stopping phase for the on-ice stations. Only stacked beams with signal-to-noise ratio (SNR) greater than 10 are considered sufficiently high amplitude to be included in the analysis. The mean azimuth for the 4 of 44 events with a clear stopping phase signal is 196 ± 11°.

We assume that the rupture propagates to a barrier at the edge of fast-moving ice, defined by the limits of ice stream motion (e.g. Joughin et al., 2002), and along the azimuth determined by beamforming. The inferred location in the direction of that beam is shown in Figure 1. The location of the stopping phase differs from the assumed location of the stopping phase in Walter et al. (2011), which was located adjacent to the area where Whillans Ice Stream flows into the WIP. This discrepancy is likely due to a lack of stations and limited station aperture in that study (Walter et al., 2011).

If we infer a rupture length from the nucleation region to the stopping phase, we can calculate a rupture speed from the observed travel-times. The rupture speed is

$$V_{rupture} = \frac{L_{rupture}}{t_{S11} - \frac{d_{PhaseB-S11}}{V_{Rayleigh}}} \qquad (4)$$

where $V_{Rayleigh}$ is the Rayleigh wave speed in ice inferred from beamforming (1.8 km/s), $d_{PhaseB\text{-}S11}$ is the distance to station S11 observing the stopping phase (75 km), $L_{rupture}$ is the length of rupture from station S03 or S08 to the stopping phase (90 and 93 km, respectively), and t_{S11} is the difference in time between the origin time and arrival of Phase B at station S11. By correcting for travel-time to the Phase B

observation station, S11, we determine the average rupture speed for each event, which is shown in Figure 3a.

Close examination of Figures 2c and 2d indicates that events occurring during different tides rupture at different near-source velocities. In order to quantitatively show this, we compute the apparent rupture speed from either S03 or S08 (depending on low or high tide event), to S11 for a series of events. Figure 3b shows that slip events that begin at low tide, propagate at much faster speeds towards S11 than high tide events. In Figure 3b, we connect apparent rupture speeds with the red vertical lines to the average rupture speed (Values from Figure 3a). This relationship indicates that once the slipping region propagates outside the seismic network, the average rupture speed scales with inter-event period, an observation consistent with data recorded during 2008 and reported by Walter et al. (2011).

3.2.2 Relationship to hydropotential and inter-event strain accumulation

Figure 2a depicts a map of hydropotential using the Bamber DEM (Bamber et al., 2001) at 2.5 km resolution in the vicinity of our seismic stations from the 2010 field season. Note that in Figures 2c and 2d that the slip events nucleate generally near a feature of relatively higher hydropotential, slightly eastward of S03. If liquid water transport occurs away from hydropotential highs and the till across the WIP is lithologically similar, then the till below the nucleation region might have a higher yield stress and accumulate more shear strain than adjacent areas.

The continuous displacement record from the GPS stations provides a diagnostic tool for determining variations of inter-event strain accumulation. Inter-event sliding occurs at varying rates across the WIP (Walter et al., 2011; Winberry et al., 2011) with less sliding occurring at stations proximal to the nucleation region. In order to evaluate the average inter-event sliding that occurs, we define seismic coupling for glaciers in analogy to the seismic coupling of faults (e.g. Ruff and Kanamori, 1983). Unlike most faults, seismic coupling and its spatial variability can be measured directly and averaged over multiple cycles. Here we define the local seismic coupling at a station as the total displacement that occurs at each GPS station over a 14-day period divided by the total displacement that occurs during the slip events over that time period. We assemble a dataset that assimilates two separate GPS campaigns collected during the TIDES experiment in 2004-2005 and a project to investigating subglacial lake activity spanning the years 2007-2012. For each experiment, we choose a single 14-day period when the highest amount of stations are operating, and compute the seismic coupling. For the TIDES data, we compute the seismic coupling spanning days 332-346 in 2004 and for the other experiment, we compute the seismic coupling spanning days 339-353 in 2008. Figure 2b shows the spatially interpolated pattern of seismic coupling that occurs in between slip events.

3.2.3. Relationship to tide near the grounding line

For the majority of events that occur during low tide, the first rupture front arrival occurs at station S03 before it is observed at other stations and spreads across

the network. Similarly, for the majority of events that occur during high tide, the first rupture front arrival occurs at S08. We conjecture that the flexure of ice at the grounding line imposes a time-varying normal effective stress on different regions of the basal interface.

We constrain how far stresses can be propagated inland by considering the ice near the grounding line as an elastic beam under a line load, with a Young's modulus of ice, E, of 5 GPa (Gudmundsson, 2011), a thickness, h, of 800 m (Christianson et al., 2012), Poisson's ratio, υ, of 0.37 (Ewing et al., 1934), a density of ice, ρ_i, of 917 kg/m^3, and density of seawater, ρ_w, of 1025 kg/m^3. Using these general properties for ice, we can constrain the distance between the loading point (where x=0, indicated in Figure 4 by w_0) and the position of the forebulge, x_b (Figure 4). For a line load at the end of a beam, x_b is related to the flexural parameter, α, where $x_b=\alpha 3\pi/4$ (Turcotte and Schubert, 2002; Equation 3-144). The flexural parameter, α, is given by Turcotte and Schubert (2002; Equation 3-127)

$$\alpha = \left[\frac{4D}{g\Delta\rho} \right]^{1/4} \qquad (5)$$

where g is the gravitational acceleration (9.81 m/s^2), $\Delta\rho$ is the density difference between seawater and ice, and D is the flexural rigidity (Turcotte and Schubert, 2002; Equation 3-72)

$$D = \frac{Eh^3}{12(1-\upsilon^2)} \qquad (6)$$

We compute the distance between the loading point where x=0 and the forebulge, x_b, for a line load to be about 14 km. The distance between station S03 and S08 is approximately 13 km.

If we consider the cross-section of tidal flexure across the grounding line (Figure 4), then during high tide, the maximum downward deflection is inland, which is consistent with ruptures originating near S08. During low tide, the maximum downward deflection is close to loading point (w_0), and is consistent with ruptures originating near S03 (closer to the grounding line).

3.3. Discussion

3.3.1. Spatial variations of basal conditions over tidal loading cycle

The slip events nucleate in a region where the hydropotential is slightly higher than adjacent regions to the north, plausibly in an area of stronger till, and adjacent to the grounding line. Tidal flexure influences the spatial variability of ruptures, initiating failure at different points depending upon the tide. After nucleation reaches a critical size, unstable sliding begins and propagates across the Ice Plain. Past the nucleation region, Figure 3a suggests that the rupture propagates at a speed that is correlated with inter-event duration (recurrence interval), consistent with observations from a previous experiment (Walter et al., 2011).

When considering deflection of ice near the grounding line, if ice deformation is directed towards the ice/till interface, then the normal stress acting on the bed should increase. Such a downward stress is on the order of $\sim \Delta \rho g w$. A tide prediction

model for this area (Padman et al., 2003) predicts tides ranging from -1.5 to 1.5 m. If we consider the minimum tide (-1.5 m), then the normal stress increase is about 1.5 kPa. The forebulge deflection also imparts a normal stress, in the opposite sense and an order of magnitude less. For either type of event, where the normal stress is increased by the downward deflection of the ice, the slip event nucleates either closer to the grounding line for low tide events or further from the grounding line for high tide events.

Whether such an increase in normal stress alters the normal effective stress is dependent upon drainage conditions in the till. If the till is completely undrained, then any increase in the normal stress causes an equivalent increase in the porewater pressure, thus leaving the effective normal stress unchanged. Alternatively, in the completely drained case, increases in the normal stress lead to an equivalent increase in the normal effective stress.

We may gain some insight by considering the hydraulic diffusivity of the tills beneath WIS. We compute the penetration depth for till over a tidal loading cycle by $z \sim \sqrt{\kappa t}$, where κ is the hydraulic diffusivity of till, measured to be 10^{-8} m/s^2 for sub-WIS tills (Tulaczyk et al., 2000), and t is the tidal loading timescale, which we assume to be a minimum ~12 hours. The resultant diffusional skin depth is on the order of 2 cm. Such a small value suggests that the till may be undrained, though the lack of direct measurements limits our ability to accurately identify the controlling mechanism. Determining the influence that flexure has in altering the normal effective stress at the grounding line awaits further measurements, yet, the

observation of alternating nucleation zones suggests that flexure alters the loading conditions at the ice/till interface.

3.3.2 Dynamic considerations for rupture speed

The WIP stick-slip events propagate on an interface with dissimilar elastic properties. Active source experiments performed at a location upstream of the WIP indicate a shear wave speed of ice of ~1900 m/s and a shear wave speed of till of ~170 m/s (Blankenship et al., 1987). Such a high contrast in elastic properties increases the difficulty of predicting the rupture velocity from inferences in the earthquake literature. Though the nature of the interface may suggest that the ice/till contact behaves fundamentally different than interfaces with similar elastic properties, such as those on faults, we also consider insight from rock mechanics.

Slip instability in such a stick-slip system occurs when the following condition is met (Rabinowicz, 1951; Scholz, 2002)

$$\frac{(\mu_s - \mu_d)\sigma_n}{D_c} > K \qquad (7)$$

where μ_s and μ_d are the static and dynamic coefficients of friction, σ_n is normal stress, D_c is the critical slip distance to transition from static to dynamic friction, and K is the system stiffness, analogous to a spring stiffness. In Equation 7, when normal stress is increased during a tidal loading cycle, it promotes a transition to stick-slip instability and initiates rupture propagation across the Ice Plain.

As the rupture continues to propagate across the Ice Plain, its average rupture speed scales with inter-event duration. Generally, frictional surfaces heal and μ_s increases approximately logarithmically with time (Rabinowicz, 1951). In the case of the WIP, sliding displacements that occur in between events are negatively correlated with inter-event duration (Walter et al., 2011); short recurrence interval events creep faster. Thus, the scaling of average rupture speed with inter-event duration (Figure 3a) may also depend upon the ratio on the left-hand side of Equation 7.

3.4. Conclusions

We have shown that spatial variations in hydropotential and observed frictional locking of the ice stream base may constrain the location of rupture event nucleation. Further, the flexure of the ice near the grounding line can modulate the normal stress at the base of ice and may alter the normal effective stress at the ice/till interface. However, identifying the precise loading conditions due to ice flexure requires more observations of the drainage behavior. Nonetheless, the flexure geometry is consistent with events that nucleate in different regions, with respect to the tide. Once slip events propagate past the nucleation region, their rupture speed is dependent upon the amount of inter-event time. Therefore, the rupture speed of stick-slip sliding may be sensitive to variations in the local loading conditions at the sliding interface, in both the nucleation zone and areas the rupture event propagates through.

3.5. Acknowledgements

This work was funded primarily by NSF Antarctic Sciences Division Grant

number 0636970. A NASA Earth and Space Science Fellowship provided support for J.I.W. We would like to thank Sasha Carter for providing the 2.5 km hydropotential map. The GPS stations were provided by the UNAVCO Facility with support from the National Science Foundation (NSF) and National Aeronautics and Space Administration (NASA) under NSF Cooperative Agreement No. EAR-0735156. Some of the instruments used in the field program were provided by the PASSCAL facility of the Incorporated Research Institutions for Seismology (IRIS) through the PASSCAL Instrument Center at New Mexico Tech. Data collected during this experiment will be available through the IRIS Data Management Center. The facilities of the IRIS Consortium are supported by the National Science Foundation under Cooperative Agreement EAR-0552316 and by the Department of Energy National Nuclear Security Administration.

References

Ben-David, O. and J. Fineberg (2011), Static friction coefficient is not a material constant, Phys .Rev. Lett., 106, 254301.

Bindschadler, R. A., M. A. King, R. B. Alley, S. Anandakrishnan, and L. Padman (2003), Tidally controlled stick-slip discharge of a West Antarctic ice stream, Science, 301, 1087–1089, doi:10.1126/science.1087231.

Bindschadler, R., H. Choi, A. Wichlacz, R. Bingham, J. Bohlander, K. Brunt, H. Corr, R. Drews, H. Fricker, M. Hall, R. Hindmarsh, J. Kohler, L. Padman, W. Rack, G. Rotschky, S. Urbini, P. Vornberger, and N. Young (2011) Getting around Antarctica: New High-Resolution Mappings of the Grounded and Freely-Floating Boundaries of the Antarctic Ice Sheet Created for the International Polar Year. The Cryosphere, 5, 569-588. doi:10.5194/tc-5-569-2011.

Blankenship, D. D., C. R. Bentley, S. T. Rooney, and R. B. Alley (1987), Till beneath Ice Stream B: I. Properties derived from seismic travel times, J. of Geophys. Res., 92(B9), 8903-8911.

Christianson, K., R.W. Jacobel, H.J. Horgan, S. Anandakrishnan, R.B. Alley (2012), Subglacial Lake Whillans – Ice-penetrating radar and GPS observations of a shallow active reservoir beneath a West Antarctic ice stream, Earth and Planetary Science Letters, 331, pp. 237–245.

Dunham, E. M. and R. J. Archuleta (2004), Evidence for a supershear transient during the 2002 Denali Fault earthquake, Bulletin of the Seismological Society of America, 94(6B), S256-S268, doi:10.1785/0120040616.

Ewing, M., A. P. Crary, and A. M. Thorne (1934), Propagation of elastic waves in ice, Part 1, Physics, 5.

Joughin, I., S. Tulaczyk, R. Bindschadler, and S. F. Price (2002), Changes in west Antarctic ice stream velocities: Observation and analysis, J. Geophys. Res., 107(B11), 2289, doi:10.1029/2001JB001029, 2002.

Mitchell J.K. (1993), Fundamentals of soil behavior, Second Edition, University of California, Berkeley. John Wiley & Sons, Inc. 437p.

Padman, L., S. Erofeeva, and I. Joughin (2003), Tides of the Ross Sea and Ross Ice Shelf cavity, Antarct. Sci., 15(01), 31-40.

Rabinowicz, E. (1951), The nature of the static and kinetic coefficients of friction, J. Appl. Phys., 22: 1373-1379.

Rost, S., and C. Thomas (2002), Array seismology: methods and applications, Reviews of Geophysics, 40, 3.

Scholz, C. H. (2002), The Mechanics of Earthquakes and Faulting, 2nd Edition, Cambridge University Press.

Segall, P., A. M. Rubin, A. M. Bradley, and J. R. Rice (2010), Dilatant strengthening as a mechanism for slow slip events, J. Geophys. Res., 115, B12305, doi:10.1029/2010JB007449.

Turcotte, D.L., and G. Schubert (2002), Geodynamics, Cambridge University Press.

Walter, J. I., E. E. Brodsky, S. Tulaczyk, S. Y. Schwartz, and R. Pettersson (2011), Transient slip events from near-field seismic and geodetic data on a glacier fault,

Whillans Ice Plain, West Antarctica, J. Geophys. Res., 116, F01021, doi:10.1029/2010JF001754.

Winberry, J. P., S. Anandakrishnan, R. B. Alley, R. A. Bindschadler, and M. A. King (2009), Basal mechanics of ice streams: Insights from the stick-slip motion of Whillans Ice Stream, West Antarctica, J. Geophys. Res., 114, F01016, doi:10.1029/2008JF001035.

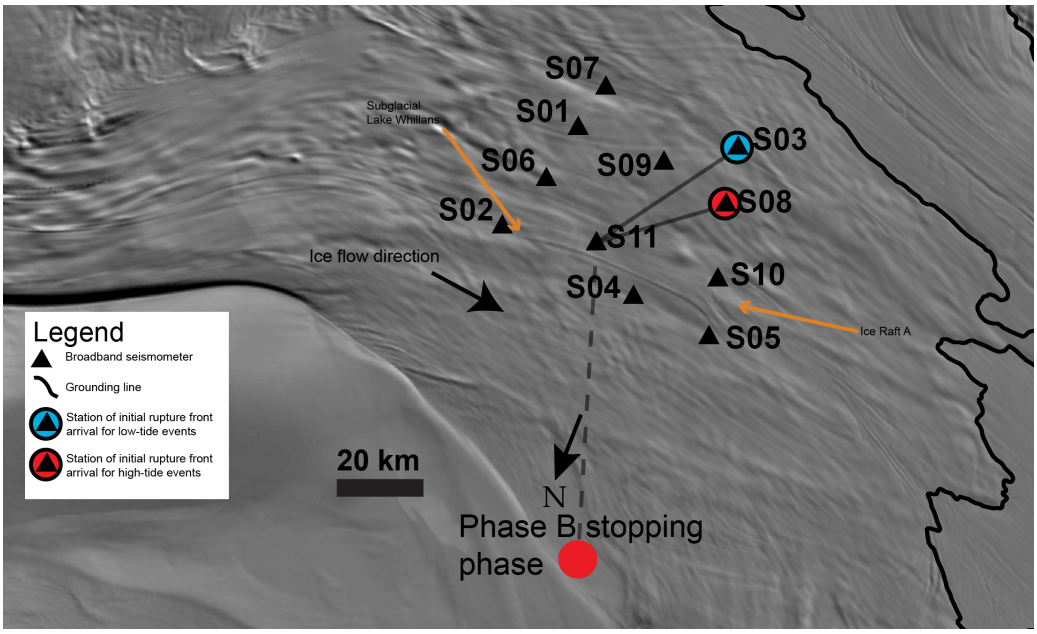

Figure 1: Locations of stations deployed during the 2010 field season, including relative locations of the grounding line, Ice Raft A and Subglacial Lake Whillans. The rupture front is initially observed at station S03 for low tide events. The rupture front is initially observed at station S08 for high tide events. Solid and dashed lines are used to indicate distances over which rupture speeds are calculated. Grounding line is the ASAID grounding line (Bindschadler et al., 2011).

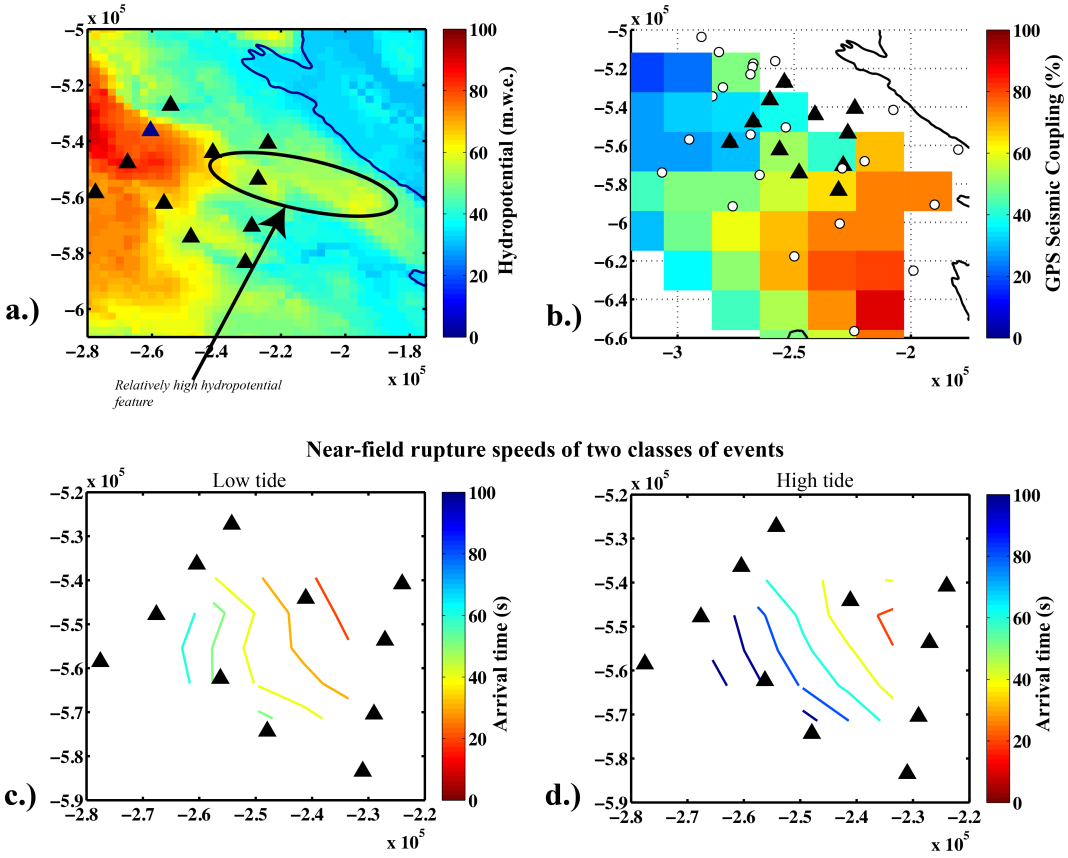

Figure 2: Slip event nucleation geometry using the broadband seismometer network from the 2010 field season, and their relationship with areas of (a.) hydropotential highs, from which porewater is theoretically driven away (b.) high inter-event loading from continuous GPS (GPS stations are white circles), and (c. and d.) average arrival time contours for each of the two populations of events, including for (c.) low-tide and (d.) high-tide events.

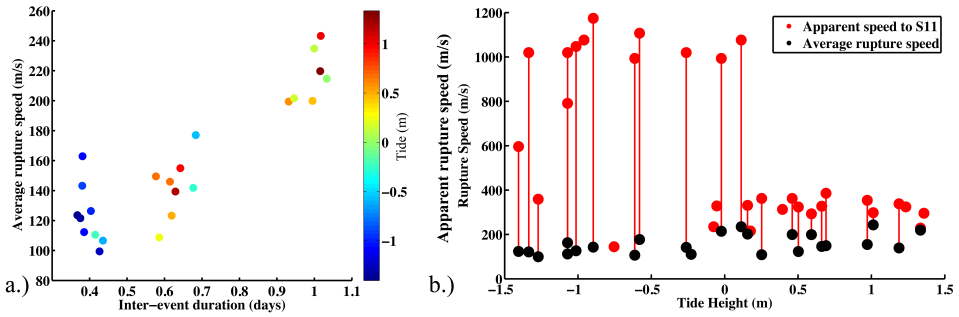

Figure 3: Rupture speed estimates using rupture front arrival and stopping phase arrival time information at station S11. Figures show (3a.) average rupture speed from nearest station to stopping phase B (see Figure 1) and (3b.) average rupture speed as in Figure 3a connected by vertical red lines with measurements of apparent ruptures speed, with tide height at time of slip event initiation on the x-axis. Figure 3b suggests a fundamental difference in rupture for low- versus high-tide events.

Figure 4: Schematic of flexure cross-section under a line load and assumptions for flexure calculation near the grounding line.

3.6. Supplemental Methods S1: Beamforming

As described in Section 2.1 we utilize delay-and-sum beamforming to determine the azimuth and speed of the stopping phase seismic wave, which allows for the calculation of average rupture speed on the ice. Beamforming is useful when the source location and/or propagation velocity are unknown or poorly constrained. We construct a beam for each of 360 degrees, j, of source locations surrounding our 2010 network. We loop through apparent wave velocities, v, from 1200 to 2600 m/s at 100 m/s intervals and compute the slowness, **u**, for each azimuth by

$$\begin{aligned}\mathbf{u} &= (u_x, u_y) \\ &= \left(\frac{\sin\theta}{v}, \frac{\cos\theta}{v}\right)\end{aligned} \qquad \text{(S1)}$$

The waveforms from all 11 stations, y_i, are time-shifted according to the travel-time for a particular plane wave apparent velocity relative to a point at the center of the array. We stack the seismograms at each of these iterations in j, to produce the beam, $B_j(t)$, at that azimuth, where

$$B_j(t) = \sum_{i=1}^{N} y_i(t + \mathbf{r}_i \cdot \mathbf{u}) \qquad \text{(S2)}$$

We take the maximum amplitude at each azimuth, j, for iterations of v.

In order to test the performance of the beamforming algorithm, we prescribe an origin location, produce synthetic "seismograms," then beamform the synthetic data. For the seismograms, we produce a cosine impulse function with duration of 20 s and add sine functions with random periods (using MATLAB's random number generator) for each of the 11 stations. Using the geometry of the 2010 network and

the prescribed location (Figure S1a), we compute the expected time delay for a wave speed of 1800 m/s and shift the synthetics accordingly (Figure S1b). We beamform the data, as described previously, and produce the polar plot in Figure S1c. The recovered backazimuth is 346°, which is roughly consistent with the prescribed origin of the synthetic source, whose azimuth from the center of the array is 348°.

The maximum beamforms of stopping phase B (S2a) are shown on the polar plot in Figure S2b. The highest amplitude stack for this event is at an azimuth of 189° with an apparent velocity of 1600 m/s. Blankenship et al. (1987) report a shear-wave speed in ice of ~1900 m/s, and so our inference of a stopping phase wave speed of 1600 m/s is consistent with the velocity of a surface wave through ice. Beams with stacked amplitude greater than 1500 mm/s are considered sufficiently high amplitude to be included in the analysis. The mean azimuth for 4 of 44 events with sufficiently high amplitude is 196 ± 11°.

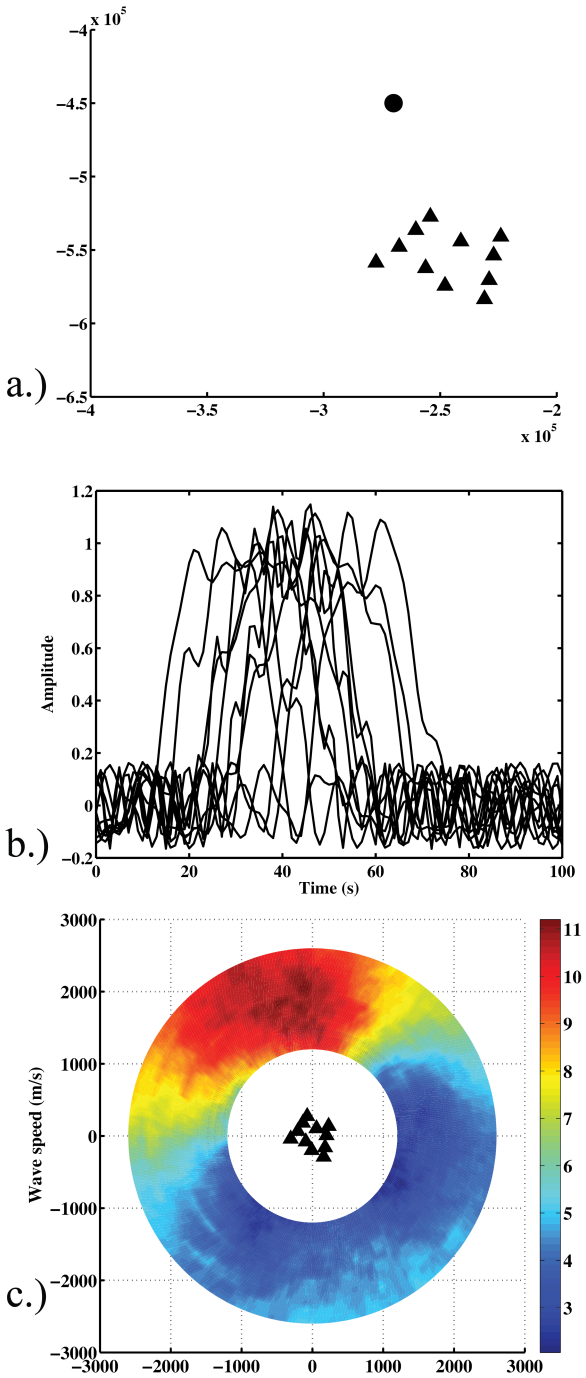

Figure S1: Example of beamforming method on synthetic data, including (a.) location of synthetic origin relative to station geometry, (b.) example seismograms for the 11 stations with random noise, and (c.) polar plot showing the synthetic beamform. Colorbar indicates relative amplitude of stacked signals.

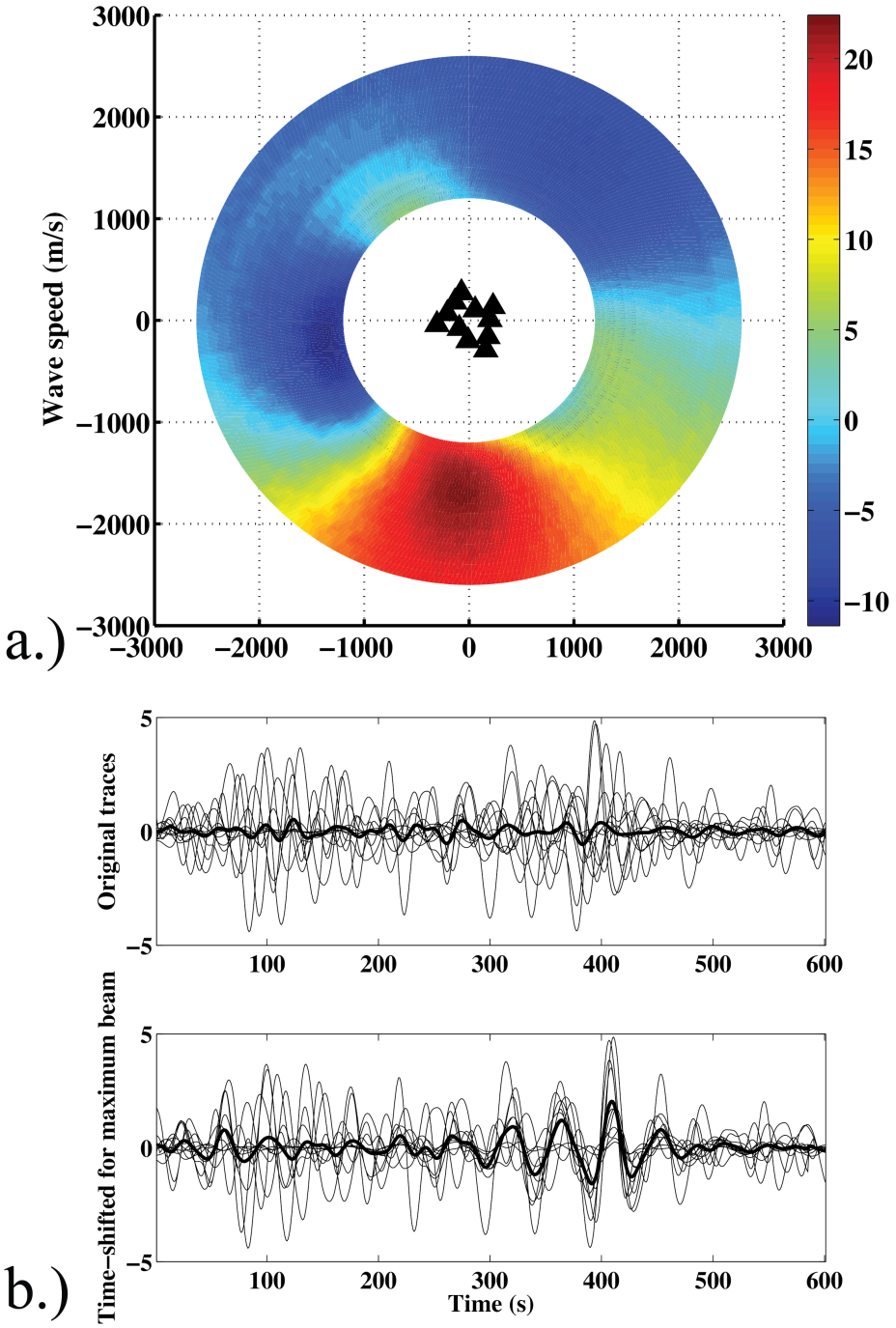

Figure S2: Example of beamforming method, including (a.) polar plot showing the beamform for a single event and (b.) example seismograms for raw seismograms and time-shifted seismograms corresponding to the maximum beam amplitude. Heavy dark lines indicate linear stack of seismograms, divided by the number of stations.

3.7. Appendix A: Maxwell time for ice loading on tidal timescales

In the Chapter 3, when employing flexure as a mechanism for controlling nucleation of events near the grounding line of the Whillans Ice Plain (WIP), we assume that the ice is elastic over tidal loading timescales. In Chapter 4, we investigate speed perturbations that propagate upglacier by changing tides near the terminus of a Greenland tidewater glacier. In the analysis in Chapter 4, we analyze speed perturbations that propagate upglacier using a viscous flow law. In this brief appendix, we will show that these different analyses are appropriate for each situation because the Maxwell time of ice is sensitive to temperature and non-linearly dependent upon effective stress. Effective stress is the relevant deformation stress of the ice, which we define as the driving stress for the analysis here.

To evaluate the appropriate rheology for each situation, we compute the Maxwell time, which is the characteristic time that distinguishes whether a visco-elastic material behaves either elastically or viscously. The Maxwell time, t_*, is the ratio of the effective viscosity, η, to the shear modulus of ice, μ,

$$t_* = \frac{\eta}{\mu} \qquad \text{(A1)}$$

In order to calculate the Maxwell time, we need to compute the effective viscosity and shear modulus of ice.

A more general form of the relationship between stress and strain rate of a Newtonian viscous material is

$$\tau = 2\eta\dot{\varepsilon} \qquad \text{(A2)}$$

where τ is stress, η is the dynamic viscosity, and $\dot{\varepsilon}$ is the strain rate. When sheared in the laboratory, the deformation of ice follows a power law where the stress evolves non-linearly with strain rate, such that

$$\dot{\varepsilon} = A\tau^n \qquad \text{(A3)}$$

where $\dot{\varepsilon}$ is the strain rate, A is a flow parameter that is sensitive to temperature, τ is stress, and n is an exponent, constrained empirically by Glen (1955) to be about 3.17, commonly assumed in ice flow models to be 3. We use a value of 3 in this analysis.

Combining equations A2 and A3, the equation for effective viscosity of ice as a function of effective stress is

$$\eta = \frac{\tau^{1-n}}{2A} \qquad \text{(A4)}$$

From equation A4, we calculate values of effective viscosity, η, over a range of effective stresses, for two values of A, 0°C and -10°C. We approximate Greenland ice as having a value of A = 68 (10^{-16} s^{-1} kPa^{-3}) for ice temperature of 0°C, while for Antarctica ice we assume a value of A = 4.9 (10^{-16} s^{-1} kPa^{-3}) for ice temperature of -10°C (Paterson, 1994; Table 5.2).

We also compute the shear modulus, which is necessary to calculate the Maxwell time. We can calculate the shear modulus of any material using the Young's modulus, E, and Poisson's ration, υ, by using the following relation (Stacey and Davis, 2008; Appendix D)

$$\mu = \frac{E}{2(1+\upsilon)} \qquad \text{(A5)}$$

An order of magnitude variation in values of Young's modulus, E, for glacier ice exists in the literature (between 1-10 GPa) though a value of 5 GPa seems to be appropriate for ice shelves on tidal loading periods (Gudmundsson, 2011). We use a Poisson's ratio of ice, υ, of 0.37 (Ewing et al., 1934) to calculate a value of approximately 1.8 GPa for the shear modulus of ice, μ.

We calculate Maxwell times for a range of effective stresses and that data are shown of Figure A1. For Store Glacier, the driving stress (See the following Chapter) is on order ~200 kPa, which we use as our estimation of effective stress in Figure A1. The Maxwell time for that effective stress is about 0.3 hrs. Accordingly, loading applied to the ice at that effective stress is accommodated viscously. Therefore, the analysis of Store Glacier viscous flow response to tidal loading is appropriate in the following Chapter. At the WIP, the driving stress is on the order of ~1 kPa, corresponding to a Maxwell time of about 1.5×10^5 hrs or 6,250 days. Such a high Maxwell time suggests that the WIP behaves elastically at tidal loading periods. Based on our calculations of Maxwell times for each relevant effective stress, our treatment of ice flow response to tides as a viscous process is appropriate at Store Glacier and our treatment of ice flexure as an elastic process is appropriate at the WIP.

Appendix A References

Ewing, M., A. P. Crary, and A. M. Thorne (1934), Propagation of elastic waves in ice, Part 1, Physics, 5.

Glen, J. W., (1955) The creep of polycrystalline ice, Proc. R. Soc. Lond. A, 228: 519-538.

Gudmundsson, G. H. (2011), Ice-stream response to ocean tides and the form of the basal sliding law, The Cryosphere, 5: 259-270.

Paterson, W.S.B. (1994), The physics of glaciers, 3rd edition, Pergammon Press, 480 pp.

Stacey, F. D., and P. M. Davis (2008) Physics of the Earth, 4th edition, Cambridge University Press, 532 pp.

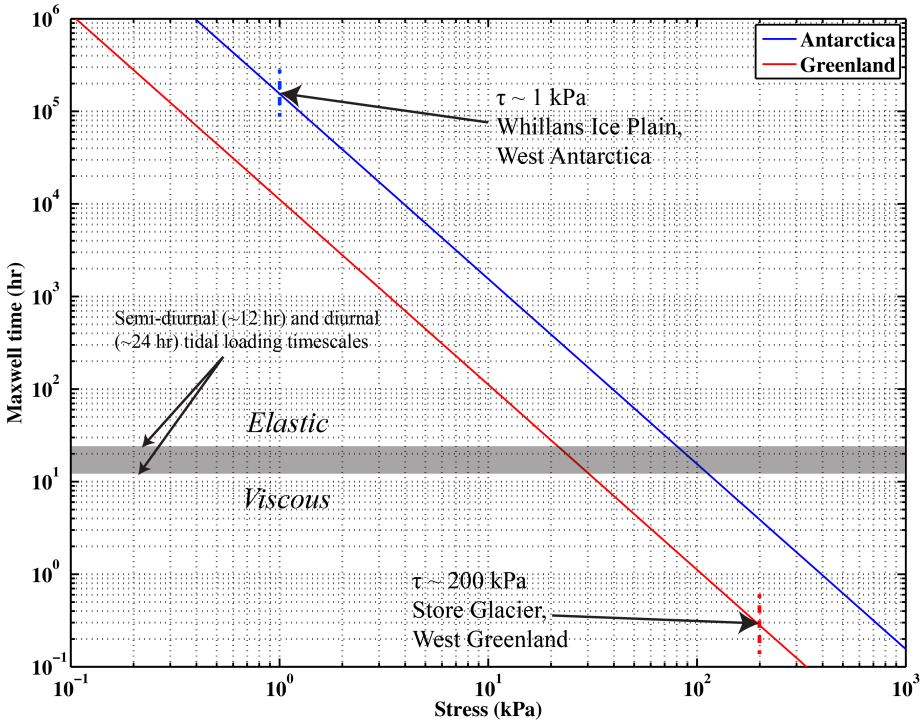

Figure A1: Maxwell time for a range of effective stresses. The grey bar indicates periods of tidal loading at semi-diurnal and diurnal periods. Maxwell times that less than the tidal loading periods indicate that the ice behaves viscously, whereas Maxwell times greater than the tidal loading periods indicate that the ice behaves elastically for tidal loading. Note the units of Maxwell time are in hours.

4. OCEANIC MECHANICAL FORCING OF THE DYNAMICS OF A MARINE-TERMINATING GREENLAND GLACIER BY ICE MELANGE REMOVAL AND OCEAN TIDES

The following Chapter, essentially unchanged, appeared previously in the Annals of Glaciology:

Walter, J. I., J. E. Box, S. Tulaczyk, E. E. Brodsky, I. M. Howat, Y. Ahn, and A. Brown (2012), Oceanic mechanical forcing of the dynamics of a marine-terminating Greenland glacier by ice melange removal and ocean tides, Annals of Glaciology, 53(60): 181-192.

4. OCEANIC MECHANICAL FORCING OF THE DYNAMICS OF A MARINE-TERMINATING GREENLAND GLACIER BY ICE MELANGE REMOVAL AND OCEAN TIDES

Abstract

Dynamics of marine-terminating major outlet glaciers are of high interest because of their potential for drawing down large areas of the Greenland ice sheet. We quantify short-term changes in ice flow speed and calving at a major west Greenland glacier and examine their relationship with the presence of the sea ice mélange and tidal stage. A field campaign at the terminus of Store Gletscher (70.40°N, 50.55°W) spanning the spring and summer of 2008 included: 4 broadband seismometers; 3 time-lapse cameras; a tide gauge; an automatic weather station; and an on-ice continuous GPS station. Sub-daily fluctuations in speed coincide with two modes of oceanic forcing: 1.) the removal of the ice mélange from the terminus-front and 2.) tidal fluctuations contributing to speed increases following ice mélange removal. Tidal fluctuations in ice flow speed were observed 16 km from the terminus and possibly extend further. Seismic records suggest bursts of calving activity that cluster near positive speed increases occurring after the mélange breaks up. A synchronous increase in speed at the front and clearing of the mélange, suggests that the mélange directly resists ice flow. We estimate a value of buttressing stress (~30-60 kPa) due to the presence of the ice mélange that is greater than the range of observed tides, though an order of magnitude less than the driving stress.

4.1. Introduction

Recent evidence suggests that the dynamics of Greenland glaciers are highly sensitive to external forcing. In response to the loss of its floating ice tongue, Greenland's largest outlet glacier, Jakobshavn Isbrae, doubled in speed, while retreating and thinning, and increasing its calving rate (Joughin and others, 2008). Helheim Glacier also experienced similar dynamic thinning and increases in speed along its main trunk, in response to retreat of the ice front (Howat and others, 2005). During the acceleration, the annual mass loss nearly doubled in 2004, but within a two-year period (2006) decreased to near-previous rates, likely due to stabilization of flow near the terminus (Howat and others, 2007). The results suggest that ice dynamics, manifested in flow speed, glacier thickness adjustments, and calving are closely linked, with the ability to vary rapidly. Furthermore, grounded ice on a glacier is likely sensitive to changes occurring at the terminus.

If ice dynamics can change rapidly in response to a warming climate, such changes may be directly related to ice/ocean interactions. Some of these changes may be driven by long-term oceanic warming present in the waters surrounding Greenland. One notable observation indicates an incursion of warm water around 1997 offshore of Jakobshavn Isbrae, which may have contributed to calving of its floating ice tongue and doubling in speed (Holland and others, 2008). Further evidence from within fjords in south-east Greenland suggests that wind-driven exchange at the continental shelf drives subtropical waters into fjords, creating a circulation which brings warmer waters into fjords and increases melting at the

terminus (Straneo and others, 2010). Local fjord-scale tidal pumping can be another important heat delivery mechanism to consider (Mortensen et al. 2011). A pervasive presence of warmer waters near the Greenland coast and throughout the Arctic may drive the observed reduction of sea ice extent in the Arctic in the last decade (Serreze and others, 2007).

The decreasing summer extent of sea ice on the Greenland margin also suggests decreased sea ice strength within fjords. At glaciated margins, land-fast sea ice traps calved icebergs near the fronts of the glaciers, creating a compacted mixture of sea and calf ice. The term ice mélange has been used to describe related ice conditions in various oceanographic settings (Rignot and MacAyeal, 1998; Amundson and others, 2010). This study focuses on a major outlet glacier in west-central Greenland, Store Gletscher, where the mélange thickness may vary by 100s of meters, depending on iceberg concentration. The mélange is further strengthened in the winter by freezing and formation of sea ice in interstitial gaps between icebergs, before eventual breakup in spring. In this area, the ice mélange reaches its peak extent in late April and then disappears rapidly in May (Howat and others, 2010). Plausibly, the ice mélange strengthens seasonally, as sea ice grows, and bonds ice fragments with sea ice in the fjord, complicating attempts to generalize its rheology.

In fjords, the presence of an ice mélange has oceanographic implications, such as preventing atmosphere-ocean heat and momentum exchange, which influences wind-driven mixing. It has become important to consider if ice mélange provides a significant mechanical link or stability to grounded glacier ice. Plausibly, the ice

mélange exerts some back-stress upon the glacier. Amundson and others (2010) infer that the ice mélange is responsible for the seasonal cessation of calving at Jakobshavn Isbrae. Other observations suggest that the disappearance of multi-year landfast sea ice can lead to rapid calving at Greenland glaciers (Reeh and others, 2001). If climatic trends continue towards decreasing sea ice concentrations and earlier breakup of sea ice at the Greenland margin, longer and less-obstructed calving seasons may persist and drive accelerated glacier flow and retreat.

To identify rapid changes in glacier behavior, we monitor changes in glacier flow speed using the Global Positioning System (GPS). The increasing use of high-rate, precise positioning has allowed the identification of tidal variations in velocity at ice streams (Bindschadler and others, 2003; Anandakrishnan and others, 2003; Gudmundsson, 2007) and Greenland outlet glaciers (de Juan and others, 2010). Typically, ocean tides impart relatively small stresses on the order of tens of kPa. Therefore, the sensitivity of glaciers to small stress fluctuations may provide unique insight into flow conditions and boundary conditions at the base.

These rapid changes in ice flow dynamics at the terminus are closely related to calving dynamics and therefore this study also includes observations on the relationship between loss of grounded ice to calving and the transient speed. The ever-changing terminus position is the balance between ice speed and calving rate (Meier and Post, 1987). The key difficulty in understanding calving requires coupling physical mechanisms operating at different timescales. Ice near the terminus cracks and cleaves away from termini abruptly, while the glacier may

change thickness or velocity, changing its terminus position on sub-daily to decadal timescales (e.g., Howat and others, 2010), sometimes synchronous with changes in calving. A better understanding of calving dynamics would allow its parameterization in ice sheet models and improve our understanding of future responses of marine ice sheets and glaciers to climate forcing.

In this study, we examine the influence of three glacier terminus processes on the sub-daily variations in the dynamics of Store Gletscher: 1.) the breakup of the ice mélange; 2.) fluctuating oceanic tides; and 3.) calving. We observe ice flow speeds near the terminus and 16 km up-glacier and compare the sub-daily oscillations with tidal stage and the presence/absence of the ice mélange. We develop a method of quantifying calving activity and compare it to the ice flow speed observations. The observations indicate that forcing at the terminus from these factors influence ice flow speeds further up-glacier, though quantifying the direct influence of any single mechanism in isolation proves limited.

4.2. Experiment Description and Measurement Techniques

A spring/summer 2008 field campaign was carried out at Store Gletscher, an outlet glacier that terminates in a ~70 km long fjord within the Uummannaq District on the central coast of west Greenland (Figure 1). Store Gletscher has displayed no multi-year change exceeding ~1.5 km in at least 40 years (Weidick, 1995 pg. C41). The front displays a relatively small ± 200 m seasonal oscillation in front position (Howat and others, 2010) likely due to growth and decay of a ~200 m section of

floating tongue. The advance typically occurs rapidly in April and May, reversing to a similarly brief period of rapid retreat once the mélange clears. Average melt season speeds remained stable between 2000 and 2009, with typically small (<10 %) variation during the melt season, with the exceptions of 2002 and 2005, when speed decreased 20-40% in mid-summer. The terminus of the glacier widens toward the front to 5.2 km and flows 11-15 m/d at the front (Ahn and Box, 2010). A dual-frequency GPS receiver recording at 1 Hz was located on the ice approximately 16 km upstream of the terminus. An automatic weather station was situated beside the on-ice GPS station. Air temperatures were recorded at heights between 1.5 and 2.0 m using a finewire thermocouple sensor that is insensitive to solar heating. On-ice wind speed measurements were made with an ultra-sonic anemometer situated 0.5 m above the temperature sensor. Four medium-period (response is linear with ground velocity for periods from ~ 0.03 – 30 s) seismometers were located near the terminus on bedrock. A tide gauge was installed beside an island 9 km southwest of the terminus. Air temperatures presented in this paper were collected from the on-ice station and were made at heights between 1.5 and 2.0 m using finewire thermocouples. The finewires are insensitive to solar heating. Time-lapse cameras, capturing images at 15 min intervals, were positioned on the north (1 camera) and south side (2 cameras) of the fjord, though only data from one of the south time-lapse is utilized quantitatively in this study (Figure 1). The other cameras provided the timing of changes in sea ice state. In order to obtain near-terminus speed estimates from the repeat photos, we implemented the Multi-Image/Multi-Chip matching procedure (Ahn and Howat,

2011) developed specifically for single-camera oblique photogrammetry of glaciers (Ahn and Box, 2010).

4.3. Observations

4.3.1 Ice mélange breakup

The time-lapse photos indicate the glacier the calving front stabilizing and the glacier growing in length throughout the winter months and into the spring season. This seasonal ice mélange rapidly disintegrates and clears within a few days in late May or early June in this region. Wind gusts above 25 m/s observed on Day 149 (May 28) triggered the Store Gletscher ice mélange breakup. The time-lapse photos indicate large bonded icebergs remobilize and floating away from the terminus.

After the mélange mobilizes, the fjord remains blanketed with an un-bonded mixture of smaller bergs and brash ice (Figure 2a). A small area of open water adjacent to the glacier front appears and persists at the southern terminus beginning on Day 160 (June 8). This polynya has is observed in past years (Weidick, 1995), and is a result of seasonal melt. The ice-front polynya continues to grow until around Day 169 (June 17) when nearly the entire front of the terminus is clear of ice, with plumes of brown, sediment rich water. While polynyas can also form at the front of Antarctic ice shelves due to cycling of warm oceanic waters beneath the shelf (Mankoff and others, this issue), the presence of brown, turbid water is indicative of melt water plume originating at the glacier bed.

4.3.2 Ice Speed Observations

We use the oblique photogrammetric method (Ahn and Box, 2010) to estimate flow speeds near the terminus. Average errors are on the order of 0.5 m/d, evident as the amplitude of noise within the speed solutions. Speeds measured at the terminus are illustrated in Figure 2c and 2e. Figure 2c indicates that near-terminus speeds include peaks at semi-diurnal and diurnal periods, though these solutions are noisy. In Figure 2d and 2e, we zoom in the period when the ice mélange breaks up and the period immediately following it. Examination of both speed records indicates changes closely following the ice mélange breakup around Day 149 (May 28). After the breakup, the near-terminus ice undergoes an increase in speed of 14% (1.5 m/d) over ~2 days (Figure 2e).

The GPS data were post-processed in kinematic mode using the GAMIT/TRACK software package, to obtain differential positions relative to a bedrock station we deployed temporarily. In order to obtain reliable velocity estimates from the 1 Hz position data, we smooth each position (Cartesian earth-centered, earth-fixed coordinates - x, y, and z) using a 1-hour running mean and remove all points greater than 1 σ from the running mean. Such a cutoff is necessary for high-sample rate data. The data is then down-sampled to 5-minute medians, in order to increase computational efficiency, and a 1st degree loess filter is applied with a 6 h window. Figure 2b illustrates the first time derivative and the resultant along-flow horizontal speed.

The GPS record shows little variability until Day 148 (May 27), with the exception of several, discrete speedup events lasting several hours. A dense ice mélange filled the fjord and air temperatures were below freezing for most of this period, and supra-glacial melt water accumulation was not visible on the ice surface. Between Days 148 and 152 (May 27 and May 31), the speed decreased ~15% as the mélange cleared, exposing patches of open water. This clearing coincided with a sustained high-wind (30 min averages of 10 m/s with 24 m/s gusts observed at the on-ice AWS situated beside the GPS site) event lasting all of Day 148 (May 27), when we observed large, tabular icebergs moving away from the front. During this period, speeds near the terminus increased ~1.5 m/d, plausibly in response to loss of buttressing.

Following the ice mélange breakup, the ice speed 16 km upstream from the terminus begins to undergo large diurnal and smaller semi-diurnal fluctuations. In order to evaluate the periodicity on the GPS record, we first perform a Fast Fourier Transform (FFT) on the entire length of the flow speed record, which clearly identifies peaks at ~12 hours and ~24 hours (Figure 3c). A spectrogram of the GPS flow speed record highlights the timing of the presence of semi-diurnal and diurnal oscillations. A 6-day moving window evaluated at 1-hour increments produces the time series illustrated in Figure 3a. Warm colors (red) in Figure 3a indicate greater signal power at those periods. After the ice mélange breaks up, dominant signals in the GPS data appear at both semi-diurnal (~12 hours) and diurnal (~24 hours) periods. The semi-diurnal signal continues until Day 156 (June 5) when it returns to

background noise levels, then reappears again from Days 159 – 170 (June 7 – June 18) through to the end of the record. The diurnal signal is strongest during the periods from Days 150 – 159 (May 29 – June 7) and Days 164 – 170 (June 12 – June 18). For the near-terminus estimate of speed, positive speed fluctuations occur at similar periods (Figure 2b, 4 hr image pair data), though amplitudes of the speed increases in Figure 2e are artificial due to errors on the order of 0.5 m/d.

Large amplitude ice flow speed fluctuations observed at the GPS station, during the period from Days 152 – 160 (May 31 – June 8), occur at low tides (Figure 4a/4b). However, as illustrated in Figure 4c, the speed peaks also coincide with maximum daily air temperature. During this time period, air temperatures over the ice were between 0 – 5 °C during sunlit periods, with nights below freezing temperatures. Thus, melt water production would have ceased each night, likely contributing to the strong diurnal periodicity of the speed increases. In a simple model of glacier response to climate, high air temperature enhances surface melting, increases melt water that pressurizes the basal interface, and likely drives accelerated ice flow. In considering the effect of air temperature influencing ice dynamics, it should be noted that the air temperature likely increases toward sea level. Therefore, our on-ice measurement point may be considered a minimum air temperature, compared to the air temperatures occurring downglacier towards the terminus. While speed response to peak air temperatures or maximum solar insolation may lag air temperature maxima by 7-8 hours (Walters and Dunlap, 1987), we find nearly zero time lag for ice speed (Figure 4). Such a small lag might be expected for temperature-

driven speed increases because the GPS station is located immediately adjacent to a large supraglacial lake (the dark feature a few km north-west of the GPS station in Figure 1). The air temperature exhibit diurnal peaks in its spectra and not the semi-diurnal peaks observed in the GPS, time-lapse camera, and tide gauge data.

The clear diurnal variation in speed and coherence with the air temperature record suggests the development of a hydrologic connection between the surface and the bed. A diurnal oscillation of similar amplitude was also observed on Columbia Glacier (Meier and others, 1994; Kamb and others, 1994). This variation in motion, in-phase with air temperature, is consistent with observations of alpine glaciers, where a lag is attributed to thermal inertia of the surface and the time needed for water to flow from the source area to the glacier water table (Mair and others, 2002). During the period of strong diurnal periodicity (Days 152 – 160 or May 31 – June 8), no melt water plume is visible at the ocean surface near the front, suggesting that drainage was relatively inefficient. The diurnal variation in melt water penetration to the bed would then induce a cyclical perturbation to the basal water storage that would cause sliding (Kamb and others, 1994). The peak daily amplitude in speed decreased after peaking on Day 153 (June 1), disappearing after Day 159 (June 7), despite the fact that air temperatures remained above freezing. This indicates a progressively decreasing influence of diurnal variations in surface melt water input to the bed on local basal water pressure and sliding. This decrease could be due to increasing efficiency of the basal drainage system. Such a mechanism would result

from the formation of a tunnelized drainage system, in which sliding becomes decoupled from basal water discharge (Röthlisberger, 1972).

Due to the timing of our observations, it is impossible to explicitly isolate and identify periodic forcing contributors (low tide and high air temperature) that oscillate at nearly the same period and whose phase is nearly coherent. However, the presence of semi-diurnal periodicity in the speed record and not in the air temperature data suggests that ocean tides influence the glacier flow dynamics. In addition to the periodic tidal and melt water forcing of ice flow speed described above, in the following we consider the correlation between calving and flow speed increases.

4.3.3 Seismic identification of calving

Various studies identify calving and glacier-related processes occurring across a broad spectrum of frequency. At Columbia Glacier, Alaska, O'Neel and others (2007) find peak iceberg calving energy, within 1-3 Hz, shifting to ~10 Hz after retreating into a deeper area (Walter and others, 2010). Seismicity observed for glaciers over a range of ice-thermal conditions (temperate, polar, etc.) may generate seismic radiation over a range of observable frequencies, including ~200 Hz (Anandakrishnan and Bentley, 1993), 6 – 35 Hz (West and others, 2010), and 30 – 60 seconds (Ekstrom and others, 2003; Wiens and others, 2008; Walter and others, 2011). The large range of observations may be due to differences in equipment quality and distance from the source, though more likely due to the characterization of a variety of phenomena and by extension, a variety of source mechanics. For

example, Greenland glacial earthquakes have been described as occurring nearly synchronous with large calving events (Tsai and others, 2008), while similar events occur as basal sliding events on Whillans Ice Stream, West Antarctica (Bindschadler and others, 2003; Wiens and others, 2008; Walter and others, 2011).

We develop a method of identifying bursts of calving activity within our seismic record, by first focusing on the nature of seismicity from a single calving event. The 15-minute photos indicate a number of large, isolated calving events (example in Figure 5a). Figure 5b illustrates the seismic record during the time period spanning the two images for the east component of the southern seismic station, co-located with the camera. We compute the velocity spectra of two 100 s portions of the seismic record (Figure 5c). The spectra for the signal is generally fairly broadband with a possible peak around ~1 Hz. Given the observation that the seismic signal is significantly greater amplitude over a broad range of frequencies extending from ~0.3 Hz to the Nyquist frequency, we use the signal in this range to distinguish potential calving events. Computing the velocity spectra in 80 s windows with 50% overlap for all the stations in the network and stacking them produces the spectrogram illustrated in Figure 6a.

After identifying the largest calving events from the time-lapse photos, we find that the calving events occur synchronous with the concentrations of energy clearly visible as vertical bands in Figure 6a. The largest calving events in the time-lapse photos occur within one or two frames, which constrains their duration to be 15-30 min. This is in contrast with the duration of calving activity in the seismic record,

which can be on the order of hours. The difference in durations is possibly due to small fracture events (on the order of meters), which are recorded seismically, but not visible due to obstructions or below the resolution of the camera. In order to avoid noise clearly visible in Figure 6a just below 5 Hz, we sum the cumulative energy within the 7-20 Hz band, take the logarithm, and smooth over a 1000-point running average (Figure 6b). The peaks in the time series indicate discontinuous periods of intense calving activity.

The timing of the ice mélange breakup is clearly visible near the beginning of the calving activity record (Figure 7a) and abruptly ceases around Day 150 (May 29), coinciding with the clearing of the ice mélange. Especially around Day 154 (June 2) and continuing through Day 160 (June 8), some larger peaks in calving appear to be coherent with peaks in speed. With a moving 2-day sample interval, we find positive correlations during the period from Days 150 – 165 (May 29 – June 13) (Figure 7c) that indicate coherence between calving activity and ice speed increases, which are more common after the ice mélange breakup. Close examination of the calving record indicates that during Days 154 – 156, near-terminus ice flow speeds lead calving activity by several hours. Due to the limited period of observations we are hesitant to conclude causation, yet this timing suggests that speed increases near the terminus can cause calving. Such a hypothesis could be the subject of future study.

4.4. Discussion

We have thus far presented evidence of external forcing of glacier dynamics by two oceanic mechanisms at the ice front, ocean tides and the absence/presence of the ice mélange, and one internal glacial mechanism, calving. Melt water production also likely perturbs ice flow speed, clearly manifested by strong diurnal speed increases following the ice mélange breakup (Figure 4). We reiterate that due to the nearly coherent phase of our observations, we cannot explicitly evaluate the contribution that each forcing has upon the flow speed. What follows are order of magnitude estimations of the expected flow speed increase in response to tides and the buttressing stress that restrains glacier flow when the mélange is present. We observe semi-diurnal periodicity in the ice flow speed at the GPS station, which is indicative of tidal forcing. In Section 4.1 we will use longitudinal coupling theory (Kamb and Echelmeyer, 1986) to evaluate the expected amplitude of ice flow speed changes from a 2 m change in tide height. In Section 4.2, we quantify the ability of the ice mélange to resist ice flow, by calculating the buttressing stress. This calculation relies upon the observation of a "ramped" step-change in ice flow speed observed near the terminus, coincident with the removal of the ice mélange. Finally, in Section 4.3, we give further context to the observational link between ice flow speed and calving.

4.4.1 Longitudinal coupling of ice flow by ocean tidal forcing

We begin our consideration of the oceanic mechanical perturbation of ice flow by predicting the glacier ice speed change in response to tides. A seminal paper by

Kamb and Echelmeyer (1986) introduces a rigorous analysis of longitudinal coupling of flow within a glacier. In addition to the typical force balance of a glacier, which can include the driving stress, lateral shear stress (wall stress), and basal shear stress terms, the longitudinal stress determines how the glacier responds to actions such as stretching. Walters (1989) extended the longitudinal coupling theory to predict the flow response to a hydrostatic stress change due to tides at the terminus of Columbia Glacier. In the Appendix, we summarize some of the steps taken in Walters (1989) to arrive at a solution for the flow speed increase from a tide change:

$$u_1(x) = \frac{p_T L}{\overline{\eta}} \exp\left(-\left|x - x_0\right| / L\right) \qquad (1)$$

In Equation 1, u_1 is the perturbation velocity, p_T is the pressure variation due to the 2 m tide level change (~20 kPa), η is the average effective viscosity, x is distance along-flow, and L is the longitudinal coupling length-scale. For Equation 1, we use the range of average effective viscosities from 0.5 – 2.0 bar a (1.58×10^{13} – 6.31×10^{13} Pa s), as found in Kamb and Echelmeyer (1986). We determine the coupling length, L, via Equation A7. Other assumed values used for solving Equation 1 are shown in Table 1 or the Appendix.

In addition to showing the predicted speed perturbations by tidal forcing in Figure 8, we also calculate the range in amplitudes of speed perturbations ~16 km up-glacier during the period May 29 – June 8 (Days 150 – 160). As illustrated in Figure 8, the predicted values for a 2 m tide lie within the range of observed speed perturbations for the m=3 stress exponent. However, the maximum observed speed

perturbations are nearly double the predicted speed perturbations from tidal forcing alone. Therefore, we hypothesize that the presence of melt water also contributes significantly to the observed speed perturbations especially during the period Days 150 – 160 (May 29 – June 8). The amplitudes of the diurnal speed perturbations appear to decay during this period and later become less diurnally periodic, as the melt season continues. Coincidentally, the reduction in coherence between air temperature and diurnal speed perturbations (Figure 4) coincides with the appearance of the polynya at the ice front on Day 160 (June 8). Therefore, one plausible explanation is that when efficient drainage pathways develop, they lose their ability to pressurize the glacier bed.

Recent modeling results suggests that ice flow coupling can extend as much as 15-20 km longitudinally inland from speed increases at the Greenland ice margin (Price and others, 2008). We calculate coupling lengths, L, for various stress exponents and a range of potential effective viscosities of ice (Table 2). With a stress exponent of m=3, we calculate a longitudinal coupling length, L, of 10-20 km over the range of viscosities used (Table 2). This is a factor of 17-33 (L/H_i) times the presumed thickness of the glacier near the terminus, H_i (600 m). Kamb and Echelmeyer (1986) suggest that glaciers in surge, such as surging behavior exhibited at Variegated Glacier, may reach values of L/H_i of ~12. Such a discrepancy may be reconciled by the fact that the Kamb and Echelmeyer (1986) longitudinal coupling analysis does not account for basal sliding, which is plausibly a large component of the observed positive speed peaks.

4.4.2 Ice mélange buttressing stress from near-terminus ice flow speed increase

In this section, we use Equation 1 to quantitatively estimate the strength of the ice mélange. The mélange strength likely continually evolves over winter and also may be dependent upon the amount of calved icebergs and their thicknesses within the fjord. However, the coincidence of the increase in speed observed at the front and clearing of the mélange (Figure 2), without substantial retreat of the ice front suggests that mélange directly resists ice flow.

Equation 1, at the limit of x=0, reduces to an expression relating a velocity perturbation to a change in stress at the terminus front. If we rearrange this equation and assume that the pressure is derived from the presence/absence of the ice mélange, we have:

$$p_{melange} = \frac{u_1(x_0)\overline{\eta}}{L} \qquad (2)$$

where the pressure due to the presence of the ice mélange, $p_{mélange}$, is proportional to the velocity perturbation observed at the terminus, $u_1(x_0)$, multiplied by the average effective viscosity, η, divided by the longitudinal coupling length, L. The along-flow length-scale, L, is necessary because we are evaluating the longitudinal ice flow response to the removal of the ice mélange buttressing effect at the terminus. The ice mélange pressure, $p_{mélange}$, is conceptually equivalent to a glacier buttressing or back-stress exerted by the mélange. In evaluating the ice mélange buttressing stress, we use the observed ~1.5 m/d increase in near-terminus ice speed as the value for $u_1(x_0)$,

as seen in Figure 2c (from photogrammetry dataset). We use the same range of effective viscosities as discussed in the previous section. With the stress exponent m=3, we calculate buttressing stresses in the range of 28-56 kPa. Thus, for a range of effective viscosities, we conclude that the winter sea ice mélange provides an effective back-stress, $p_{melange}$, upon the glacier of ~30-60 kPa. The ice mélange buttressing stress is not much larger than that induced by the range of tides observed at the terminus (20 kPa).

One way to quantify the relative significance of the mélange buttressing stress is to compare the value to Store Gletscher's driving stress. Driving stress is equal to $\rho g H_i \sin\alpha$, where α is the estimated surface slope and the other variables are the same as before. From the examination of satellite imagery, we estimate a change in slope of approximately ~400 m over ~10 km, or about 0.04. From these values, we calculate a driving stress of ~200 kPa. Our range of calculated mélange buttressing stress (~30-60 kPa) is an order of magnitude less than the driving stress. The ice mélange buttressing stress can be considered an additional seasonal resisting force and may be similar in magnitude to the basal drag resistance. We are also reasonably confident that these are realistic values for the seasonal buttressing back-stress given results of a few recent studies. First, when modeling the influence of the seasonal ice mélange on calving, Nick and others (2010) used a value of 20 kPa for the back-stress imposed by the mélange. Also, Van der Veen and others (2011) directly applied a force balance scheme to estimate a change of 150 kPa in back-stress, due to the loss of the floating ice tongue at Jakobshavn Isbrae from 1995-2005.

4.4.3 Calving and ice speed

The ice mélange disintegration and associated calving are present in the record starting Day 145 (May 24) and ceasing by Day 150 (May 29). A short period of relative quiescence is observed until around Day 154 (June 2) when calving continues periodically through the observation period. From Day 154 – 160 (June 2 – 8) peaks in calving are better correlated with peaks in flow speed (Figure 7c). Near-terminus ice flow speed increases appear to lead calving activity by several hours during Days 154 – 156, though accurately identifying timing is significantly hindered by smoothing of the calving activity time series and a noisy photogrammetry dataset. We merely point out that the calving and ice speed increases are clustered in time, an observation made at other Greenland outlet glaciers (Nettles and others, 2008).

A correlation between calving and ice flow speed may be expected, as glacier velocity probably has important controls on calving. For ice shelves, Alley and others (2008) show calving rate linearly correlates with a normalized stretching rate. Another model for calving productivity involves crevasse-depth criteria (Benn and others, 2007), where the calving margin is defined as the point where the crevasse depth equals the glacier freeboard. Therefore, if longitudinal stretching occurs under positive speed increases, then crevasse depth increases, promoting calving. Though a feedback between the two is expected, the identification of a causal link between calving and ice flow speed, requires denser along-flow speed observations and a calving activity time series whose amplitude correlates with calved ice volume.

4.5. Summary and Conclusions

We examined a number of short-term (sub-daily) variations in the flow dynamics of a major west Greenland ice sheet tidewater outlet glacier. We obtained data from seismometers, GPS, time-lapse cameras, and an on-ice automatic meteorological station. We observe two modes of oceanic forcing upon the glacier horizontal speed, the presence/absence of ice mélange and ocean tides. Acceleration near the terminus of ~1.5 m/d (or 14%) over a 2 day period occurs after the winter sea ice mélange disintegrates and drifts away. Based on this "ramped" step-change in speed, we determine that when the mélange is present, it provides a ~30-60 kPa back-stress upon the glacier terminus, in the direction opposite ice flow. After the mélange breaks up, we observe a synchronicity between flow speed, minimum ocean tidal range, and surface air temperature.

We find that GPS ice flow speed times series includes both semi-diurnal and diurnal peaks; semi-diurnal peaks can only be caused by tides and is evidence that tides can influence flow at least ~16 km from the terminus. Further, we find that predicted speed increases match our observations of speed increases during this period, though only near the minimum range of GPS fluctuations. The discrepancy between observed and predicted speed perturbations, via the tidal range input to the longitudinal stress balance, suggests that melting likely contributes to the observed accelerated flow. The glacier likely undergoes a rapid flow response to melt lubrication via basal pressurization that exists for ~10 days. The drainage efficiency

seems to increase to the point that basal pressurization is abruptly lost, followed by no correlation between horizontal speed and surface melting. The flow regime instead becomes characterized by a sustained correlation with semi-diurnal forcing from the tidal stage. Thus, we find evidence of an evolution in the relative importance of melt and tidal forcing, with further investigations planned for future field seasons.

Lastly, we show that calving and ice flow speed observed ~16 km upstream from the terminus appear to be manifested in nearly synchronous perturbations after the mélange has been removed. The buttressing effect of the mélange plausibly reduces longitudinal stretching and its removal signals a period of increased susceptibility to calving.

4.6. Acknowledgments

We thank Jason Amundson and an anonymous reviewer for thorough and insightful reviews, which greatly improved this manuscript. Francis Nimmo and Eric Rignot are also thanked for enlightening discussions regarding the strength of ice mélange. JIW is funded by a NASA Graduate Earth and Space Science Fellowship. A University of California IGPP Mini-Grant to JIW, a Special Research Grant from the UCSC Committee on Research to ST, and a supplement to NASA grant NNX08AD31G-05 to ST provided partial support for field logistics. Funding for the GPS, time-lapse camera equipment, and partial field logistics were made possible by an OSU Climate Water Carbon Initiative grant managed by Doug Alsdorf. Field logistics were also partially supported by NASA and NSF. We thank Dan Sampson

for technical assistance prior to fieldwork and Tristan Rhodes for assisting in preparing equipment.

4.7. Appendix A. Longitudinal coupling of ice flow modulated by tidal stresses

In order to better understand external forcing at the terminus and its effect upon the glacier, we must first sum all of the relevant stresses in the contributing to glacier flow. We follow the convention common in glaciology where stresses are geometrically corrected so that they are contact-area-normalized. We assume that the sum of the driving stress, τ_d, minus the longitudinal stress, τ_L, and basal shear stress (basal drag), τ_b, balances. Thus,

$$\tau_d - \tau_L - \tau_b = 0 \qquad \text{(A1)}$$

In order to evaluate the ice flow speed response to tides and compare with our observations of semi-diurnal and diurnal speed oscillations, we choose a relationship of velocity to basal shear stress and effective pressure. We employ a commonly used power-law sliding relation after Bindschadler (1983),

$$u = k \frac{\tau_b{}^m}{p_e} \qquad \text{(A2)}$$

where u is horizontal velocity, k is an empirical constant, m is a locally determined exponent, either 1 or 3, best-fit with a value of 3 for most glaciers (Bindschadler, 1983). Effective pressure, p_e, in Equation A2 is the ice overburden minus water pressure at the terminus and is positive for grounded ice. We assume, informed by the camera observations, that the glacier is grounded at the bed once the winter

breakup has occurred. In this case, the effective pressure is thus always greater than zero, and is given by

$$p_e = g\left(\rho_i H_i - \rho_w h_w\right) \qquad \text{(A3)}$$

In Equation A3, g is the acceleration due to gravity (9.81 m/s^2), ρ_i is the density of ice (917 kg/m^3), H_i is the thickness of the glacier ice at the terminus, estimated to be ~600 m, ρ_w is the density of seawater (1,025 kg/m^3), and h_w is the depth of the fjord at the terminus.

At this point, we follow the derivation of Walters (1989), which is an application and extension of the derivation for longitudinal coupling found in Kamb and Echelmeyer (1986). For brevity, we do not repeat all the steps involved in this derivation, but point the reader to these papers. In introducing the derivation, we define our reference frame, where ice flows in the x-direction. The force balance from Equation A1 becomes

$$\rho_i g H_i \alpha - 4\frac{d}{dx}\left(H_i \bar{\eta}\frac{d\bar{u}}{dx}\right) - \left(\frac{up_e}{k}\right)^{1/m} = 0 \qquad \text{(A4)}$$

The first term on the left hand side (LHS) is the gravitational driving stress of the glacier, where ρ is the density of ice, H_i is the glacier thickness, and g is the acceleration due to gravity. The second term on the LHS of the equation describes the longitudinal stress component of the force balance equation. As most of the motion is dominated by sliding, ice rheology is further simplified, by assuming that a depth-averaged viscosity or effective viscosity, η, is sufficient. In addition, we

average over along-flow length-scales. The average viscosity term is valid assuming du/dx does not significantly change along-flow, which is expected as long as there are no large variations in slope or thickness. Satellite imagery does indicate an undulating topographic variation in slope, likely also manifested as undulations in the basal topography. Significant variations of basal topography pose several complications in applying the assumptions for Equation A4 (Kamb and Echelmeyer, 1986) and as a result, our later predictions may be poor.

In order to further simplify Equation A4, Walters (1989) uses perturbation analysis, where velocity, u, and effective pressure, p_e, are expanded in terms of a mean plus a small perturbation. Expanding Equation A4 and collecting terms on the order of only the small perturbations, results in the following equation.

$$-4\frac{d}{dx}\left(H_i\overline{\eta}\frac{du_1}{dx}\right)+\frac{\tau_0}{m}\left(\frac{u_1}{\overline{u}}-\frac{p_1}{p_0}\right)=0. \qquad \text{(A5)}$$

In Equation A5, x is distance along-flow, u_1 is the perturbation velocity, u is the average flow speed, η is the average effective viscosity, p_1 is the perturbation effective pressure, p_0 is the average effective pressure, and τ_0 is the average basal shear stress. If we assume that H_i and η are relatively constant along-flow and $\tau_0 = \left(\overline{u}p_0/k\right)^{1/m}$, then Equation A5 reduces to

$$-L^2\frac{d^2u_1}{dx^2}+u_1=\overline{u}\frac{p_1}{p_0} \qquad \text{(A6)}$$

The longitudinal coupling length, L, is derived in Kamb and Echelmeyer (1986) and is shown below, where m is the stress exponent, H_i is the thickness of ~600 m, τ_0 is

the average basal shear stress (150 kPa from Walters, 1989), and u is the average flow speed near the terminus or 11 m/d (Howat and others, 2010):

$$L = \sqrt{\frac{4mH_i\overline{\eta}\,\overline{u}}{\tau_0}} \qquad \text{(A7)}$$

If basal water pressure fluctuations are neglected ($p_1 = 0$), a solution to Equation A6 can be found that is an exponential function, which predicts the decay of near-terminus velocity perturbations as they propagate up-glacier.

$$u_1(x) = \frac{p_T L}{\overline{\eta}} \exp\left(-\left|x - x_0\right| / L\right) \qquad \text{(A8)}$$

Equation A8 predicts horizontal speed perturbations as a function of distance from the terminus, where, u_1 is the perturbation velocity and p_T is the pressure variation due to the 2 m tide level change (~20 kPa).

References:

Ahn, Y. and J. E. Box. 2010. Glacier velocities from time-lapse photos: technique development and first results from the Extreme Ice Survey (EIS) in Greenland, J. Glaciol., 56(198), 723-734.

Ahn, Y. and I.M. Howat. 2011. Efficient, Automated Glacier Surface Velocity Measurement from Repeat Images Using Multi-Image/Multi-Chip (MIMC) and Null Exclusion Feature Tracking, IEEE Trans. on Geoscience and Remote Sensing, 49(8), 2838-2846.

Alley, R. B. and others. 2008. A simple law for ice-shelf calving, Science, 322, 1344.

Amundson, J. M., M. Fahnestock, M. Truffer, J. Brown, M. P. Luthi, and R. J. Motyka. 2010. Ice mélange dynamics and implications for terminus stability, Jakobshavn Isbræ, Greenland, J. Geophys. Res., 115, F01005, doi:10.1029/2009JF001405.

Anandakrishnan, S. and C. R. Bentley. 1993. Micro-earthquakes beneath Ice Streams B and C, West Antarctica: observations and implications, J. Glaciol., 39(133), 455-462.

Anandakrishnan, S., D. E. Voigt, R. B. Alley, and M. A. King. 2003. Ice stream D flow speed is strongly modulated by the tide beneath the Ross Ice Shelf, Geophys. Res. Lett., 30(7), 1361, doi:10.1029/2002GL016329.

Benn, D. I., C. R. Warren, and R. H. Mottram. 2007. Calving processes and the dynamics of calving glaciers, Earth Sciences Reviews, 82, 143 – 179.

Bindschadler, R. 1983. The importance of pressurized subglacial water in separation and sliding at the glacier bed, J. Glaciol., 29(101), 3–19.

Bindschadler, R. A., M. A. King, R. B. Alley, S. Anandakrishnan, and L. Padman. 2003. Tidally controlled stick-slip discharge of a West Antarctic ice stream, Science, 301, 1087–1089, doi:10.1126/science. 1087231.

de Juan, J., et al. 2010. Sudden increase in tidal response linked to calving and acceleration at a large Greenland outlet glacier, Geophys. Res. Lett., 37, L12501, doi:10.1029/2010GL043289.

Ekstrom, G., M. Nettles, and G. A. Abers. 2003. Glacial earthquakes, Science, 302, 622–624.

Gudmundsson, G. H. 2007. Tides and the flow of Rutford Ice Stream, West Antarctica, J. Geophys. Res., 112, F04007, doi:10.1029/2006JF000731.

Holland, D. M. R. H. Thomas, B. d. Young, M. H. Ribergaard, and B. Lyberth. 2008. Acceleration of Jakobshavn Isbrae triggered by warm subsurface ocean waters, Nature Geoscience, 1, 659-664.

Howat, I. M., I. Joughin, S. Tulaczyk, and S. Gogineni. 2005. Rapid retreat and acceleration of Helheim Glacier, east Greenland, Geophys. Res. Lett., 32, L22502, doi:10.1029/2005GL024737.

Howat, I. M., I. Joughin, and T. A. Scambos. 2007. Rapid changes in ice discharge from Greenland outlet glaciers, Science, 315, 1559, doi:10.1126/science.1138478.

Howat I. M., J. E. Box, Y. Ahn, A. Herrington, and E. M. McFadden. 2010. Seasonal variability in the dynamics of marine-terminating outlet glaciers in Greenland, J. Glaciol., 56(198), 1-13.

Joughin, I., I. M. Howat, M. Fahnestock, B. Smith, W. Krabill, R. B. Alley, H. Stern, and M. Truffer. 2008. Continued evolution of Jakobshavn Isbrae following its rapid speedup, J. Geophys. Res., 113, F04006, doi:10.1029/2008JF001023.

Kamb, B., and K. A. Echelmeyer. 1986. Stress-gradient coupling in glacier flow: I. Longitudinal averaging of the influence of ice thickness and surface slope, J. Glaciol., 32(111), 267–284.

Kamb, B., H. Engelhardt, M. A. Fahnestock, N. Humphrey, M. Meier and D. Stone. 1994. Mechanical and hydrologic basis for the rapid motion of a large tidewater glacier. 2. Interpretation. J. Geophys. Res., 99(B8), 15,231-15,24 4

Mair, D., P. Nienow, M. Sharp, T. Wohlleben, and I. Willis. 2002. Influence of subglacial drainage system evolution on glacier surface motion: Haut Glacier d'Arolla, Switzerland, J. Geophys. Res., 107(B8), 2175, doi:10.1029/2001JB000514.

Mankoff, K. D., S. S. Jacobs, S. Tulaczyk, S. E. Stammerjohn. In review. Ice and ocean properties near the terminus of Pine Island Glacier Ice Shelf, Antarctica, Annals of Glaciology, this issue.

Meier, M. F., and A. Post. 1987. Fast tidewater glaciers, J. Geophys. Res., 92, 9051–9058.

Meier, M. and 9 others. 1994. Mechanical and hydrologic basis for the rapid motion of a large tidewater glacier. 1. Observations. J. Geophys. Res., 99(B8), 15,219-15,229.

Mortensen, J., K. Lennert, J. Bendtsen, and S. Rysgaard. 2011. Heat sources for glacial melt in a sub-Arctic fjord (Godthåbsfjord) in contact with the Greenland Ice Sheet, J. Geophys. Res., 116, C01013, doi:10.1029/2010JC006528.

Nettles, M., et al. 2008. Step-wise changes in glacier flow speed coincide with calving and glacial earthquakes at Helheim Glacier, Greenland, Geophys. Res. Lett., 35, L24503, doi:10.1029/2008GL036127.

Nick, F. M., C. J. Van der Veen, A. Vieli, and D. I. Benn. 2010. A physically based calving model applied to marine outlet glaciers and implications for the glacier dynamics, J. Glaciol., 56, 781–794, doi:10.3189/002214310794457344.

O'Neel, S., H. P. Marshall, D. E. McNamara, and W. T. Pfeffer. 2007. Seismic detection and analysis of icequakes at Columbia Glacier, Alaska, J. Geophys. Res., 112, F03S23, doi:10.1029/2006JF000595.

Price, S. F., A. J. Payne, G. A. Catania, and T. A. Neumann. 2008. Seasonal

acceleration of inland ice via longitudinal coupling to marginal ice, J. Glaciol., 54(185), 213-219.

Reeh, N., H. H. Thomsen, A. K. Higgins, and A. Weidick. 2001. Sea ice and the stability of north and northeast Greenland floating glaciers, Annals of Glaciology, 33, 474 – 480.

Rignot, E., and D. R. MacAyeal. 1998. Ice-shelf dynamics near the front of the Filchner-Ronne Ice Shelf, Antarctica, revealed by SAR interferometry, J. Glaciol., 44, 405–418.

Rothlisberger, H. 1972. Water pressure in intra- and subglacial channels. Journal of Glaciology, Vol. 11, No. 62, 177-203.

Serreze, M. C., M. M. Holland, and J. Stroeve. 2007. Perspectives on the Arctic's shrinking sea-ice cover, Science, 315, 1533-1536.

Straneo, F. and others. 2010. Rapid circulation of warm subtropical waters in a major glacial fjord in East Greenland, Nature Geoscience, 3, 182 – 186.

Tsai, V. C., J. R. Rice, and M. Fahnestock. 2008. Possible mechanisms for glacial earthquakes, Journal of Geophysical Research, 113(F03014).

Van der Veen, C., and others. 2011. Controls on the recent speed up of Jakobshavn Isbrae, West Greenland, J. Glaciol., 57, 770–782.

Walter, F., S. O'Neel, D. McNamara, W. T. Pfeffer, J. N. Bassis, and H. A. Fricker. 2010. Iceberg calving during transition from grounded to floating ice: Columbia Glacier, Alaska, Geophys. Res. Lett., 37, L15501, doi:10.1029/2010GL043201.

Walter, J. I., E. E. Brodsky, S. Tulaczyk, S. Y. Schwartz, and R. Pettersson. 2011. Transient slip events from near-field seismic and geodetic data on a glacier fault, Whillans Ice Plain, West Antarctica, J. Geophys. Res., 116, F01021, doi:10.1029/2010JF001754.

Walters, R. A., and W. W. Dunlap. 1987. Analysis of time series of glacier speed: Columbia Glacier, Alaska, J. Geophys. Res., 92(B9), 8969 – 8975.

Walters, R. A. 1989. Small amplitude, short period variations in the speed of a tidewater glacier in south-central Alaska, Ann. Glaciol., 12, 187– 191.

West, M. E., C. F. Larsen, M. Truffer, S. O'Neel, and L. LeBlanc. 2010. Glacier microseismicity, Geology, 38(4), 319–322, doi:10.1130/G30606.1.

Wiens, D. A., S. Anandakrishnan, J. P. Winberry, and M. A. King. 2008. Simultaneous teleseismic and geodetic observations of the stick-slip motion of an Antarctic ice stream, Nature, 453, 770–774, doi:10.1038/ nature06990.

Weidick, A. 1995. Greenland. In Williams, R.S. and J. Ferrigno, eds. Satellite image atlas of glaciers of the world. Denver, CO, US Geological Survey, C1–C105. (USGS Professional Paper 1386-C.

Variable	Value	Units
g, gravitational acceleration	9.81	m/s^2
ρ_i, density of glacier ice	917	kg/m^3
ρ_w, density of seawater	1,025	kg/m^3
H_i, glacier thickness	~600	m
m, stress exponent	3	none (Bindschadler, 1983)
τ_0, average basal shear stress	150	kPa (Walters, 1989)
u, average horizontal speed	11	m/d (Howat and others, 2010)
p_T, pressure from 2 m tide	20	kPa

Table 1: Table of assumed values for use in Equations 1 (A8) and A7.

Stress exponent, m	Viscosity, η (Pa s)	Coupling length, L (km)	Velocity perturbation at x=0, $u_1(x_0)$ (m/d)
1	$1.58x10^{13}$ (0.5 bar a)	5.67	0.31
1	$3.15x10^{13}$ (1.0 bar a)	8.02	0.22
1	$4.73x10^{13}$ (1.5 bar a)	9.82	0.18
1	$6.31e10^{13}$ (2.0 bar a)	11.3	0.16
3	$1.58x10^{13}$ (0.5 bar a)	9.82	0.54
3	$3.15x10^{13}$ (1.0 bar a)	13.9	0.38
3	$4.73x10^{13}$ (1.5 bar a)	17.0	0.31
3	$6.31e10^{13}$ (2.0 bar a)	19.6	0.27

Table 2: Values computed for longitudinal coupling length, L, and velocity perturbation at the terminus, $u_1(x_0)$, for a range of viscosities. The range of viscosities were chosen based on the original work (Kamb and Echelmeyer, 1986; Figure 3).

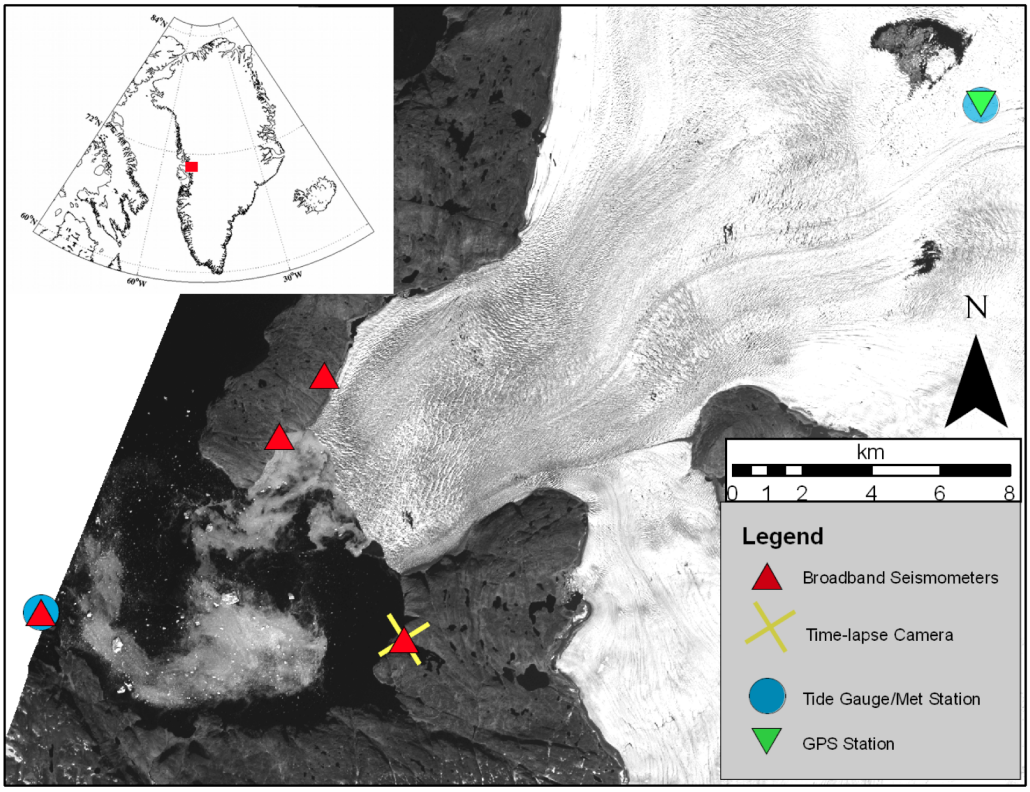

Figure 1: Location of the field site at Store Gletscher, with symbols denoting seismometers (red triangle), on-ice GPS station and co-located automatic weather station (green inverted triangle, blue circle), time-lapse camera (yellow cross), and a tide gauge (blue circle).

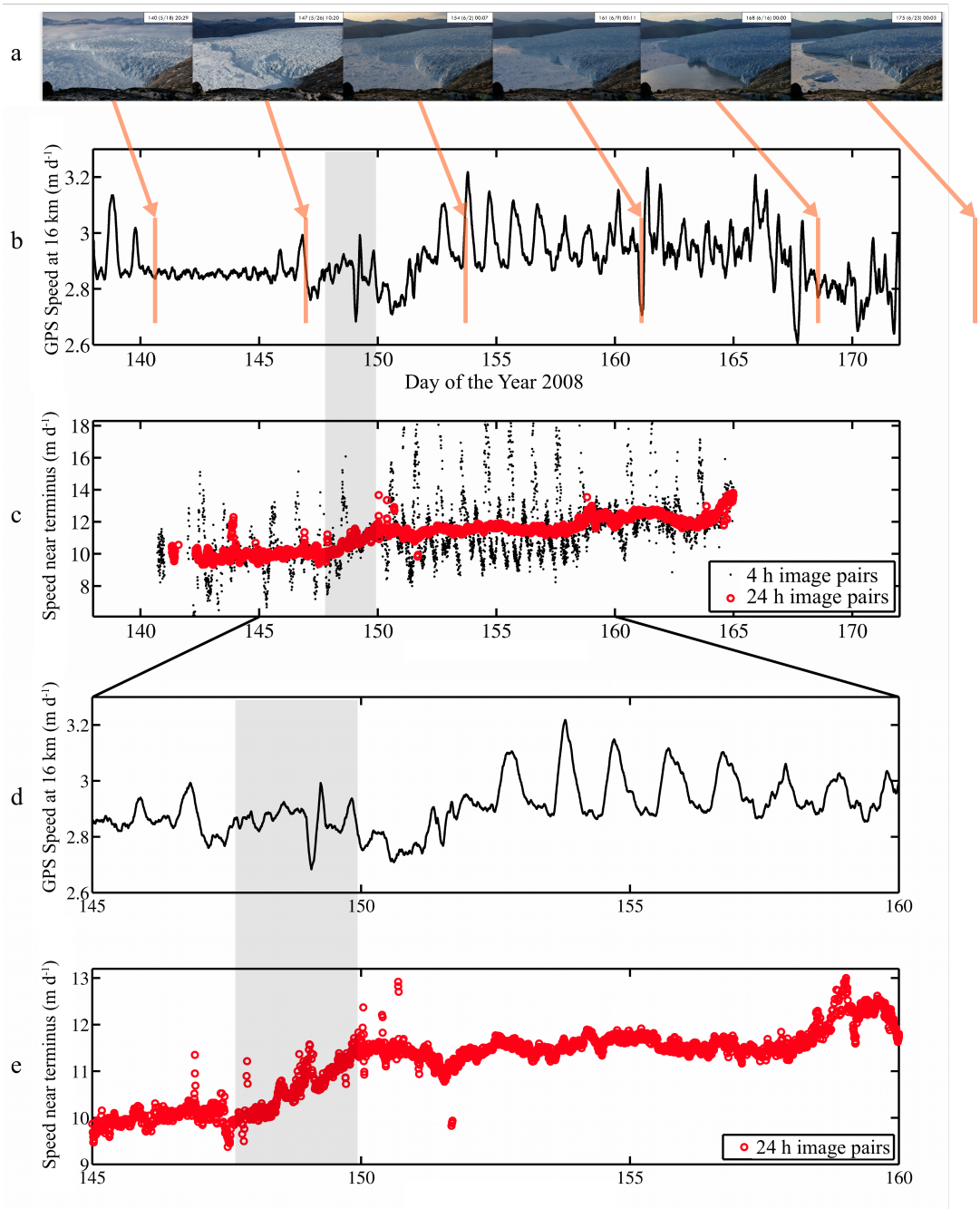

Figure 2: A set of (a.) time-lapse images are shown taken at approximately 7-day intervals showing the evolution of the terminus region. The corresponding ice speed records from (b.) the on-ice GPS station, approximately 16 km from the terminus, and (c.) photogrammetry, near the terminus. The gray bar indicates break-up of the ice mélange, as observed in the time-lapse images. A period between Days 150-160 is emphasized for (d.) the on-ice GPS and (e.) near-terminus region. The gray shaded region indicates the time period when the ice mélange breakup occurred.

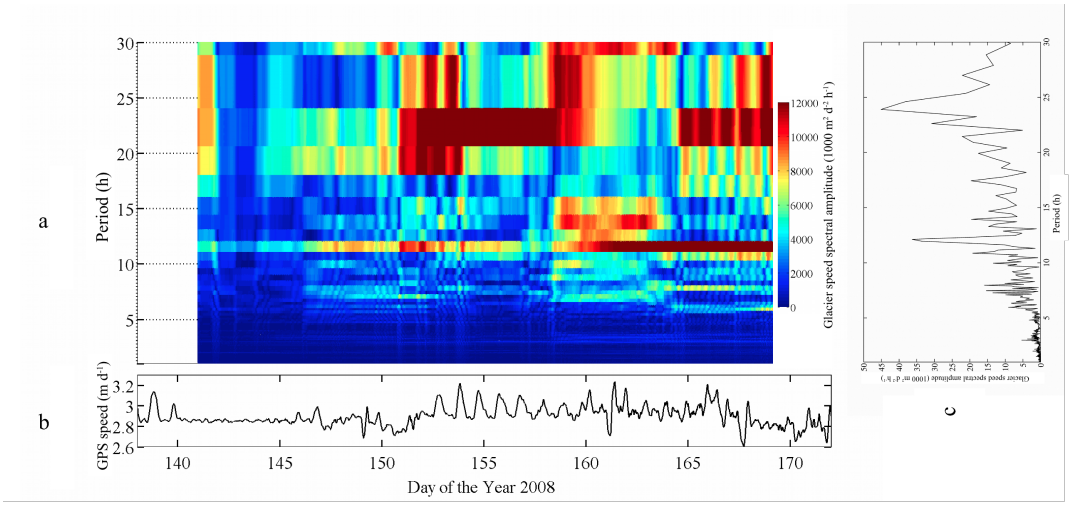

Figure 3: Shown is a (a.) spectrogram of the ice speed observed at the GPS station, ~16 km from the terminus. The bottom panel (b.) includes the speed record for reference. After about Day 150 (break-up of the mélange), the ice speed is more strongly periodic about semi-diurnal (~12 hours) and diurnal (~24 hours) periods, which correspond to ocean tides. At right (c.), we show the spectra of the entire speed record over the period of observation, exhibiting peaks at the same semi-diurnal (~12 hours) and diurnal (~24 hours) periods.

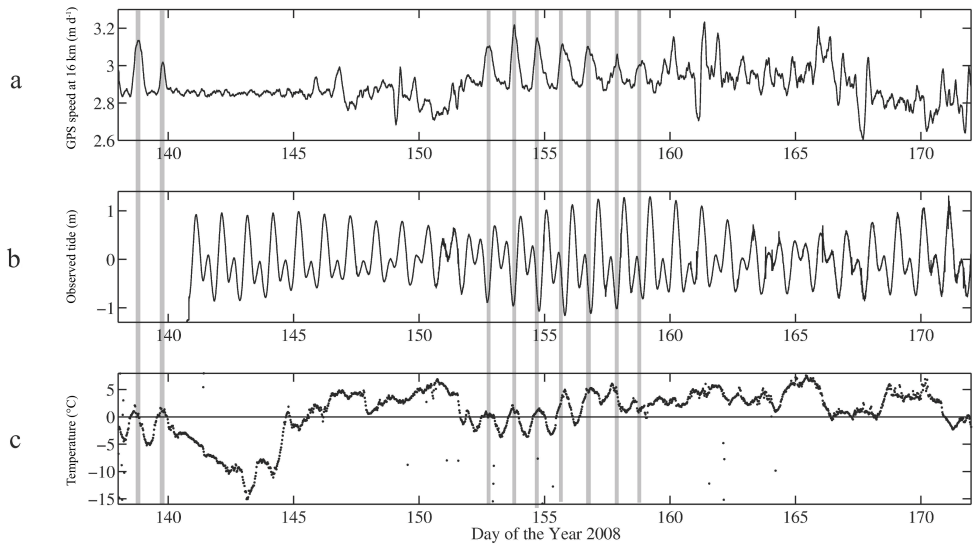

Figure 4: Measurements during the time period between Days 145-165 of (a.) ice flow speed, from the on-ice GPS stations ~16 km from the terminus, (b.) measured tide in the fjord, and (c.) air temperature measured at an automatic weather station co-located with the GPS station.

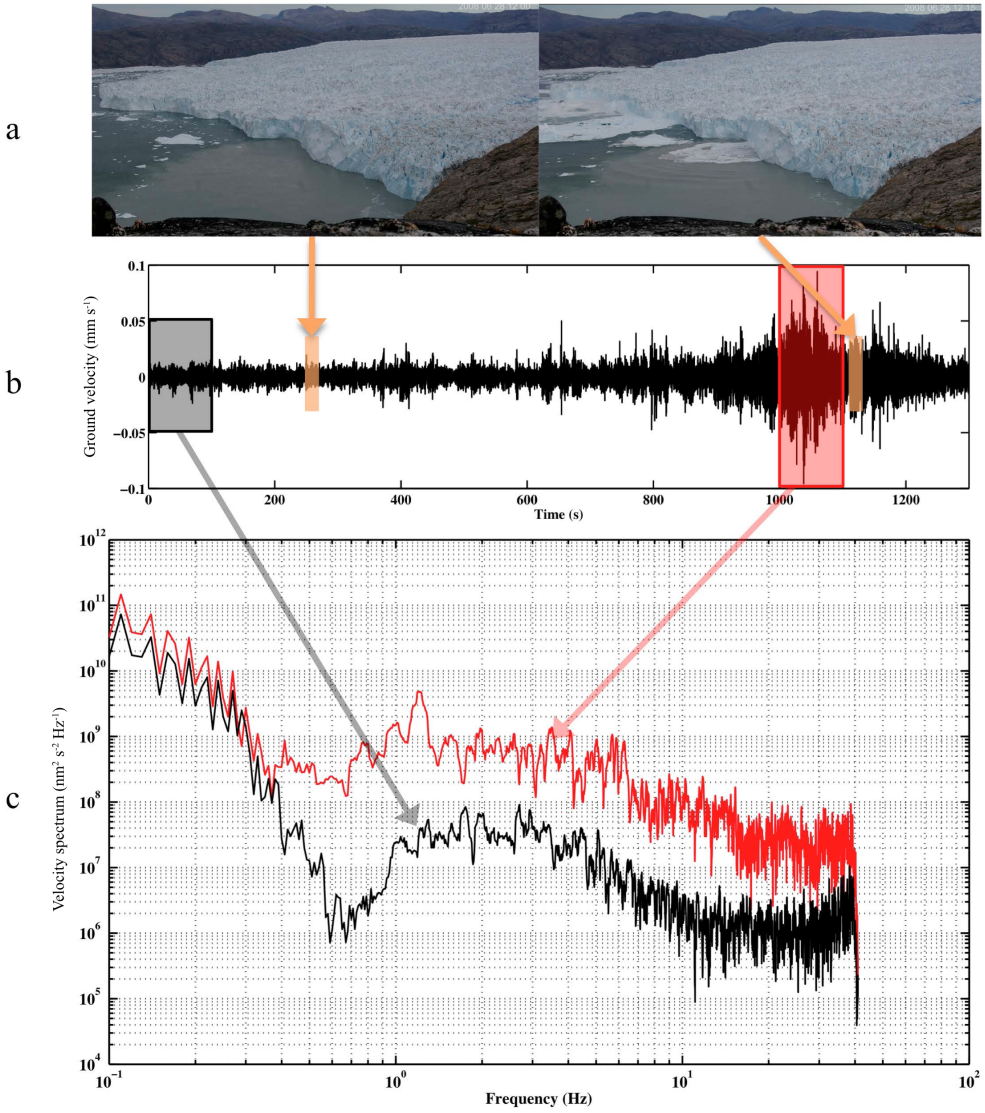

Figure 5: Series of (a.) time-lapse photos indicating a calving event occurring in the left third of the frame. Note a relatively large calving event occurring in the frame, at left. The next panel (b.) depicts the east component seismic record from a station co-located with the time-lapse camera. We compute spectra for windows of 100 seconds during two periods, shown as signal and noise. The spectra (c.) indicates increased energy above noise levels from ~0.3 Hz to the Nyquist frequency.

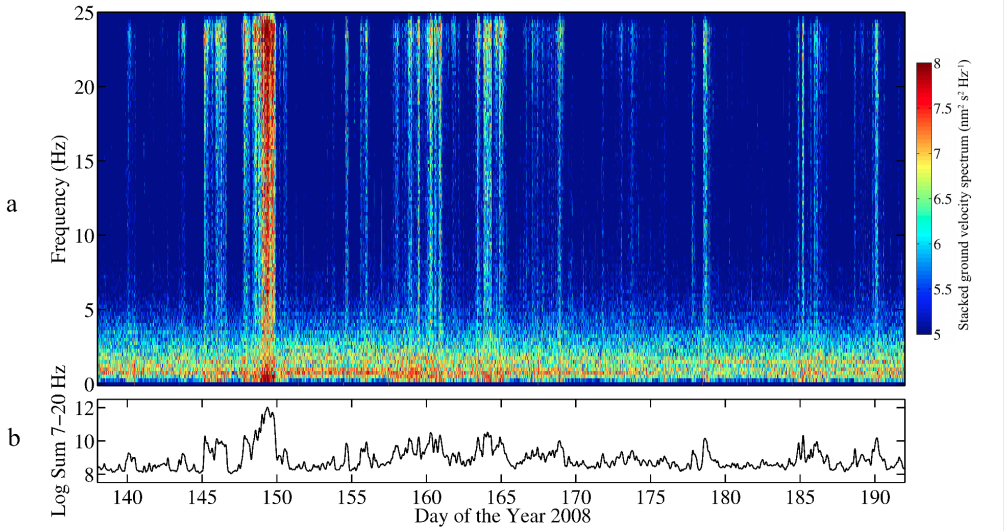

Figure 6: Plot of the computed spectrogram (a.) for the stacked east components of the four stations within the network. Based on examination of the time-lapse photographs, calving events occur during vertical streaks of color above 5 Hz. To limit the amount of noise in choosing a calving activity time series, we choose a frequency band between 7-20 Hz. We sum the energy within this band, take the logarithm, and smooth the time series using a 1000-point window running average, in order to obtain the calving time series (b.).

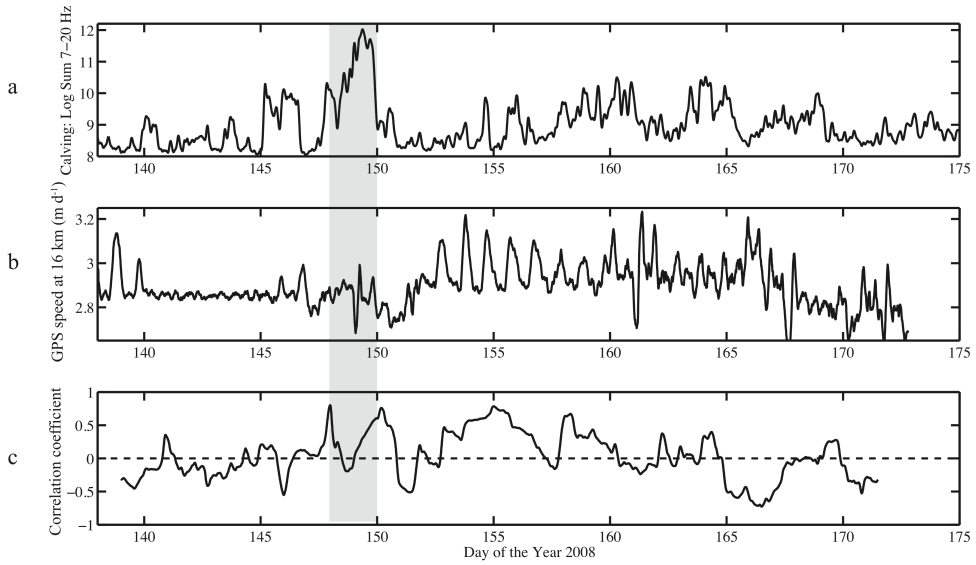

Figure 7: Shown is (a.) the calving activity record from Figure 6b, which is the cumulative seismic energy of the east-west component in 7-20 Hz band for the four seismometers. For comparison, we also show (b.) the GPS ice speed record ~16 km from the terminus. The gray shaded region indicates the ice mélange breakup. Following a brief period of relative quiescence, peaks in the calving activity record and speed perturbations appear to be coherent during some days. We compute a (c.) zero-lag correlation coefficient as a function of time, using a 2-day moving window. Positive correlations suggest periods when calving and speed perturbations are coherent.

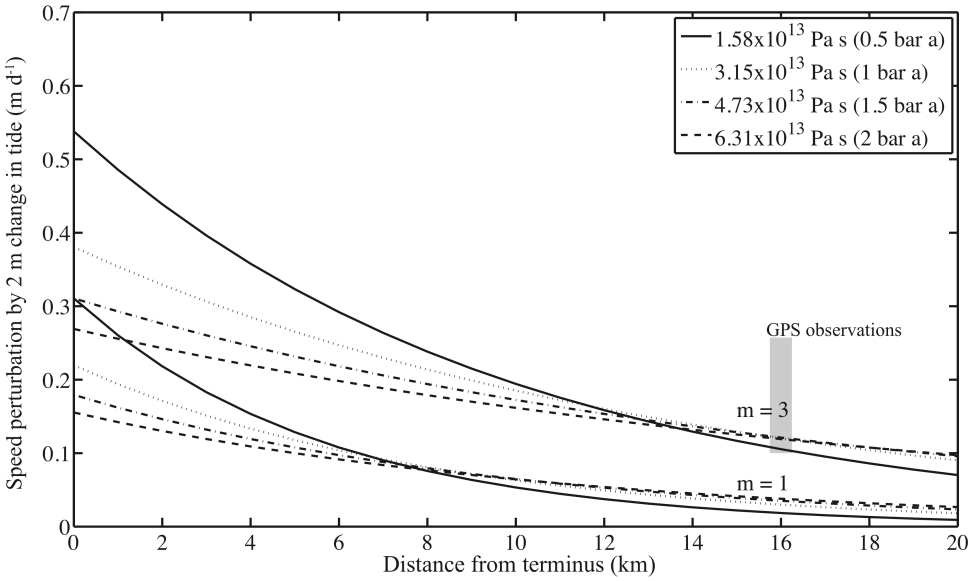

Figure 8: Expected ice speed perturbations, for a range of viscosities and stress exponents and their propagation along-flow, given a two-meter change in the tide at the terminus. The range in perturbation amplitudes for Days 150-160 for the diurnal speed increases from on-ice GPS (Figure 2d) are shown and fit speed perturbation solutions for the stress exponent m=3.

5. PERSISTENT TREMOR WITHIN THE NORTHERN COSTA RICA SEISMOGENIC ZONE

The following Chapter, essentially unchanged, appeared previously in Geophysical Research Letters:

Walter, J. I., S. Y. Schwartz, J. M. Protti, and V. Gonzalez, Persistent tremor of the northern Costa Rica seismogenic zone (2011), Geophys. Res. Lett., 38, L01307, doi:10.1029/2010GL045586.

5. PERSISTENT TREMOR WITHIN THE NORTHERN COSTA RICA SEISMOGENIC ZONE

Abstract

We identify tremor using a spectral detection method and characterize its occurrence over a period of four years (2006-2009) in the vicinity of the Nicoya Peninsula, Costa Rica. Although a few major tremor events accompanied by geodetic slow slip occur, much of the tremor record consists of minor episodes with short duration and no detectable geodetic slip. Its persistent occurrence suggests that some portion of the interface is experiencing slow slip nearly continuously driving small patches to fail in accelerated slip. Locations indicate that much of the tremor occurs at shallow depth, in freely slipping regions of the seismogenic zone. This result is significant in that locations of slow slip and tremor at other subduction zones are largely limited to the downdip frictional transition. Tremor locations may help to refine the heterogeneous distribution of locked and freely slipping patches within the Costa Rica seismogenic zone.

5.1. Introduction

Most of the largest recorded earthquakes occur along the plate boundary at convergent margins. The region of the plate interface capable of rupturing during large earthquakes, termed the seismogenic zone, exhibits frictional stick-slip behavior and is bounded by stably sliding portions both up- and downdip [Scholz, 2002]. Because slow slip and tremor are thought to occur at transitions in frictional stability, the shallowest occurrence of tremor has been used to demarcate the downdip edge of

the seismogenic zone and thus the greatest depth to which earthquake rupture can occur [Chapman and Melbourne, 2009]. More recently, it is becoming clear that frictional transitions from stick-slip to stable sliding are not confined to the up- and downdip edges of the seismogenic zone, but also occur within it. Seismic and aseismic slip have been shown to occur in complementary regions within the seismogenic zone in northeast Japan [Igarashi et al., 2003], Sumatra [Chileh et al., 2008], Chile [Moreno et al. 2010], and Central Peru [Perfettini et al., 2010]. Just as the occurrence of tremor has been used to delineate the downdip extent of seismic rupture, its incidence at shallower depth may help to refine the distribution of asperities within the seismogenic zone. Here we report persistent observations of tremor at the northern Costa Rica margin that locate within the seismogenic zone, at boundaries between locked and more freely slipping regions.

In the vicinity of the Nicoya Peninsula in northern Costa Rica the Cocos and Caribbean plates undergo convergence at a rate of ~90 mm/yr [Norabuena et al., 2004]. This relatively fast rate likely contributes to the abundance and short recurrence interval of large earthquakes. The following five magnitude 7 or greater earthquakes occurred in or around this region during the last century: 1990 M_s 7.2, 1916 M_s 7.4, 1939 M_s 7.3, 1950 M_s 7.7, and 1978 M_s 7.0 [Nishenko, 1991]. The 1950 M_s 7.7 earthquake was the largest event in this time period and both aftershock relocations [Guendel, 1986] and surface deformation [Marshall and Anderson, 1995] suggest a significant portion of the plate interface below the Nicoya Peninsula ruptured during this event. The shallow portion of the inferred rupture zone of the

1950 earthquake corresponds to a locked patch determined by inversion of geodetic data [Norabuena et al., 2004; LaFemina et al., 2009; Outerbridge, 2010]. It is thus the likely location of maximum slip (asperity) during the next large earthquake. Given that the largest two earthquakes preceding the 1950 event occurred in 1853 and 1900 [Protti et al., 2001], the Nicoya Peninsula segment of the plate boundary is late in its earthquake cycle.

The prevalent regional microseismicity of the Nicoya region [DeShon et al., 2006] requires a tremor detection algorithm capable of discriminating tremor from microearthquakes. We developed a spectral detection method and apply it, along with a tremor envelope cross-correlation location technique, to produce a four-year tremor catalog. This catalog displays four major tremor episodes, including: a May 2007 event accompanied by slow slip and studied by Outerbridge et al. [2010], an August 2008 event, and two events in 2009 that are all under study; this paper focuses on the temporal/spatial relationships of the nearly continuous tremor record.

5.2. Data and Methods: Tremor Identification and Location

The Nicoya seismic network (Figure 1a) was deployed in stages between 2006 and 2009. During this time instrumentation varied from an initial network consisting of 5 broadband (deployed in ~ 1.5 m deep vaults) and 3 short-period stations to a configuration of 10 broadband (4 in 5 m deep vaults) and 6 short-period stations, with 4 of these located in 100 m boreholes. Sampling rates also varied between 40 and 100 Hz depending on instrument type. To detect non-volcanic tremor (NVT) we

developed a spectral method (See Supplemental Material), which discriminates tremor energy from prevalent regional microseismicity and cultural noise. This method computes daily network stacked spectrograms and identifies time windows where power exceeds a defined threshold in a tremor (2-7 Hz) and/or earthquake/noise (7-15 Hz) band. An example of this technique applied to a single day of seismic data (2008 JD 215) is presented in Figure 2. While many tremor detections are identified throughout (Figure 2a), the second half of this day contains a lot of energy above 5 Hz. This time period corresponds to 06:00 to 18:00 local time in Costa Rica and the energetic high frequencies are believed to reflect cultural noise. Abundant noise during daylight hours is typical of our entire data set. Although our method can detect tremor during daylight hours, tremor is surely obscured by the high level of noise during this time period. As opposed to noise with peak energy above 5 Hz, local earthquakes possess significant energy across the entire 2-15 Hz band (a few examples of local earthquakes are indicated by arrows in Figure 2c). These are always detected, categorized as both tremor (Figure 2a) and earthquake/noise (Figure 2b) and eliminated from our record of tremor counts (Figure 2d). Applying the detection method described, we obtain the tremor timeseries for 2006-2009 shown in Figure 3a. The relatively low number of tremor events prior to mid-2007 likely reflects fewer stations included in our analysis. Data from 3 additional short-period and 5 broadband stations became available in mid-2007 and mid-2008, respectively. For each detection in the tremor catalog, we employ an envelope cross-correlation method to locate tremor events (See Supplemental Material). Locations of events with

computed horizontal errors less than 5 km (true errors are expected to be much larger due to the simple velocity model and large uncertainties inherent to the envelope cross-correlation location method used) are shown on Figure 1. Applying this error criterion eliminates 70% of the events, so that only the better-located tremor events are retained.

5.3. Results and Discussion

5.3.1 Temporal Behavior of Tremor

The four-year (2006-2009) tremor time series for the Nicoya Peninsula, Costa Rica (Figure 3a) reveals four major tremor episodes in May 2007, August 2008, January 2009, and June/July 2009. Geodetically detectable slow slip accompanied the May 2007 [Outerbridge et al., 2010], August 2008, and June/July 2009 tremor activity with details of the later two events currently under investigation. These four episodes account for only 22% of the tremor record with the remaining activity distributed nearly continuously in time. This is a fairly novel observation, since most accounts of tremor activity at other subduction zones emphasize its temporal clustering. The continuous nature of tremor activity may not be a unique property of the Costa Rica margin, due instead to enhanced tremor detection facilitated by the proximity of the network to shallow tremor sources. Although temporal clustering of tremor is generally emphasized, careful examination of tremor time series from Cascadia [Wech and Creager, 2008], Japan [Suda et al., 2009] and Mexico [Husker et al., 2010] reveals incessant low-level tremor activity between major tremor episodes.

In all regions, only major tremor episodes are accompanied by geodetically recorded slow slip, but most studies still suggest that transient slip is what causes tremor. If tremor is driven by slow slip, its nearly continuous occurrence in northern Costa Rica suggests that transient slip is almost always occurring somewhere, along the ~100 km strike of the plate interface.

Figure 3a appears to indicate a crude recurrence interval of 12-14 months for the more major tremor events, although this estimation is hardly robust given the relatively short monitoring period. Considering all tremor activity, a shorter period cyclic behavior emerges. Ocean loading has been shown to influence tremor activity in Cascadia [Rubinstein et al., 2008; Lambert et al., 2009] and Japan [Nakata et al., 2008]. In order to assess ocean tidal influence on tremor in Costa Rica, we compute spectra for our tremor time series and an equivalent four-year record of tide heights calculated for Puntarenas, Costa Rica (~ 15 km east of the Nicoya Peninsula). Predominant peaks in both datasets occur at approximately 180 days (Figure 3b), corresponding to the equinox period, where tides are enhanced due to earth's proximity to the sun. Although we recognize that the tremor catalog is woefully incomplete being far more likely to be missing detections during daytime hours and in the first 12-18 months of network operation, there is no indication of preferential seasonal detection that would bias the 180 day periodicity. Examination of the temporal tremor and tidal record for a single year of data in 2006, when seismic station coverage was sparse yet uniform, also shows the 180 day periodicity (Figure 3b). The qualitative correlation between spectra peaks at ~180 days suggests that

tremor activity in northern Costa Rica is modulated by the ocean tide. As has been suggested in other regions where tides appear to modulate tremor, the areas of the plate interface where tremor occurs are inherently weak (having very low effective frictional stress) or critically stressed such that small perturbation to stress produce failure.

5.3.2 Spatial Behavior of Tremor

Figure 1a shows the location of all tremor events with horizontal errors less than 5 km, color-coded for time of occurrence as indicated on Figure 3a. Superimposed is the strain accumulation pattern determined from inversion of continuous GPS data collected on the Nicoya Peninsula between 2006-2009 [Outerbridge, 2010]. Both LaFemina et al. [2009] and Norabuena et al. [2004] used episodic GPS measurements with a similar network configuration to define the interseismic surface velocity field, and inverted these data for the locking pattern on the plate interface under the Nicoya Peninsula. These episodic measurements lack the temporal resolution to recognize slow slip events, biasing the picture of interseismic locking. The model of Outerbridge [2010] corrects surface displacements for offsets produced by the well-documented May 2007 slow slip event and inverts interseismic velocities that are about 30% higher than previous studies. This produces a strain accumulation pattern that consists of two fully locked patches, rather than patches locked at only 50-65% of the plate convergence rate obtained by previous studies. Although improved, we still consider this model to be provisional; inversion of

longer, less noisy time series that include the vertical component of velocity are required to significantly improve both the resolution and uniqueness of the model. Given this caveat, a comparison of this strain accumulation model to the location of tremor events reveals that they are anticorrelated. Nearly all of the tremor events locate within the freely slipping regions or at the boundaries between freely slipping and locked regions within the seismogenic zone (Figure 1b).

The up-dip limit of the seismogenic zone is well-defined by the shallowest extent of geodetic locking and the rupture of the 1950 Nicoya (M_S 7.7) earthquake [Schwartz and DeShon, 2007]. The downdip extent has been more difficult to determine given poorer GPS resolution above this transition that results in models of strain accumulation [Norabuena et al., 2004; LaFemina et al., 2009; Outerbridge, 2010] that differ significantly in this region. The deepest interplate seismicity occurs at about 30 km [DeShon et al., 2006], which provides a minimum downdip limit to the seismogenic zone. Given these constraints, it is clear that tremor is distributed throughout the seismogenic zone, rather than at the downdip edge as reported in most other environments. If the occurrence of slow slip and tremor requires a transition in frictional properties from velocity weakening to strengthening, then tremor locations may be used to indicate where these frictional transitions occur within the seismogenic zone and thus the likely locations of maximum slip in future earthquakes.

5.4. Conclusions

We developed a spectral method that can successfully detect tremor in the presence of prevalent microseismicity and cultural noise. We applied it to four years of seismic data (2006-2009) collected on the Nicoya Peninsula, Costa Rica and identified a few major tremor episodes with nearly continuous minor tremor activity in the intervening periods. In contrast to most other regions, Costa Rica tremor occurs at shallow depth, within the seismogenic zone. The tremor occurs within freely slipping regions, adjacent to patches that are presently accumulating strain [Norabuena et al., 2004; Outerbridge, 2010]. Although only the major tremor episodes are accompanied by geodetically detected slow slip, we believe that the copious minor tremor activity is also driven by episodic aseismic deformation that occurs more frequently than previously assumed. Variations in the quantity of tremor in time (major vs. minor episodes) may reflect the magnitude of slow slip deformation, as has been suggested by the linear scaling between tremor duration and geodetic moment in Cascadia [Aguiar et al., 2009]. Both the major and minor tremor episodes tend to occur in similar localities assumed to be conditionally stable regions of the plate interface [e.g. Scholz, 2002]. These regions seem to be driven to failure in slow slip by very small stress perturbations caused by ocean loading. Therefore, the locations of tremor events are providing important information about the frictional properties and thus mechanical behavior of the plate interface.

5.5. Acknowledgements

This work was supported by NSF Awards OCE-0841061 and EAR-0842338 to SYS and a NASA Earth and Space Science Fellowship to JIW. We thank Dan Sampson, Andy Newman, Kim Outerbridge, Jaime Convers, Martin Thorwart, and Waldo Taylor for their invaluable assistance during installation and maintenance of the seismic network. Tidal data for Puntarenas, Costa Rica was obtained using the freely available JTides program (http://www.arachnoid.com/JTides/). Some of the instruments used in the field program were provided by Andy Newman and Zhigang Peng at Georgia Tech and the PASSCAL facility of the Incorporated Research Institutions for Seismology (IRIS) through the PASSCAL Instrument Center at New Mexico Tech. Data collected during this experiment will be available through the IRIS Data Management Center. The facilities of the IRIS Consortium are supported by the National Science Foundation under Cooperative Agreement EAR-0552316 and by the Department of Energy National Nuclear Security Administration.

References

Aguiar, A. C., T. I. Melbourne, and C. W. Scrivner (2009), Moment release rate of Cascadia tremor constrained by GPS, J. Geophys. Res., 114, B00A05, doi:10.1029/2008JB005909.

Chapman, J. S., and T. I. Melbourne (2009), Future Cascadia megathrust rupture delineated by episodic tremor and slip, Geophys. Res. Lett., 36, L22301, doi:10.1029/2009GL040465.

Chileh, M., J.-P. Avouac, K. Sieh, D. Natawidjaja, and J. Galetzka, (2008), Heteroteneous coupling of the Sumatran megathrust constrained by geodetic and paleogeodetic measurements, J. Geophys. Res., 113, doi:10.1029/2007JB004981.

DeShon, H.R., S.Y. Schwartz, A.V. Newman, V. Gonzalez, J.M. Protti, L.M. Dorman, T. Dixon, E. Norabuena, and E. Flueh (2006), Seismogenic zone structure beneath the Nicoya Peninsula, Costa Rica, from 3D local earthquake P- and S- wave tomography, Geophys. J. Int., 164, 109-124.

Guendel, F. (1986), Seismotectonics of Costa Rica: An analytical view of the southern terminus of the Middle America Trench, Ph.D. thesis, 157 pp., Univ. of Calif., Santa Cruz.

Husker, A., S. Peyrat, N. Shapiro, and V. Kostoglodov, (2010), Automatic non-volcanic tremor detection in the Mexican subduction zone, Geofisica Internacional 49 (1), 17-25.

Igarashi, T., T. Matsuzawa, and A. Hasegawa, (2003), Repeating earthquakes and interplate aseismic slip in the Northeastern Japan subduction zone, J. Geophys. Res., 108, doi:10.1029/2002JB001920.

LaFemina, P., T.H. Dixon, R. Govers, E. Norabuena, H. Turner, A. Saballos, G. Mattioli, M. Protti, and W. Strauch, (2009), Fore-arc motion and Cocos Ridge collision in Central America, Geochemistry Geophysics, Geosystems, 10 (1), doi:10.1029/2008GC002181.

Lambert A., H. Kao, G. Rogers and N. Courtier, (2009), Correlation of tremor activity with tidal stress in the northern Cascadia subduction zone, J. Geophys. Res., 114, B00A08, doi:10.1029/2008JB0006038.

Marshall, J. S. and R. S. Anderson (1995), Quaternary uplift and seismic cycle deformation, Peninsula de Nicoya, Costa Rica, Geol. Soc. Am. Bull., 107(4): 463-473.

Moreno, M., M. Rosenau, and O. Onchen (2010), 2010 Maule earthquake slip correlates with pre-seismic locking of Andean subduction zone, Nature, 467, doi:10.1038/nature09349.

Nakata, R., N. Suda, and H. Tsuruoka, (2008), Non-volcanic tremor resulting from the combined effect of Earth tides and slow slip events, Nature Geoscience, 11, doi:10.1038/ngeo288.

Nishenko, S. P. (1991), Circum-Pacific seismic potential: 1989-1999, Pure and Applied Geophysics, 135(2): 169-259.

Norabuena, E., et al. (2004), Geodetic and seismic constraints on some seismogenic zone processes in Costa Rica, J. Geophys. Res., 109, B11403, doi:10.1029/2003JB002931.

Outerbridge, Kimberly C. Slow Slip Beneath the Nicoya Peninsula, Costa Rica and It's Effect on the Interseismic Cycle, PhD Thesis: University of Miami, 2010.

Outerbridge, K. C., T. H. Dixon, S. Y. Schwartz, J. I. Walter, M. Protti, V. Gonzalez, J. Biggs, M. Thorwart, and W. Rabbel (2010), A Tremor and Slip Event on the Cocos-Caribbean Subduction zone as measured by a GPS and Seismic Network on the Nicoya Peninsula, Costa Rica, J. Geophy. Res., doi:10.1029/2009JB006845

Perfettini, H., J.-P. Avouac, H. Tavera, A. Kositsky, J.-M. Nocquet, F. Bondoux, M. Chlieh, A. Sladen, L. Audin, D. L. Farber, and P. Soler (2010), Seismic and aseismic slip on the Central Peru megathrust, Nature, 465: 78-81, doi:10.1038/nature09062.

Protti, M. Güendel, F. y Malavassi, E., Evaluación del Potencial Sísmico de la Península de Nicoya; Editorial Fundacion UNA, 1ra. edicion, Heredia, Costa Rica, 2001, 144 p.

Rubinstein, J.L. et al., (2008), Tidal modulation of nonvolcanic tremor, Science, 319, 186, doi:10.1126/science.1150558.

Scholz, C. H. (2002), The Mechanics of Earthquakes and Faulting, 2nd Edition, Cambridge University Press.

Schwartz, S.Y. and H.R. DeShon (2007), Distinct Up-dip Limits to Geodetic Locking and Microseismicity at the Northern Costa Rica Seismogenic Zone: Evidence for Two Mechanical Transitions, in The Seismogenic Zone of Subduction Thrust Faults, eds. T. Dixon and J.C. Moore, Columbia Univerisity Press, New York, 576-599

Suda, N., R. Nakata, and T. Kusumi, (2009), An automatic monitoring system for nonvolcanic tremors in southwest Japan, J. Geoohys. Res., 114, B00A10, doi:10.1029/2008JB006060.

Wech, A. G., and K. C. Creager (2008), Automated detection and location of Cascadia tremor, Geophys. Res. Lett., 35, L20302, doi:10.1029/2008GL035458.

5.6. Appendix A: Spectral Tremor Detection Method

We stack unfiltered, daylong, east-component seismograms for all the available stations within the network and normalize for the number of operating stations and daily mean energy across all frequencies. We produce daily

spectrograms with ~82 s windows and 50% overlap. Peaks of energy are identified within certain bands: the tremor band is chosen as 2-7 Hz and the earthquake/noise band 7-15 Hz. The spectrograms for the entire duration of the dataset (2006-2009) are computed and a baseline threshold established above which detections are defined. Because we want to allow positive tremor or earthquake/noise detections when power in a significant portion of the defined frequency bands exceed the baseline threshold, we establish a required percentage of the frequency band that must exceed the baseline threshold (termed the threshold percentage) for a positive detection. Our algorithm scans the entire dataset and for each time window determines the percentage of signal within the tremor and earthquake/noise bands, that falls above the baseline threshold. All time windows where this percentage exceeds the tremor and/or earthquake/noise threshold percentage are considered a positive tremor and/or earthquake detection. Time windows that contain only a tremor detection are retained, if an earthquake/noise-band detection occurs within the same window as a tremor detection, that tremor detection is negated.

In order to determine threshold percentages for tremor and earthquake/noise detections, we generated 10,201 tremor detection catalogs using data for several weeks surrounding the May 2007 slow slip event and different percentages between 0% and 100%, in 1% increments. We then compared these detection catalogs with an analyst-determined hand counted tremor catalog for the same time period [Outerbridge et al., 2010]. The visually determined tremor catalog indicated that tremor started abruptly on Julian Day (JD) 136, continued at a high level through JD

142, and tapered off by JD 146. The ten days preceding tremor initiation were virtually devoid of tremor activity. We tuned the threshold percentages to best fit this pattern by calculating the ratio of tremor detections between JD 136-146 to JD 125-135 for each of the 10,201 tremor catalogs and chose the threshold percentages that maximized this ratio. The highest ratio attained for the computed catalogs was 16.5, corresponding to tremor and earthquake percentage thresholds of 46% and 28%, respectively. These values are likely network and region specific. A combination of the high microseismicity and cultural noise for the Nicoya region likely determines the best values. This threshold percentage method could be easily tailored for use in other tectonic environments.

5.7. Appendix B: Comparison of Automatic Detection to Visually Determined Catalog of Tremor

The visually determined tremor catalog for 2007 presented in Outerbridge et al. [2010] counts the number of tremor episodes that occur within each hour lasting at least four minutes and computes tremor durations for the entirety of each episode. Because tremor episodes often consist of several tremor bursts separated by quiet intervals, this catalog overestimates tremor durations. Both the handpicked and automated tremor catalogs identify peak tremor activity in 2007 on JD 137. On this day the hand-picked catalog contains 36 tremor episodes totaling almost 400 minutes, while the automated detection algorithm described here finds 22 events with a total estimated duration of only 30 minutes. The spectrogram for this day displays an

unusually high level of noise during both local daylight and night-time hours that unfortunately obscures a lot of the tremor activity. Automatic tremor detection methods developed for use in Mexico [Husker et al., 2010] and Cascadia [Wech and Creager, 2008] also suffer from reduced tremor counts compared to handpicked determinations of tremor. These researchers have attributed this to storm activity and cultural noise, which both reduce automated detection compared to visual inspection. Brudzinski and Allen [2007] recognized the difficulty of detecting tremor in the presence of cultural noise and only searched for tremor during the twelve, quiet night-time hours. Because automated tremor detection algorithms consistently underestimate tremor when compared with visual inspection, we consider our tremor catalog to provide a lower bound estimate of tremor activity.

5.8. Appendix C: Tremor Location Method

Tremor events are located using an envelope cross-correlation method to determine the phase lag across the network similar to Obara [2002]. Daylong seismograms for each station are band-passed at 2-7 Hz, smoothed, decimated to a 2 Hz sample rate, and converted to single-sided functions or envelopes. Subtracting the mean and dividing by the standard deviation normalizes the envelopes for each station. We determine time lags for the maximum cross-correlation coefficient relative to one of the stations and exclude stations that do not have a correlation coefficient greater than 0.65. With the phase lag, we locate the tremor events with

HYPOINVERSE [Klein, 1978], using a one-dimensional S-wave model determined for this region [DeShon et al., 2006].

Appendix References

Brudzinski, M. R., and R. M. Allen (2007), Segmentation in episodic tremor and slip all along Cascadia, Geology, 35, 907-910.

DeShon, H.R., S.Y. Schwartz, A.V. Newman, V. Gonzalez, J.M. Protti, L.M. Dorman, T. Dixon, E. Norabuena, and E. Flueh (2006), Seismogenic zone structure beneath the Nicoya Peninsula, Costa Rica, from 3D local earthquake P- and S- wave tomography, Geophys. J. Int., 164, 109-124.

Husker, A., S. Peyrat, N. Shapiro, and V. Kostoglodov, (2010), Automatic non-volcanic tremor detection in the Mexican subduction zone, Geofisica Internacional 49 (1), 17-25.

Klein, F.W. (1978), Hypocenter location program HYPOINVERSE, U.S. Geological Survey Open-File Report 78-694, 113 pp.

Obara, K. (2002), Nonvolcanic deep tremor associated with subduction in southwest Japan, Science, 296: 1679-1681.

Outerbridge, K. C., T. H. Dixon, S. Y. Schwartz, J. I. Walter, M. Protti, V. Gonzalez, J. Biggs, M. Thorwart, and W. Rabbel (2010), A Tremor and Slip Event on the Cocos-Caribbean Subduction zone as measured by a GPS and Seismic Network on the Nicoya Peninsula, Costa Rica, J. Geophy. Res., doi:10.1029/2009JB006845

Wech, A. G., and K. C. Creager (2008), Automated detection and location of Cascadia tremor, Geophys. Res. Lett., 35, L20302, doi:10.1029/2008GL035458.

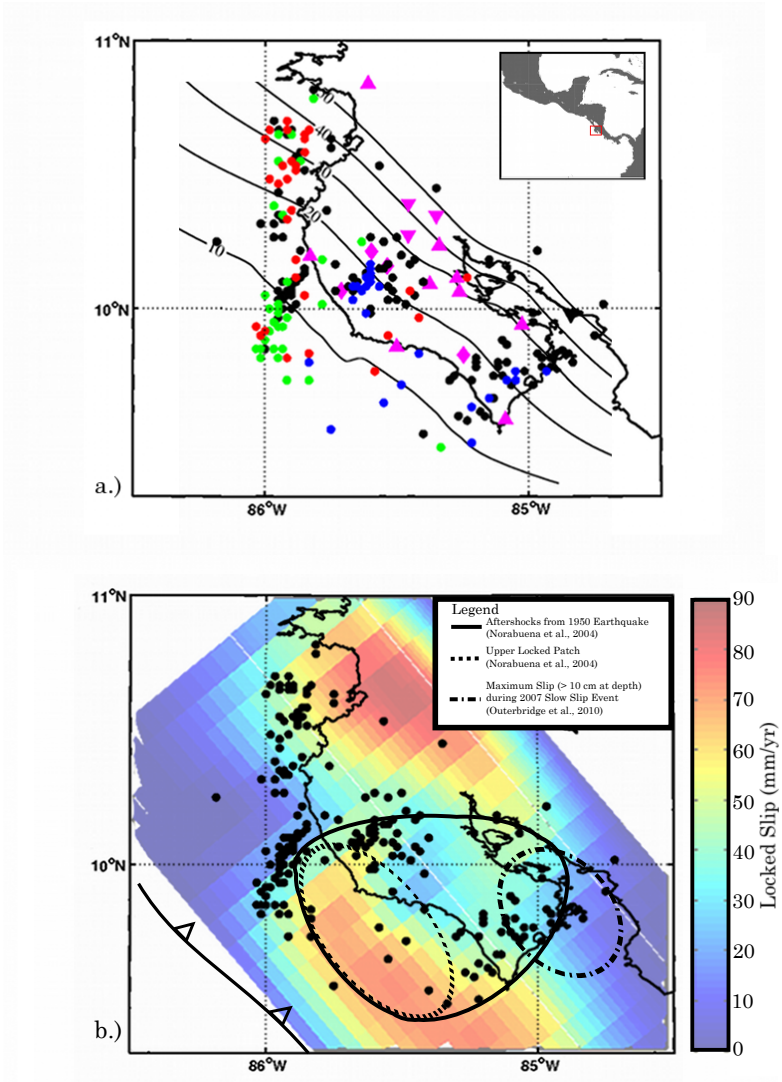

Figure 1: a) Map of tremor locations color coded to correspond to the temporal record of tremor activity from Figure 3a, including major (blue-May 2007, green-August 2008, and red-April 2009) and minor (black) tremor events. Seismic stations are indicated by the magenta symbols with inverted triangles and diamonds representing borehole and deep vault sites, respectively. The black inverted triangle indicates the location of Puntarenas. b) Contours of locked slip on the plate interface from Outerbridge [2010] with all tremor locations in black. The plate rate approaches ~90 mm/yr [Norabuena et al., 2004]. The aftershock area of the 1950 Nicoya Peninsula Earthquake (Ms 7.7), the shallow locked patch determined by episodic GPS measurements [Norabuena et al., 2004], and the region of maximum slip at depth (greater than 10 cm) during the 2007 Slow Slip Event [Outerbridge et al., 2010] are also indicated.

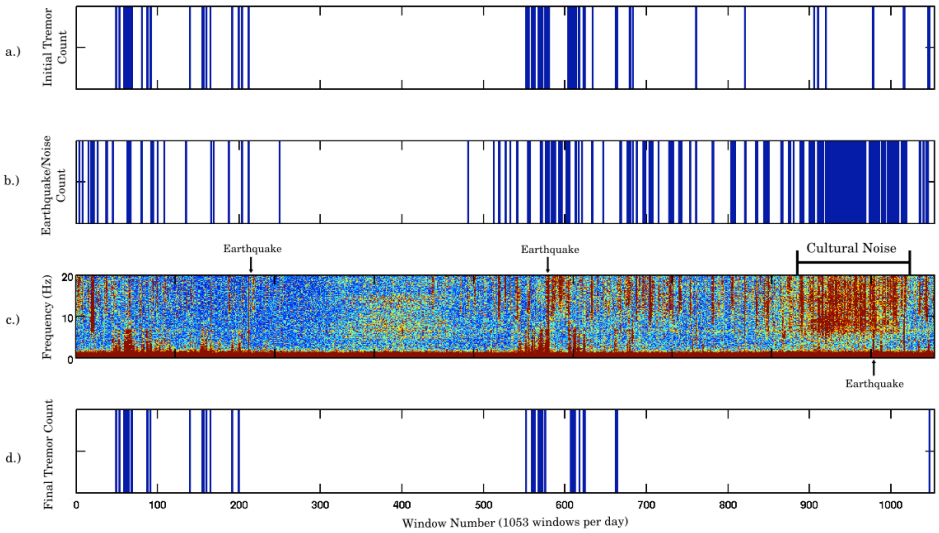

Figure 2: Illustration of the spectral detection method for one day (Day of the Year 2008) showing (a) initial tremor detections, (b) earthquake and cultural noise detections, (c) the daily stacked network-wide spectrogram with the color axis saturated at the detection threshold (red) and (d) final tremor detections determined by subtracting (b) from (a). The high level of cultural noise and several earthquakes are indicated on the spectrogram.

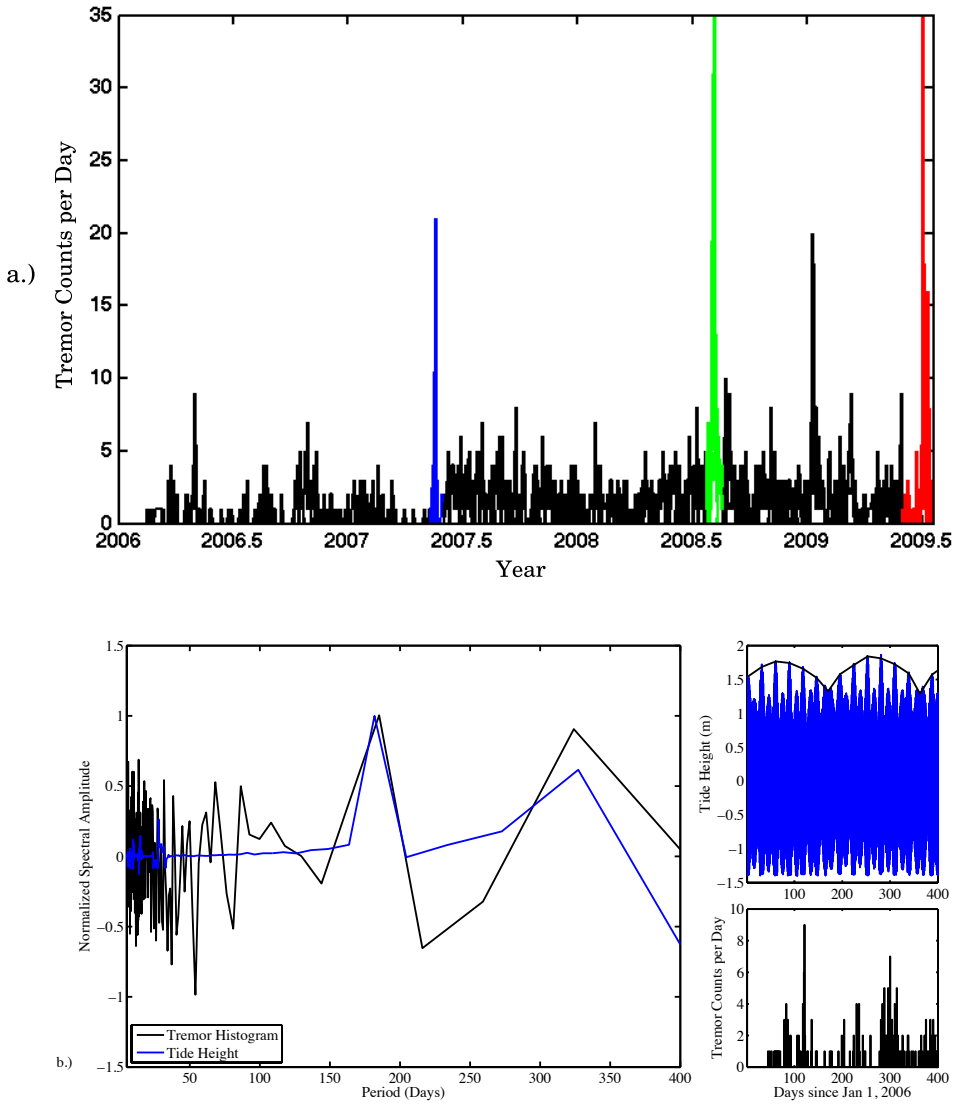

Figure 3. (a) Tremor histogram of daily events from 2006 through mid-2009. Three of the major tremor episodes are color-coded and event locations indicated in Figure 1 (blue for May 2007, green for August 2008, and red for April 2009). (b) Left panel: Spectra computed for the 2006-2009 tremor and tide height records calculated for Puntarenas, Costa Rica. Right panels: The 2006 tremor and tide height data to highlight the 180 day periodicity.

6. SHALLOW, OFFSHORE TREMOR AND SLOW SLIP AT THE NICOYA PENINSULA, COSTA RICA

6. SHALLOW, OFFSHORE TREMOR AND SLOW SLIP AT THE NICOYA PENINSULA, COSTA RICA

Abstract

We present evidence that a tremor and slow slip event occurred offshore of the Nicoya Peninsula, Costa Rica, in August 2008. The temporal coincidence of offshore tremor, very low-frequency earthquakes (VLFEs), slow slip on northwest coastal GPS stations, and a pressure transient in an IODP borehole, all indicate slow slip occurring at shallow depths. The periodicity of the tremor during this particular event corresponds to the peak Coulomb stress forced by the semi-diurnal ocean tide. Based on beamforming data, we loosely constrain that the VLFE activity occurs to the southwest of the Peninsula, possibly in the same source region as the tremor. Our interpretation of this activity is that a slow slip event occurred southwest of the network and that the presence of tremor may be a manifestation of slip in zones that are in a frictional transition between stably sliding and locked interfaces.

6.1. Introduction

At a subduction zone, as the oceanic plate slides beneath the continental plate, the motion is resisted by friction at their contact. This friction is overcome as elastic energy is released as earthquakes of all sizes, including some of the world's largest on record. Within the central part of the megathrust, the largest earthquakes nucleate and propagate. Frictional conditions that control the accumulation of strain across the interface can vary along-dip and along-strike, due to contact roughness, presence of soft sediments at the megathrust interface, and a number of other physical parameters.

Recent efforts have included campaigns to delineate areas of the plate interface along-strike and along-dip that are frictionally coupled, using continuous and campaign GPS (Chapman and Melbourne, 2010). The widespread use of continuous GPS at these margins has led to the discovery of episodic slow slip at some of these margins.

Slow slip in Cascadia and Japan is often accompanied by episodes of non-volcanic tremor (Obara, 2002; Rogers and Draggert, 2003). In the last decade, the number of observations of tremor at different subduction zones and intraplate faults has increased significantly, including southwest Japan (Obara, 2002), Cascadia (Rogers and Draggert, 2003), Mexico (Payero et al., 2008), Alaska (Peterson and Christensen, 2009), the San Andreas fault (Nadeau and Dolenc, 2005), and Costa Rica (Outerbridge et al., 2010; Walter et al., 2011). Many of these observations include tremor occurring in regions typically down-dip of the frictionally locked seismogenic zone or in areas believed to be stably sliding.

At the shallow limit of subduction, near the trench, ocean crust can push its way beneath the more buoyant continental crust. When significant ocean sediments exist, an accretionary prism forms and may have important controls upon frictional coupling (Moore and Saffer, 2001). The presence of sediments decreases the elastic rigidity, which controls accumulation of elastic strain. Thus, at a margin like the Nicoya Peninsula, which has little to no sediment entering the trench, strain may accumulate at shallower depths and further towards the trench than in other subduction zones. The strain can either release as earthquakes or stably-sliding slow slip events.

Also at the shallowest limits of the subduction interface, recently, a new class of earthquakes deficient in seismic energy above 0.05 Hz, called very low frequency earthquakes (VLFEs) have been discovered near the trench (Ito and Obara, 2006), as well as down-dip of the seismogenic zone (Ito et al., 2009). The VLFE activity often occurs during other manifestations of slow slip (tremor) and can occur in areas that span the seismogenic zone where its presence is detectable simultaneously up-dip and down-dip (Hirose et al., 2010). Thus, exploring the range of behaviors and its presence in other regimes will allow it to be a better-studied phenomena.

In addition, a certain class of earthquakes often rupture at shallow depths at the plate interface, called tsunami earthquakes. Tsunami earthquakes produce larger tsunamis than would have been forecasted, given the surface-wave magnitude, and are often depleted in short-period energy (Bilek and Lay, 2002). In 1992, slightly north of the study area and adjacent to Nicaragua, a large tsunami earthquake ruptured a large portion of upper plate, up-dip of the seismogenic zone, from ~10 km depth extending all the way to the trench (Ide et al., 1993). Tsunami size is largely dependent upon the volume of seafloor, and thus, crustal deformation that occurs underwater is an important hazard.

The Nicoya Peninsula undergoes convergence at a rate of ~90 mm/yr (Norabuena et al., 2004), which is a relatively fast rate for subduction zones. This rate likely contributed to the five magnitude 7 or greater earthquakes observed on or near Nicoya in the last century (Nishenko, 1991). An M_s 7.7 earthquake occurred in 1950 and a series of magnitude-7 sized events occurred in 1853 and 1900 (Protti et

al., 2001), prompting a high level of alert within local government agencies, as evidence suggests the area is late in its earthquake cycle.

Understanding deformation at both frictional limits of a seismogenic zone would be societally useful for forecasting earthquake hazards. This paper provides evidence of tremor and slow slip at the up-dip, shallow limit. We build on previous results from Walter et al. (2011) and provide further evidence that a plate interface slow slip event occurred in August 2008 at the Nicoya Peninsula. Furthermore, we identify and constrain some characteristics of VLFEs that occur during this slow slip activity.

6.2. Observations

6.2.1. Tremor semi-diurnal periodicity

During August 2008, a large amount of tremor locates offshore (Figure 1). When the previously published tremor record (Walter et al., 2011) during August 2008 is binned hourly, the binned tremor activity record appears to exhibit a strong semi-diurnal (12 hour) periodicity. In order to determine the nature of the tidal forcing, we used the tidal program SPOTL (Agnew, 1996) to compute the ocean tide heights near the tremor locations. Stress is determined via plane stress transformations (e.g. Wilcock 2009) for a 23 degree dipping fault with a rake of 90 degrees (reverse fault). We choose a 23 degree dip as this is the geometry of the Wadati-Benioff zone in this region (Protti et al., 1994). From rock mechanics, the

total stress promoting failure is called the Coulomb stress (e.g. Scholz, 2002) and can be calculated:

$$\Delta\sigma_c = \Delta\tau - \mu_f \Delta\sigma_n \qquad (1)$$

where σ_c is the Coulomb stress, τ is the shear stress, μ_f is the coefficient of friction, and σ_n is normal stress. We use an average value of 0.6 for the coefficent of friction. Figure 2 shows the shear stress, normal stress, and Coulomb stress due to ocean loading on the fault plane at a dip of 20 degrees, plotted with tremor counts. The phases of positive shear and Coulomb qualitatively correlate well with tremor counts. The tremor activity occurs primarily during 02:00 and 14:00 UTC, which corresponds to 20:00 and 08:00 local time, respectively. Therefore, observations of tremor do not appear to be biased towards occurring only during periods of time when cultural noise is low.

6.2.2. VLFE presence and source constraints

In order to detect the presence of very low frequency earthquake (VLFE), we bandpass between 0.02-0.05 Hz the east component daylong seismograms during the period between Days 210-230. We identify periods of time when there is long-period energy that is coherent across multiple stations. The VLFEs appear to lack body waves, making the determination of an origin location and time difficult with such long period energy. An example set of seismograms showing an active period of VLFEs is shown in Figure 3. The VLFE catalog is included as a supplemental table

and a histogram of the activity is shown with the tremor activity in Figure 4. All of the 54 events occur during periods of tremor activity.

In order to constrain some characteristics of the source and waveform, we next perform beamforming on the long-period energy. We use the vertical component seismograms that are band-passed between 0.02-0.05 Hz. We utilize delay-and-sum beamforming to determine the azimuth and speed of the seismic wave. Beamforming is useful when the source location and/or propagation velocity are unknown or poorly constrained. We construct a beam for each of 360 degrees, j, of source locations surrounding our 2010 network. We loop through apparent wave velocities, v, from 3,000 to 7,000 m/s at 100 m/s intervals and compute the slowness, **u**, for each azimuth by

$$\begin{aligned} \mathbf{u} &= (u_x, u_y) \\ &= \left(\frac{\sin\theta}{v}, \frac{\cos\theta}{v} \right) \end{aligned} \qquad (2)$$

The waveforms from all the stations, y_i, are time-shifted according to the travel-time for a particular plane wave apparent velocity relative to a point at the center of the array. We stack the seismograms at each of these iterations in j, to produce the beam, $B_j(t)$, at that azimuth, where

$$B_j(t) = \sum_{i=1}^{N} y_i(t + \mathbf{r}_i \cdot \mathbf{u}) \qquad (3)$$

We take the maximum amplitude at each azimuth, j, for iterations of v. The maximum beamform for an individual event during Day 216 is shown on the polar plot in Figure 5a. The highest amplitude stack is at an azimuth of ~225° and wave speed of 3,000-

4,000 m/s, which is the also the approximate azimuth of the offshore tremor. The value of 3,000-4,000 m/s is consistent with a surface wave velocity for this region (DeShon et al., 2006).

In order to expand this analysis to other events, we perform the beamforming technique on all three components data for all the events. We beamform each event and each component, as described previously, and record the azimuth with the maximum amplitude beam. We average the preferred azimuth of the threee components for each of the events and those data are shown in Figure 5b, in addition to error bars defined by 1σ standard deviation. We only show azimuths for those data where the standard deviation is less than 80°, leaving 26 of 54 events that are shown in Figure 5b.

6.2.3. Coastal and seafloor evidence slow slip

Aside from the tremor locations and inferences regarding the source of VLFEs, we have two lines of tangential evidence that a slow slip and tremor event occurred to the west of the Nicoya Peninsula. First, at coastal station PNEG, a geodetic offset, indicative of slow slip, occurred over a period of approximately 20 days (Figure 4b). The geodetic slow slip begins at roughly the same time as the largest peaks in tremor activity. Analyzing the same data, Jiang et al. (2012) also report slow slip event during this time period, present at only a few western stations. Continuous GPS displacements, which indicates that some coastal stations observe the slow slip event, is included as supplementary material (Supplementary Figure S1).

Another line of evidence for offshore upper-plate deformation includes pressure transients observed in the IODP Site 1255 borehole (Davis et al., 2011). The site is located 400 m arc-ward of the trench and drilled through the overlying sediment. The location of the offshore borehole appears on Figure 1 as a red star. In Figure 4c, a pair of pressure transients occurs approximately 15-25 days following peaks in tremor activity. The positive sign of the anomaly likely represents contraction in the prism sediments (Davis et al., 2011), consistent with the interpretation that slip occurred on the plate interface. Similarly, previous measurements of seafloor porewater flux in this area have been attributed to seafloor deformation during inferred aseismic slip (Brown et al., 2005).

6.3. Discussion

We have shown evidence of an offshore slow slip event that occurred in August 2008. Tectonic tremor that occurs during this period locates offshore, west of the Nicoya Peninsula (Walter et al., 2011). When we analyze the temporal clustering of that data, we find that the tremor is semi-diurnally periodic and is coherent with peaks in the computed coulomb stress. The strong tidal periodicity of tremor at Costa Rica, observed during August 2008, suggests that prior to the tremor and slow slip event, the plate interface approaches a critical threshold, such that the small Coulomb stress changes promote tremor activity. In addition to the location of this tremor, we observe VLFEs that appear to propogate from similar or adjacent areas. Continuous GPS stations and pressure transients in a near-trench borehole also provide further

evidence that a slow slip event occurred at shallow depths. Due to the lack of direct seafloor geodetic tools, we cannot precisely delineate the area that deformed during the event.

VLFE activity is most prevalent during vigorous periods of tremor activity. The synchronicity of VLFE and tremor activity suggests that they may be located in the same place. Further constraints on location from beamforming suggests that the VLFE waveforms originate to the southwest of the Nicoya network. If the beamforming results are valid, then this suggests that slow slip is also occurring further west of the Peninsula and in an area of the plate interface adjacent to Nicaragua. Though poorly constrained, if slow slip occurs northwest of the tremor in addition to the area of vigorous tremor, then tremor appears to occur at the frictional transition between the slow slip event and the frictionally locked portion of the plate interface (Feng et al., 2012).

6.4. Conclusions

In summary, we have shown evidence that a shallow slow slip event occurred offshore of the northwest portion of the Nicoya Peninsula. The tremor during this time period locates offshore and is semi-diurnally periodic. In addition, coastal GPS and pressure transients in a borehole observatory near the trench provide evidence of shallow slip on the plate interface. Further evidence is the presence of VLFEs which, when beamformed, seem to originate in a similar source region. All these data

suggest that a slow slip event occurred at this subduction zone, which is at the shallowest limit of the plate interface.

6.5. Acknowledgements

This work was supported by an NSF grant EAR 0842338 to S.Y.S. and a NASA Earth and Space Science Fellowship to J.I.W. We thank Earl Davis and Martin Heesemann for providing the pressure time series from the IODP borehole observatory. GPS network equipment services and field support provided by the UNAVCO Facility with support from the National Science Foundation (NSF) and National Aeronautics and Space Administration (NASA) under NSF Cooperative Agreement No. EAR-0735156. Seismic instruments were provided by the PASSCAL facility of the Incorporated Research Institutions for Seismology (IRIS) through the PASSCAL Instrument Center at New Mexico Tech. Data collected during this experiment will be available through the IRIS Data Management Center. The facilities of the IRIS Consortium are supported by the National Science Foundation under Cooperative Agreement EAR-0552316 and by the Department of Energy National Nuclear Security Administration.

6.6 Appendix A: Coulomb stress comparison with alternate tremor catalog

In Section 6.2.1, we calculated the Coulomb stress change due to the influence of ocean tides on the plate interface. Figure 2 qualitatively suggests that most of the tremor activity occurs during positive peaks in the Coulomb stress. In order to affirm

this inference of tidal modulation of tremor activity, we present an alternative tremor catalog for this time period (M. Kim, personal communication). The method, as described by Kim et al. (2011), is an adaptation of the Wech and Creager (2008) envelope cross-correlation method. Kim et al. (2011) cross-correlate waveform envelopes in two different frequency bands, ideally to remove the small earthquakes as possible false detections.

We bin the tremor activity identified using the Kim et al. (2011) method into hourly bins. The tremor activity is shown on Figure A1, along with stresses computed as in Section 6.2.1. Qualitatively, this alternate tremor catalog appears to confirm observations made in Section 6.2.1, using the Walter et al. (2011) method, which indicates coherence between Coulomb stress and tremor activity.

6.7 Appendix B: Beamforming test on catalogued earthquake

In order to test the accuracy of the beamforming algorithm, we test the beamforming algorithm on high frequency seismic data during a period of time when we located an earthquake offshore. The event occurred at 06:00:37 on August 5 (Day 218), 2008 and was located at position 9.5782°N, 84.6599°W, depth 18 km, which is approximately 50 km directly east of station PNCB, and at an azimuth of 123° from the center of the array. The array geometry and earthquake location are shown in Figure B1.

We use the vertical component seismograms, remove the instrument response, and filter the data using a bandpass filter at 1-3 Hz. Next, we perform the

beamforming analysis, as described in Section 6.2.2. The beamforms appear in Figure B2. The maximum beam is at an azimuth of 78° and a plane wave speed of 7,000 m/s. At 20 and 25 km depths, DeShon et al. (2006) report P-wave speeds over the Nicoya Peninsula of 6.72 and 7.01 km/s, respectively. Therefore, the maximum beam is roughly the expected P-wave speeds at the Peninsula, yet, the velocity structure offshore of the Peninsula and near the origin is less constrained. However, there is a significant discrepancy between the azimuth of the highest amplitude beam, 78°, and the expected azimuth for the earthquake location is 123°. In addition, there are a number of relatively high amplitude beams scattered at various azimuths in Figure B2. This suggests that the array geometry is too sparse for beamforming of high frequency seismic data.

In Figure B3, we show example seismograms from stations in the array and the maximum beam at 78° and 7,000 m/s speed. Upon closer examination of the shifted beam (Figure B3, lower panel), it appears that the catalogued event is preceded by smaller events. The presence of these signal at higher amplitude than the noise suggests smaller events in the vicinity of this larger earthquake. In addition, it highlights the difficulty of using the beamforming methodology on high frequency data in a region with high microseismicity. The sensitivity to detecting other events is likely the reason for the large number of high amplitude beams at different azimuths and wave speeds on Figure B2. However, this sensitivity could be leveraged to detect smaller events, otherwise undetected with conventional amplitude-dependent single station techniques (e.g. STA/LTA).

References

Agnew, D. C. (1996), SPOTL: Some programs for ocean-tide loading, SIO Ref. Ser. 96-8, 35 pp., Scripps Institution of Oceanography, La Jolla, CA.

Bilek, S.L., and T. Lay (2002), Tsunami earthquakes possibly widespread manifestations of frictional conditional stability, Geophys. Res. Lett., 29(14), 1673, doi: 10.1029/2002GL015215.

Brown, K. M., M. D. Tryon, H. R. DeShon, L. M. Dorman, and S. Y. Schwartz (2005), Correlated transient fluid pulsing and seismic tremor in the Costa Rican subduction zone, Earth and Planetary Science Letters, 238: 189-203.

Davis, E., et al. (2011), Evidence for episodic aseismic slip across the subduction seismogenic zone off Costa Rica: CORK borehole pressure observations at the subduction prism toe, Earth Planet. Sci. Lett., 306(3–4), 299–305, doi:10.1016/j.epsl.2011.04.017.

Feng, L., A. V. Newman, M. Protti, V. González, Y. Jiang, and T. H. Dixon (2012), Active deformation near the Nicoya Peninsula, northwestern Costa Rica, between 1996 and 2010: Interseismic megathrust coupling, J. Geophys. Res., 117, B06407, doi:10.1029/2012JB009230.

Hirose, H., Y. Asano, K. Obara, T. Kimura, T. Matsuzawa, S. Tanaka, and T. Maeda (2010), Slow earthquakes linked along dip in the Nankai subduction zone, Science, 330, 1502.

Ide, S., F. Imamura, Y. Yoshida, and K. Abe (1993), The characteristics of the Nicaraguan tsnunami earthquake of September 2, 1992, Geophysical Research Letters, 20(9): 863-866.

Ito, Y. and K. Obara, Dynamic deformation of the accretionary prism excites very low frequency earthquakes, Geophys. Res. Lett., 33, L02311, doi:10.1029/2005GL025270, 2006.

Ito, Y., K. Obara, T. Matsuzawa, and T. Maeda (2009), Very low frequency earthquakes related to small asperities on the plate boundary interface at the locked to aseismic transition, J. Geophys. Res., 114, B00A13, doi:10.1029/2008JB006036.

Jiang, Y., S. Wdowinski, T. H. Dixon, M. Hackl, M. Protti, and V. Gonzalez (2012), Slow slip events in Costa Rica detected by continuous GPS observations, 2002–2011, Geochem. Geophys. Geosyst., 13, Q04006, doi:10.1029/2012GC004058.

Lay, T. and T. C. Wallace (1995), Modern Global Seismology, Academic Press, 521 pp.

Lay, T., H. Kanamori, C. J. Ammon, K. D. Koper, A. R. Hutko, L. Ye, H. Yue, and T. M. Rushing (2012), Depth-varying rupture properties of subduction zone megathrust faults, J. Geophys. Res., 117, B04311, doi:10.1029/2011JB009133.

Moore, J. C., and D. Saffer (2001), Updip limit of the seismogenic zone beneath the accretionary prism of southwest Japan: An effect of diage- netic to low-grade metamorphic processes and increasing effective stress, Geology, 29, 183–186.

Nishenko, S. P. (1991), Circum-Pacific seismic potential: 1989-1999, Pure and Applied Geophysics, 135(2): 169-259.

Norabuena, E., et al. (2004), Geodetic and seismic constraints on some seismogenic zone processes in Costa Rica, J. Geophys. Res., 109, B11403, doi:10.1029/2003JB002931.

Obara, K. (2002), Nonvolcanic deep tremor associated with subduction in southwest Japan, Science, 296: 1679-1681.

Outerbridge, K. C., T. H. Dixon, S. Y. Schwartz, J. I. Walter, M. Protti, V. Gonzalez, J. Biggs, M. Thorwart, and W. Rabbel (in review), A Tremor and Slip Event on the Cocos-Caribbean Subduction zone as measured by a GPS and Seismic Network on the Nicoya Peninsula, Costa Rica, Journal of Geophysical Research.

Payero, J. S., V. Kostoglodov, N. Shapiro, T. Mikumo, A. Iglesias, X. Pérez-Campos, and R. W. Clayton (2008), Nonvolcanic tremor observed in the Mexican subduction zone, Geophys. Res. Lett., 35, L07305, doi:10.1029/2007GL032877.

Protti, M., F. Guendel, and K. McNally (1994), The geometry of the Wadati-Benioff zone under southern Central America and its tectonic significance: results from a high-resolution local seismographic network, Phys. Earth Planet. Int., 84, 271–287.

Rogers, G. and H. Dragert (2003), Episodic tremor and slip on the Cascadia subduction zone: the chatter of silent slip, Science, 300: 1942-1943.

Rost, S., and C. Thomas (2002), Array seismology: methods and applications, Reviews of Geophysics, 40, 3.

Scholz, C. H. (2002), The Mechanics of Earthquakes and Faulting, 2nd Edition, Cambridge University Press.

Schwartz, S. Y., and J. M. Rokosky (2007), Slow slip events and seismic tremor at circum-Pacific subduction zones, Rev. Geophys., 45, RG3004, doi:10.1029/2006RG000208.

Sugioka, H., T. Okamoto, T.Nakamura, Y. Ishihara, A. Ito, K. Obana, M. Kinoshita, K. Nakahigashi, M. Shinohara, and Y. Fukao (2012), Tsunamigenic potential of the shallow subduction plate boundary inferred from slow seismic slip, Nature Geoscience, 5: 414-418.

Walter, J. I., S. Y. Schwartz, J. M. Protti, and V. Gonzalez (2011), Persistent tremor within the northern Costa Rica seismogenic zone, Geophys. Res. Lett., 38, L01307, doi:10.1029/2010GL045586.

Wilcock, W. S. D. (2009), Tidal triggering of earthquakes in the northeast Pacific Ocean, Geophysical Journal International, 179(2): 1055-1070.

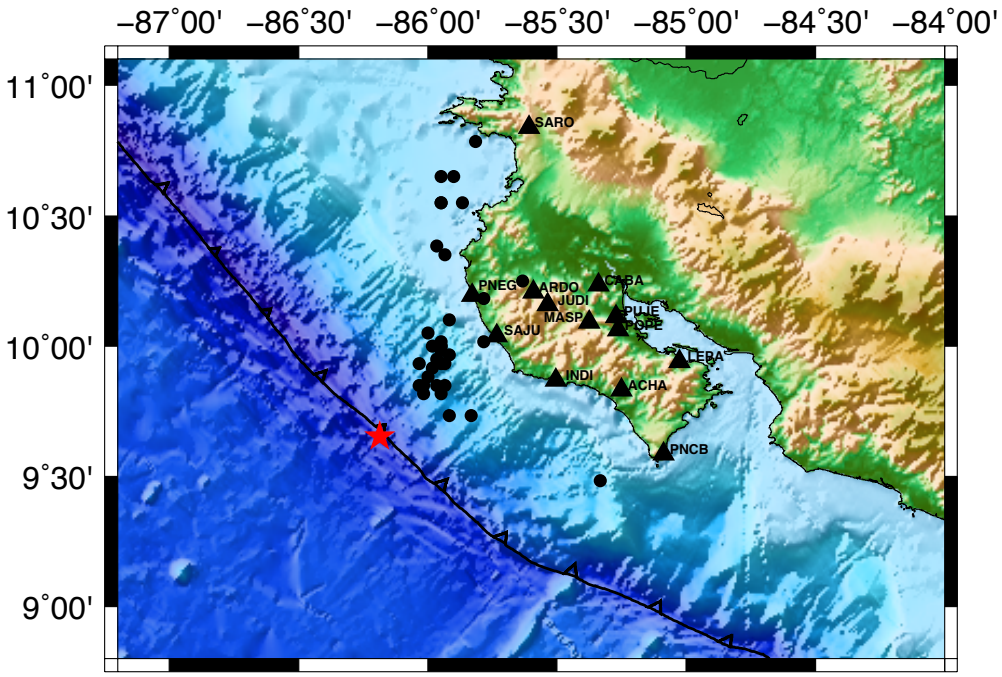

Figure 1: Location of tremor events occurring in August 2008. Red star marks the position of IODP Borehole 1255.

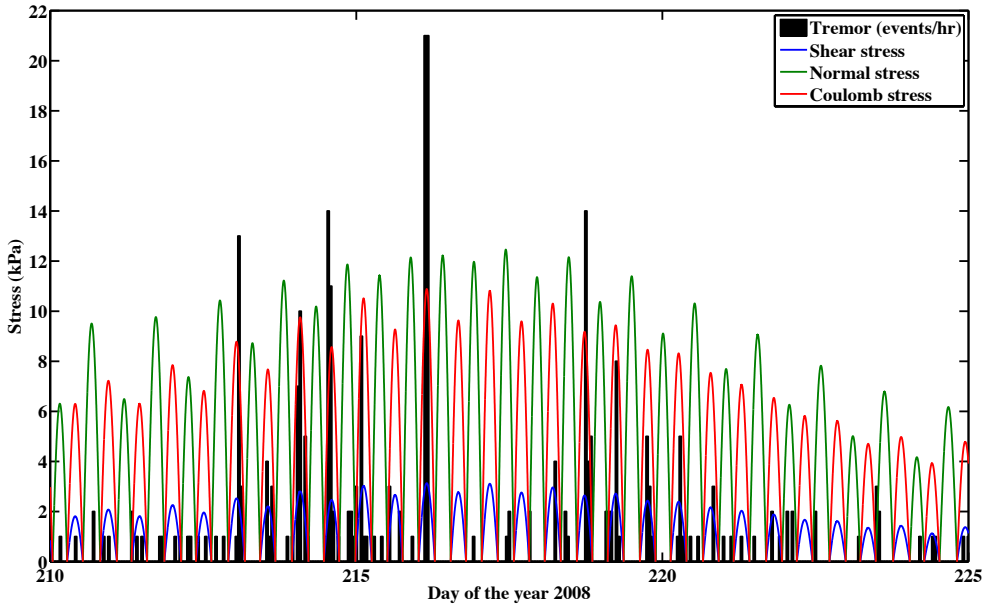

Figure 2: Ocean loading stresses oriented with respect to a 20 degree dip on the subduction interface from predicted tides near the offshore tremor locations. Black bar graph indicates number of tremor counts binned hourly.

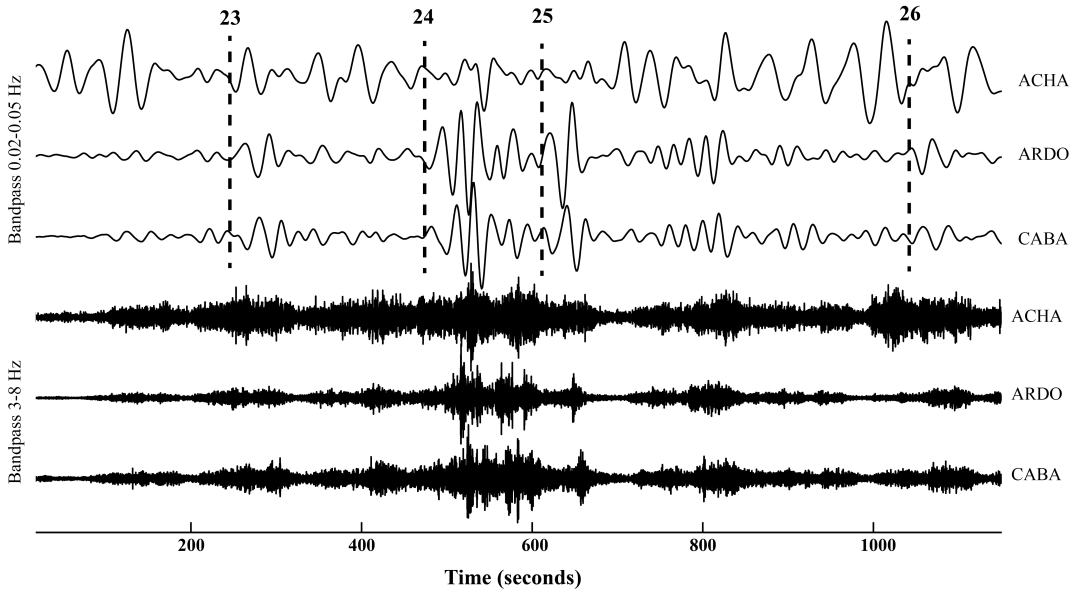

Figure 3: Example of presence of VLFEs during increased tremor activity. All stations are the horizontal east component, the top three seismograms are bandpassed from 0.02-0.05 Hz and the bottom three are bandpassed 3-8 Hz for the same stations. Vertical dashed lines indicate identification of VLFEs and their corresponding event number (See supplementary table).

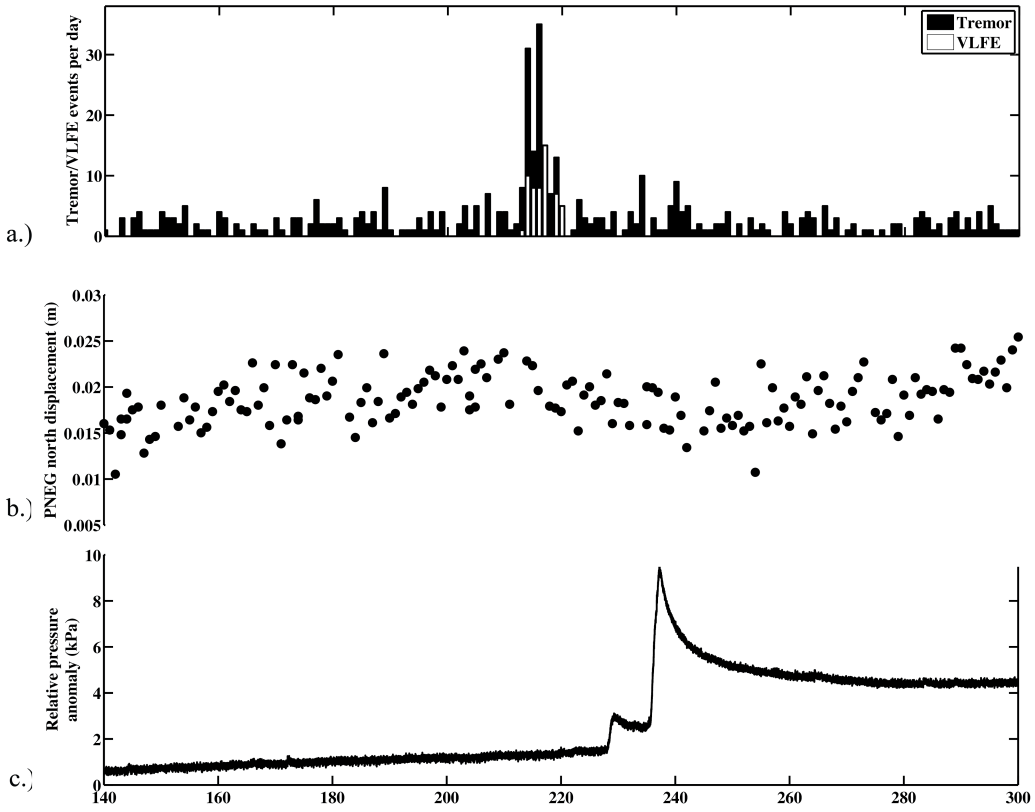

Figure 4: Evidence for offshore slow slip and tremor include (4a.) tremor histogram of events per day, (4b.) GPS displacement at coastal station PNEG, and (4c.) pressure transient observed at IODP Site 1255. The peak pressure changes occur ~15-25 days following the peak in tremor activity.

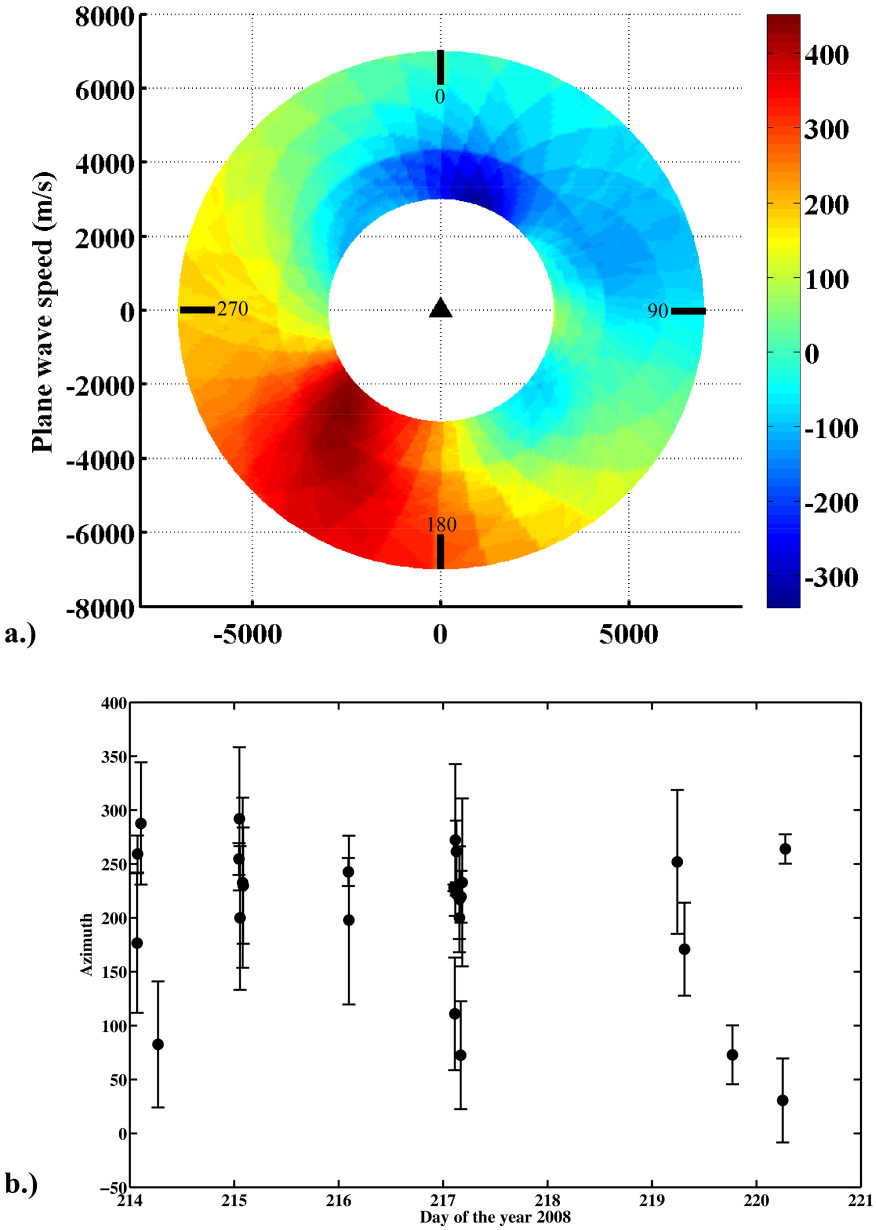

Figure 5: Beamforming of VLFE activity, including (5a.) example for event 35 (See supplementary table), indicating azimuth and wave speed of highest amplitude beam. Figure 5b is the average azimuth for the three components, where error bars indicate standard deviation. Note that Figure 5b includes 26 of 54 identified events, as we do not show events where the standard deviation is less than 80 degrees.

Event Number	Year	Day	Time
1	2008	213	22:17:51
2	2008	214	1:42:09
3	2008	214	1:47:49
4	2008	214	1:56:46
5	2008	214	2:05:49
6	2008	214	2:11:10
7	2008	214	2:28:28
8	2008	214	2:35:57
9	2008	214	2:40:16
10	2008	214	2:46:55
11	2008	214	6:30:42
12	2008	215	1:06:01
13	2008	215	1:11:50
14	2008	215	1:20:34
15	2008	215	1:23:10
16	2008	215	1:26:15
17	2008	215	1:35:56
18	2008	215	1:58:44
19	2008	215	2:04:50
20	2008	216	1:02:05
21	2008	216	1:20:58
22	2008	216	2:08:17
23	2008	216	2:12:11
24	2008	216	2:14:28
25	2008	216	2:21:32
26	2008	216	2:39:40
27	2008	216	23:51:43
28	2008	217	2:30:51
29	2008	217	2:36:53
30	2008	217	2:38:23
31	2008	217	2:41:19
32	2008	217	2:44:29
33	2008	217	2:48:28
34	2008	217	3:00:33
35	2008	217	3:03:41
36	2008	217	3:29:48
37	2008	217	3:44:03
38	2008	217	3:45:43
39	2008	217	3:58:15
40	2008	217	4:03:59
41	2008	217	4:07:43
42	2008	217	4:24:23
43	2008	219	5:39:30
44	2008	219	5:43:08
45	2008	219	5:48:31
46	2008	219	6:00:21
47	2008	219	7:28:12
48	2008	219	17:58:05
49	2008	219	18:29:51
50	2008	220	5:59:00
51	2008	220	6:02:57
52	2008	220	6:07:00
53	2008	220	6:13:41
54	2008	220	6:37:59

Supplementary Table 1: Catalog of VLFEs visually identified between Days 210-230.

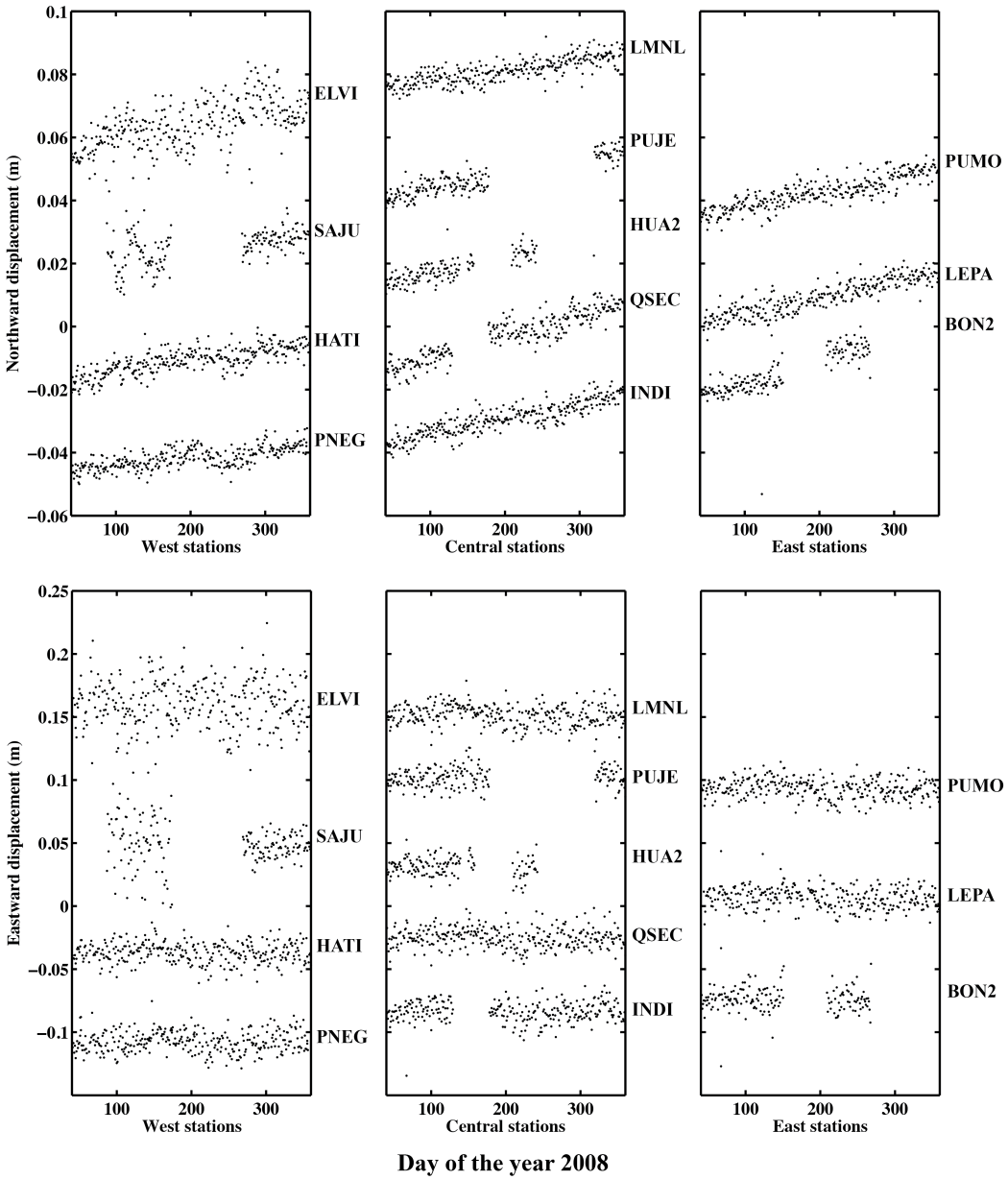

Supplementary Figure S1: GPS northward and eastward displacement for all stations.

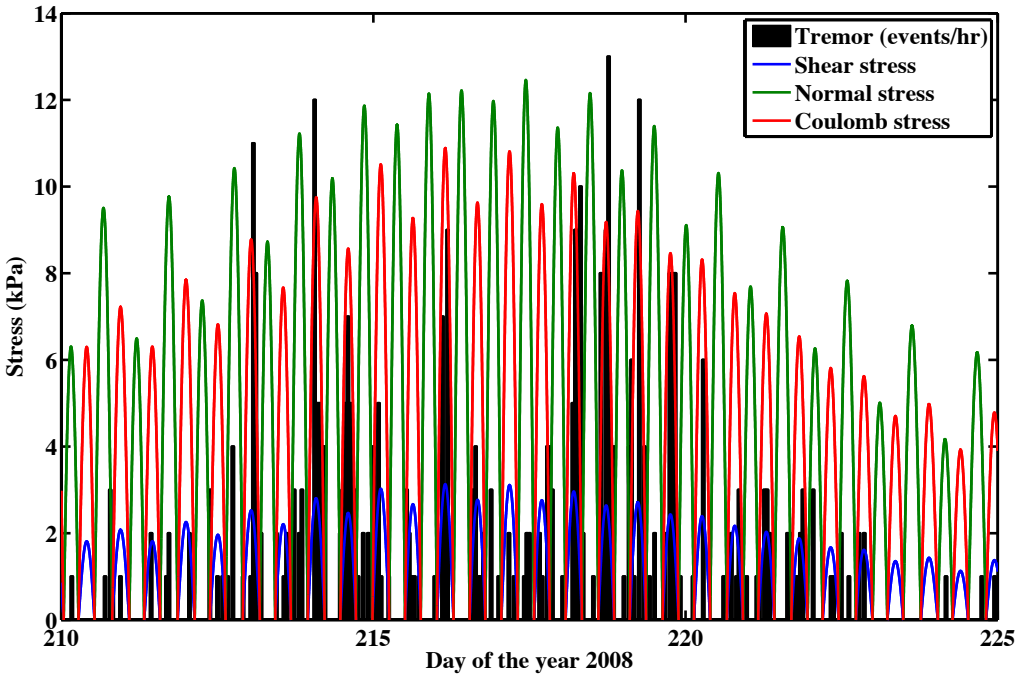

Figure A1: Ocean loading stresses oriented with respect to a 20 degree dip on the subduction interface from predicted tides near the offshore tremor locations. Black bar graph indicates number of tremor counts binned hourly, using the Kim et al. (2011) and provided by M. Kim (personal communication).

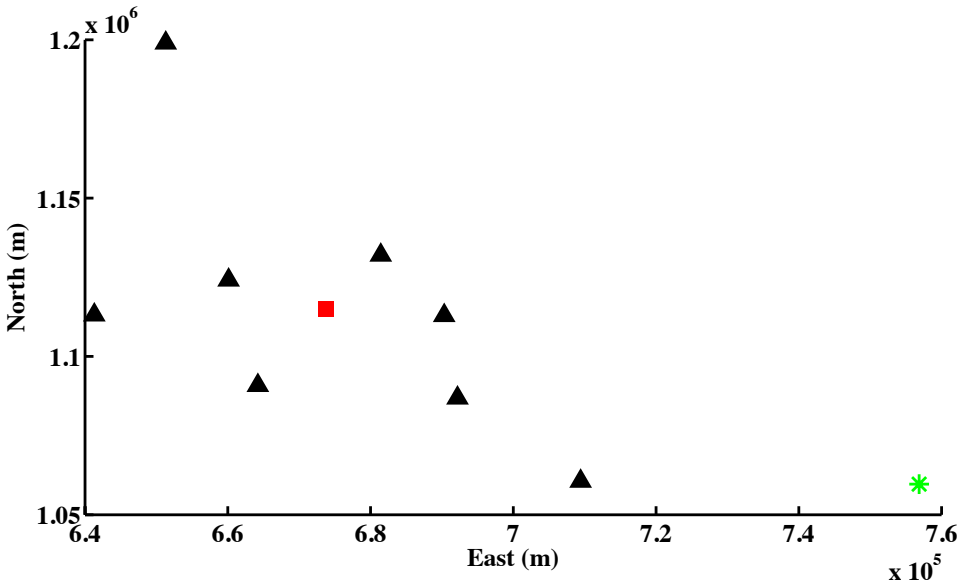

Figure B1. Array geometry for beamforming the identified earthquake. Seismic stations are black triangles, center of the array is a red square, and the earthquake location is a green star.

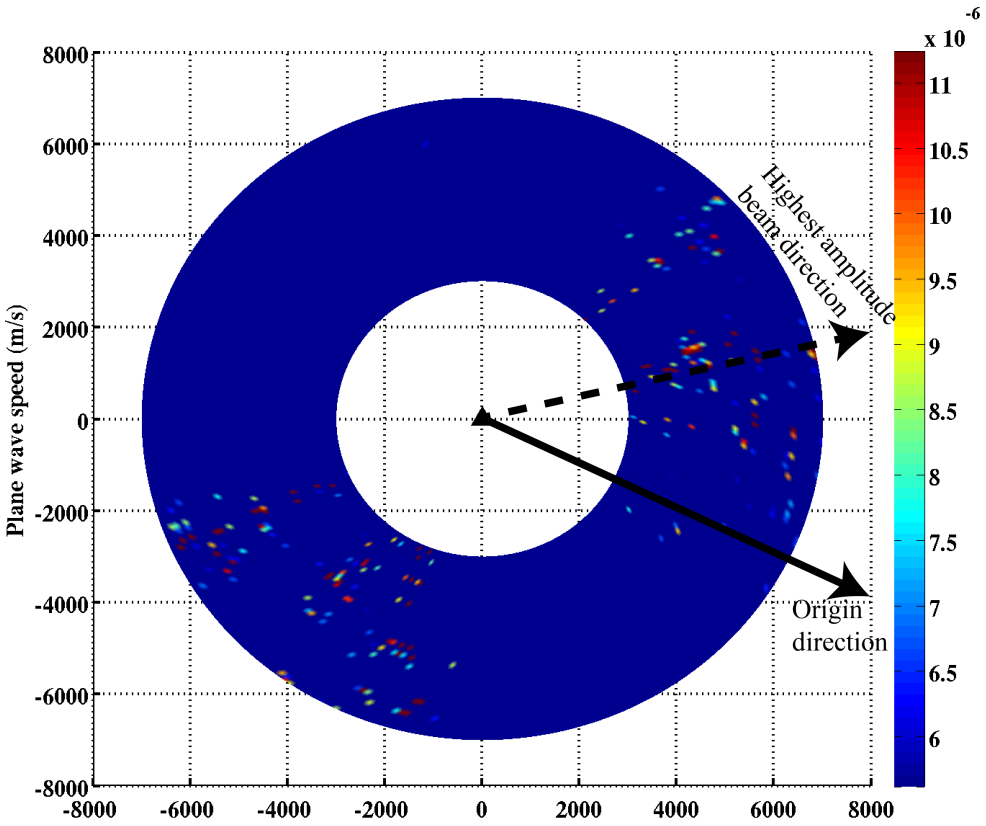

Figure B2. Beams for time series, including the identified earthquake.

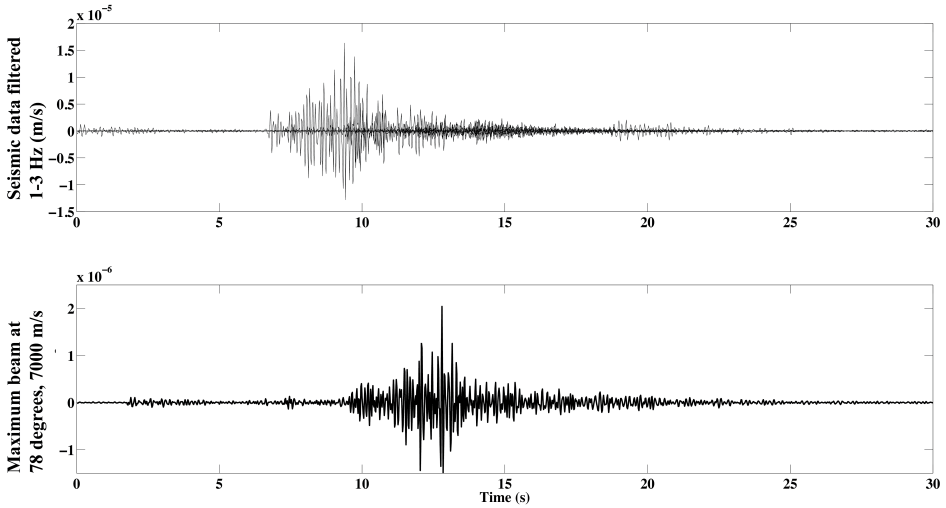

Figure B3: Upper panel, seismogram from various stations band-passed 1-3 Hz. Maximum beam from previous figure at an azimuth of 78°.